



LUND UNIVERSITY

The Formation and Breakdown of Passive Film on Ni Alloys in situ synchrotron studies

Larsson, Alfred

2023

[Link to publication](#)

Citation for published version (APA):

Larsson, A. (2023). *The Formation and Breakdown of Passive Film on Ni Alloys: in situ synchrotron studies*. Lund University.

Total number of authors:

1

General rights

Unless other specific re-use rights are stated the following general rights apply:

Copyright and moral rights for the publications made accessible in the public portal are retained by the authors and/or other copyright owners and it is a condition of accessing publications that users recognise and abide by the legal requirements associated with these rights.

- Users may download and print one copy of any publication from the public portal for the purpose of private study or research.
- You may not further distribute the material or use it for any profit-making activity or commercial gain
- You may freely distribute the URL identifying the publication in the public portal

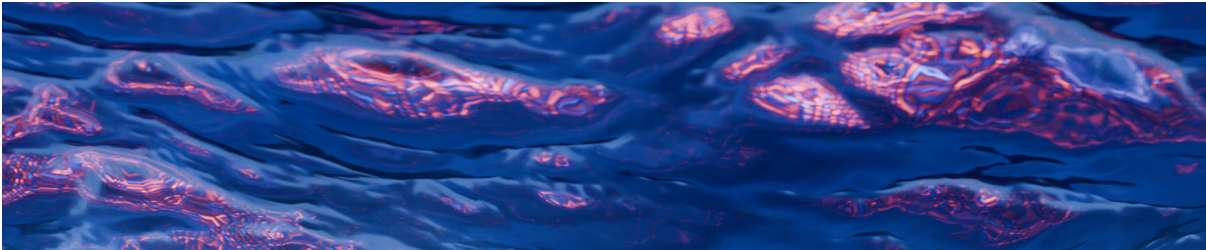
Read more about Creative commons licenses: <https://creativecommons.org/licenses/>

Take down policy

If you believe that this document breaches copyright please contact us providing details, and we will remove access to the work immediately and investigate your claim.

LUND UNIVERSITY

PO Box 117
221 00 Lund
+46 46-222 00 00

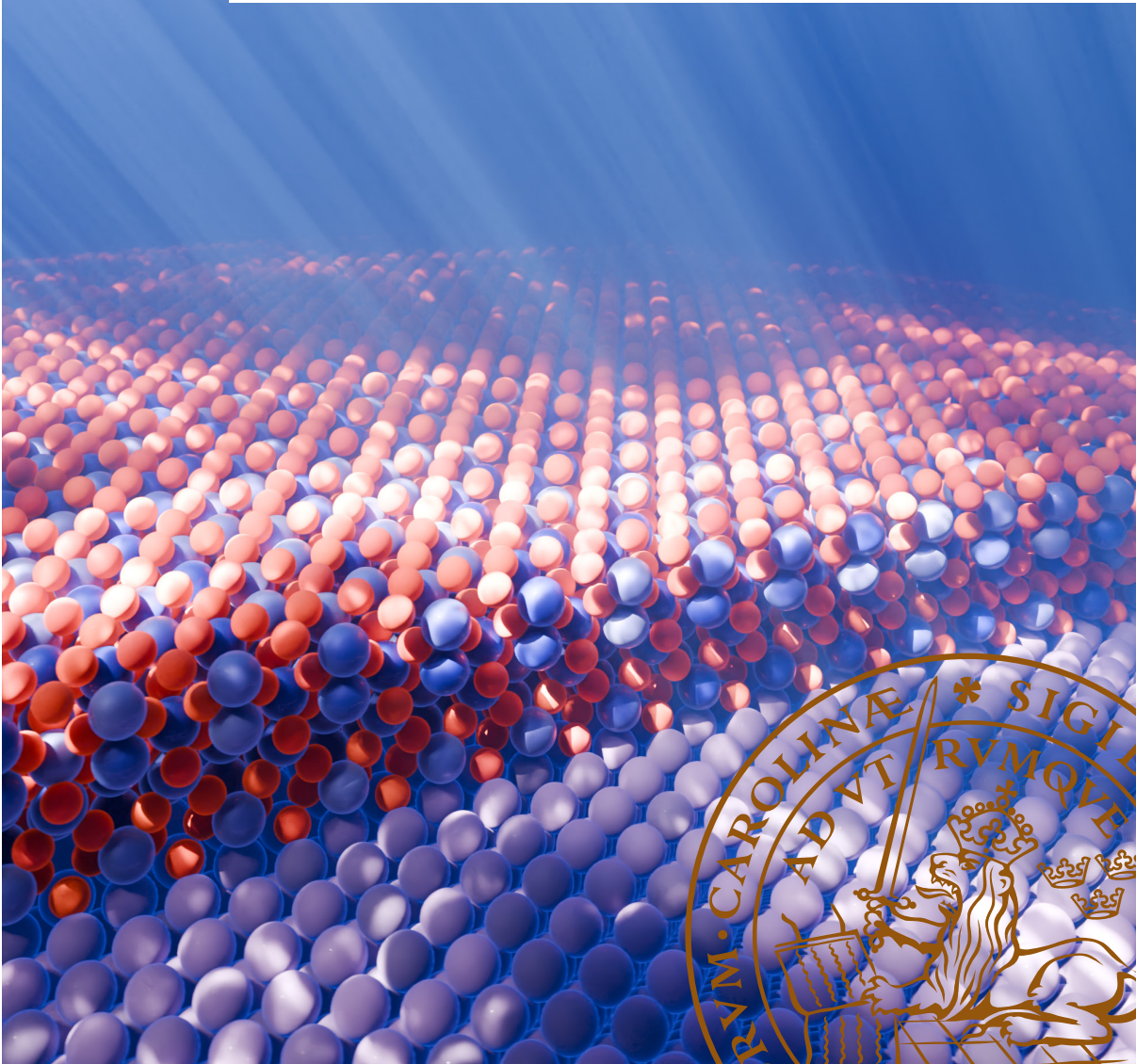


The Formation and Breakdown of Passive Films on Ni Alloys

in situ synchrotron-based studies

ALFRED LARSSON

DEPARTMENT OF PHYSICS | FACULTY OF SCIENCE | LUND UNIVERSITY





Printed by Media-Tryck, Lund 2023  NORDIC SWAN ECOLABEL 304119093



LUND
UNIVERSITY

Faculty of Science
Department of Physics

ISBN 978-91-8039-845-9



The Formation and Breakdown of Passive Films on Ni Alloys

The Formation and Breakdown of Passive Films on Ni Alloys

in situ synchrotron-based studies

Alfred Larsson



LUND
UNIVERSITY

DOCTORAL DISSERTATION

by due permission of the Faculty of Science, Lund University, Sweden.
To be defended in the Rydberg Lecture Hall at the Department of Physics.

Date: 2023-12-15 and time: 13:00

Faculty opponent

Prof. Arjan Mol, Delft University of Technology

Organization LUND UNIVERSITY	Document name: Doctoral thesis	
	Date of issue: 2023-12-15	
Author: Alfred Larsson	Sponsoring organization -	
Title and subtitle: The Formation and Breakdown of Passive Films on Ni Alloys: <i>in situ</i> synchrotron-based studies		
Abstract		
<p>Corrosion results in huge annual costs and a large environmental footprint. The corrosion rate of some alloys can be made negligible by the presence of a spontaneously forming oxide film on the surface, a so-called passive film. Famous examples of alloys exhibiting passivity are stainless steels. However, in some demanding applications, stainless steel does not provide significant corrosion resistance. Instead, Ni alloys are used, which are known for their excellent corrosion resistance. The nature, formation, and mechanism of breakdown of the passive films that form on Ni alloys is, however, not well understood.</p> <p>In this thesis, a combination of <i>in situ</i> synchrotron-based methods has been used to elucidate the chemistry and structure of the thin oxide films that dictate the corrosion resistance, as well as the chemistry of the electrolyte above the sample surface to probe the concentration of dissolved ions and their chemical state. This was also coupled with the use of optical microscopy to provide a full-field view of the surface <i>in situ</i>.</p> <p>It was found that the passive film on the studied Ni-Cr-Mo alloys mainly contains Cr oxides and Mo oxides, while Ni does not participate in the oxide film. The film is only one nanometer thick and forms rapidly upon exposure to oxygen. It was shown that even if the initial oxidation kinetics are rapid, it takes time for a true steady-state composition to be reached, and aging of the sample surface in air affects the oxide thickness and composition. It was also found that Ni-Cr-Mo alloys exhibit a transpassive breakdown mechanism that is different from that of typical Cr-containing alloys. This mechanism was also found to be connected to the catalytic activity towards the oxygen evolution reaction, which takes place at increased anodic potentials. Lastly, this thesis also covers some method development of both X-ray-based and optical surface-sensitive methods that were used to study the thin oxide films at the solid-liquid interface <i>in situ</i>.</p>		
Key words		
Classification system and/or index terms (if any)		
Supplementary bibliographical information		Language English
ISSN and key title		ISBN 978-91-8039-845-9 (print) 978-91-8039-846-6 (digital)
Recipient's notes	Number of pages: 110	Price
	Security classification	

I, the undersigned, being the copyright owner of the abstract of the above-mentioned dissertation, hereby grant to all reference sources permission to publish and disseminate the abstract of the above-mentioned dissertation.

Signature

Date 2023-10-30

The Formation and Breakdown of Passive Films on Ni Alloys

in situ synchrotron-based studies

Alfred Larsson



LUND
UNIVERSITY

Cover photo by Vidar Flodgren & Alfred Larsson

Copyright pp 1-110 Alfred Larsson

Paper 1 © ELSEVIER

Paper 2 © ACS

Paper 3 © IOP Publishing

Paper 4 © John Wiley & Sons

Paper 5 © by the Authors (Manuscript unpublished)

Paper 6 © ELSEVIER

Paper 7 © AIP Publishing

Paper 8 © ACS

Paper 9 © by the Authors (Manuscript unpublished)

Faculty of Science
Department of Physics

ISBN: 978-91-8039-845-9 (print)

ISBN: 978-91-8039-846-6 (digital)

Printed in Sweden by Media-Tryck, Lund University
Lund 2023



Media-Tryck is a Nordic Swan Ecolabel
certified provider of printed material.
Read more about our environmental
work at www.mediatryck.lu.se

MADE IN SWEDEN 

*Dedicated to my family and friends,
who make me want to keep on going.*

Table of Contents

List of publications.....	x
Papers included in this thesis:.....	x
Papers to which I have contributed but that are not covered in this thesis:.....	xiii
Abstract	xvii
Populärvetenskaplig sammanfattning.....	xviii
Popular summary.....	xx
Acknowledgments.....	xxii
List of abbreviations.....	xxiv
1. Introduction	1
2. Materials	5
Crystals and alloys	5
Ni-based alloys.....	7
Oxides	8
Surfaces and atomic planes	9
Thin oxide films on metal surfaces	10
3. Electrochemistry.....	15
Fundamentals	15
Passivity	21
Passive film growth.....	22
Passive film breakdown and corrosion reactions.....	25
Electrochemical techniques.....	28
Polarization curve.....	28
Electrochemical impedance spectroscopy	29
Mott-Schottky analysis.....	30
Electrochemical cell for synchrotron experiments.....	31

4.	X-ray based techniques.....	33
	Introduction to X-rays	33
	Synchrotron radiation and beamlines	35
	X-ray photoelectron spectroscopy.....	41
	Ambient pressure X-ray photoelectron spectroscopy.....	46
	X-ray absorption near edge structure	50
	X-ray fluorescence	51
	X-ray diffraction.....	52
	Grazing Incidence Geometry	56
	X-ray reflectivity	58
	<i>In situ</i> vs. <i>operando</i> studies of electrochemical interfaces.....	59
	Beam damage and beam-induced effects	60
5.	Complementary techniques.....	63
	Two-Dimensional Surface optical reflectance	63
	Scanning electron microscopy	64
6.	Summary of papers	67
	Passive film formation	67
	Paper I.....	67
	Paper II.	67
	Paper III.....	68
	Passive film breakdown	68
	Paper IV	68
	Paper V.....	69
	Method development.....	69
	Paper VI.....	69
	Paper VII.	69
	Paper VIII.....	70
	Paper IX.....	70
7.	Summary & Outlook.....	71
	References	75

List of publications

Papers included in this thesis:

Paper I.

Thickness and composition of native oxides and near-surface regions of Ni superalloys

A. Larsson, G. D'Acunto, M. Vorobyova, G. Abbondanza, U. Lienert, Z. Hegedüs, A. Preobrajenski, L. R. Merte, J. Eihagen, A. Delblanc, J. Pan, E. Lundgren

Journal of Alloys and Compounds, 895, (2022), 162657

I analyzed the data and wrote the manuscript.

Paper II.

Dynamics of early-stage oxide formation on a Ni-Cr-Mo alloy

A. Larsson, S. Gericke, A. Grespi, V. Koller, J. Eihagen, X. Yue, E. Frampton, S. Appelfeller, A. Generalov, A. Preobrajenski, J. Pan, H. Over, and E. Lundgren

Manuscript

I wrote the beamtime proposals and was the main responsible for the synchrotron experiments. I analyzed the data and wrote the manuscript.

Paper III.

Synchrotron XPS and Electrochemical Study of Aging Effect on Passive Film of Ni Alloys

J. Eihagen, A. Larsson, A. Preobrajenski, A. Delblanc, E. Lundgren, J. Pan

Journal of The Electrochemical Society, 170, (2023), 021506

I analyzed the XPS data and contributed to the discussion and editing of the manuscript.

Paper IV.

The Oxygen Evolution Reaction Drives Passivity Breakdown for Ni–Cr–Mo Alloys

A. Larsson, A. Grespi, G. Abbondanza, J. Eidhagen, D. Gajdek, K. Simonov, X. Yue, U. Lienert, Z. Hegedüs, A. Jeromin, T. F. Keller, M. Scardamaglia, A. Shavorskiy, L. R. Merte, J. Pan, E. Lundgren

Advanced Materials, (2023), 2304621

I was the main responsible for planning and leading the synchrotron experiments. I analyzed all the data, and I wrote the manuscript.

Paper V.

Operando Surface Optical Reflectance Microscopy Study of Corrosion Film Growth on a Ni-Cr-Mo Alloy During Anodic Polarization

A. Larsson, M. Vorobyova, S. Pfaff, G. Abbondanza, J. Pan, J. Zetterberg, E. Lundgren

The Journal of Physical Chemistry C, (2023),

I took part in planning the experiments and supervised the master student Mariya, who performed the experiments. I analyzed the data and wrote the manuscript.

Paper VI.

In situ quantitative analysis of electrochemical oxide film development on metal surfaces using ambient pressure X-ray photoelectron spectroscopy: Industrial alloys

A. Larsson, K. Simonov, J. Eidhagen, A. Grespi, X. Yue, H. Tang, A. Delblanc, M. Scardamaglia, A. Shavorskiy, J. Pan, E. Lundgren

Applied Surface Science, 611, (2023), 155714

I was the main responsible for planning and leading the synchrotron experiments. I analyzed the data, and I wrote the manuscript.

Paper VII.

An electrochemical cell for 2-dimensional surface optical reflectance during anodization and cyclic voltammetry

W. Linpé, G. S. Harlow, A. Larsson, G. Abbondanza, L. Rämisch, S. Pfaff, J. Zetterberg, J. Evertsson, E. Lundgren

Review of Scientific Instruments, 91, (2020), 044101

I took part in the discussion of the manuscript.

Paper VIII.

Operando Reflectance Microscopy on Polycrystalline Surfaces in Thermal Catalysis, Electrocatalysis, and Corrosion

S. Pfaff*, A. Larsson*, D. Orlov, G. S. Harlow, G. Abbondanza, W. Linpé, L. Rämisch, S. M. Gericke, J. Zetterberg, E. Lundgren

ACS Applied Materials & Interfaces, 13,16, (2021), 19530-19540

* These authors contributed equally

I took part in performing the gas phase experiments, and I was responsible for the electrochemical experiments. I took part in the data analysis and in the writing of the manuscript.

Paper IX.

Probing the electrode-electrolyte interface using operando total reflection X-ray absorption spectroscopy

A. Grespi, A. Larsson, G. Abbondanza, J. Eindhagen, D. Gajdek, J. Manidi, A. Tayal, A. Kalinko, J. Pan, L. R. Merte, E. Lundgren

Manuscript

I wrote the beamtime proposal, and I took part in the planning and leading of the synchrotron experiments. I took part in the discussion of the data and the manuscript.

Papers to which I have contributed but that are not covered in this thesis:

Paper X.

Electrochemical Fabrication and Characterization of Palladium Nanowires in Nanoporous Alumina Templates

A. Larsson, G. Abbondanza, W. Linpé, F. Carlà, P. Mousley, C. Hetherington, E. Lundgren, G. S. Harlow

Journal of The Electrochemical Society, 167, (2020), 122514

Paper XI.

Time-resolved grazing-incidence X-ray diffraction measurement to understand the effect of hydrogen on surface strain development in super duplex stainless steel

C. Örnek, A. Larsson, G. S. Harlow, F. Zhang, R. Kroll, F. Carlà, H Hussain, U. Kivisäkk, D. L. Engelberg, E. Lundgren, J. Pan

Scripta Materialia, 187, (2020), 63-67

Paper XII.

Metastable precursor structures in hydrogen-infused super duplex stainless steel microstructure – An operando diffraction experiment

C. Örnek, A. Larsson, G. S. Harlow, F. Zhang, R. Kroll, F. Carlà, H Hussain, U. Kivisäkk, D. L. Engelberg, E. Lundgren, J. Pan

Corrosion Science, 176, (2020), 109021

Paper XIII.

In situ scanning X-ray diffraction reveals strain variations in electrochemically grown nanowires

A. Larsson, G. Abbondanza, L. Rämisch, W. Linpé, D. V. Novikov, E. Lundgren, G. S. Harlow

Journal of Physics D: Applied Physics, 54, (2021), 235301

Paper XIV.

Quantitative powder diffraction using a (2+3) surface diffractometer and an area detector

G. Abbondanza, [A. Larsson](#), F. Carlá, E. Lundgren and G. S. Harlow

Journal of Applied Crystallography, 54, (2021), 1140-1152

Paper XV.

Revisiting Optical Reflectance from Au(111) Electrode Surfaces with Combined High-Energy Surface X-ray Diffraction

W. Linpé, L. Rämisch, G. Abbondanza, [A. Larsson](#), S. Pfaff, L. Jacobse, J. Zetterberg, L. Merte, A. Stierle, Z. Hegedues, U. Lienert, E. Lundgren, G. S. Harlow

Journal of The Electrochemical Society, 168, (2021), 096511

Paper XVI.

Operando Stability Studies of Ultrathin Single-Crystalline IrO₂(110) Films under Acidic Oxygen Evolution Reaction Conditions

T. Weber, V. Vonk, D. Escalera-López, G. Abbondanza, [A. Larsson](#), V. Koller, M. J.S. Abb, Z. Hegedüs, T. Bäcker, U. Lienert, G. S. Harlow, A. Stierle, S. Cherevko, E. Lundgren, H. Over

ACS Catalysis, 11, 20, (2021), 12651-12660

Paper XVII.

Templated electrodeposition as a scalable and surfactant-free approach to the synthesis of Au nanoparticles with tunable aspect ratios

G. Abbondanza, [A. Larsson](#), W. Linpé, C. Hetherington, F. Carlá, E. Lundgren, G. S. Harlow

Nanoscale Advances, 4, (2022), 2452-2467

Paper XVIII.

Visualizing the Gas Diffusion Induced Ignition of a Catalytic Reaction

S. Pfaff, L. Rämisch, S. M. Gericke, [A. Larsson](#), E. Lundgren, J. Zetterberg

ACS Catalysis, 12, 11, (2022), 6589-6595

Paper XIX.

Anisotropic strain variations during the confined growth of Au nanowires

G. Abbondanza, A. Grespi, A. Larsson, L. Glatthaar; T. Weber; M. Blankenburg; Z. Hegedüs, U. Lienert, H. Over, E. Lundgren

Applied Physics Letters, 122, (2023), 123101

Paper XX.

Synchrotron-based near ambient-pressure X-ray photoelectron spectroscopy and electrochemical studies of passivation behavior of N- and V-containing martensitic stainless steel

X. Yue, A. Larsson, H. Tang, A. Grespi, M. Scardamaglia, A. Shavorskiy, A. Krishnan, E. Lundgren, J Pan

Corrosion Science, 214, (2023), 111108

Paper XXI.

The causation of hydrogen embrittlement of duplex stainless steel: Phase instability of the austenite phase and ductile-to-brittle transition of the ferrite phase – Synergy between experiments and modelling

C. Örnek, M. Mansoor, A. Larsson, F. Zhang, G. S. Harlow, R. Kroll, F. Carlà, H. Hussain, B. Derin, U. Kivisäkk, D. L. Engelberg, E. Lundgren, J. Pan

Corrosion Science, 217, (2023), 111140

Paper XXII.

Understanding passive film degradation and its effect on hydrogen embrittlement of super duplex stainless steel – Synchrotron X-ray and electrochemical measurements combined with CalPhaD and ab-initio computational studies

C. Örnek, F: Zhang, A. Larsson, M. Mansoor, G. S. Harlow, R. Kroll, F. Carlà, H. Hussain, D. L. Engelberg, B. Derin, J. Pan

Applied Surface Science, 628, (2023), 15764

Paper XXIII.

Ex-situ synchrotron X-ray diffraction study of CO₂ corrosion-induced surface scales developed in low-alloy steel with different initial microstructure

S. Haratian, K. K. Gupta, [A. Larsson](#), G. Abbondanza, E. H. Bartawi, F. Carlà, E. Lundgren, R. Ambat

Corrosion Science, 222, (2023), 111387

Paper XXIV

Hydride formation and dynamic phase changes during template-assisted Pd electrodeposition

G. Abbondanza, A. Grespi, [A. Larsson](#), D. Dzhigaev, L. Glatthaar, T. Weber, M. Blankenburg, Z. Hegedüs, U. Lienert, H. Over, G. S. Harlow, E. Lundgren

Nanotechnology, (2023)

Paper XXV

Critical Step in the HCl Oxidation Reaction over Single-Crystalline CeO_{2-x}(111): Peroxo-Induced Site Change of Strongly Adsorbed Surface Chlorine

V. Koller, P. G. Lustemberg, A. Spriewald-Luciano, S. M. Gericke, [A. Larsson](#), C. Sack, A. Preobrajenski, E. Lundgren, M. V. Ganduglia-Pirovano, H. Over

ACS Catalysis, 13, (2023), 12994–13007

Paper XXVI

Effect of hydrogen on the passivation for ultra-thin 316 L SS foil

X. Yue, Z. Yang, [A. Larsson](#), H. Tang, S. Appelfeller, B. Sefer, A. Preobrajenski, J. Li, L. Zhang, J. Pan

npj Materials Degradation, 7, (2023)

Abstract

Corrosion results in huge annual costs and a large environmental footprint. The corrosion rate of some alloys can be made negligible by the presence of a spontaneously forming oxide film on the surface, a so-called passive film. Famous examples of alloys exhibiting passivity are stainless steels. However, in some demanding applications, stainless steel does not provide significant corrosion resistance. Instead, Ni alloys are used, which are known for their excellent corrosion resistance. The nature, formation, and mechanism of breakdown of the passive films that form on Ni alloys is, however, not well understood.

In this thesis, a combination of *in situ* synchrotron-based methods has been used to elucidate the chemistry and structure of the thin oxide films that dictate the corrosion resistance, as well as the chemistry of the electrolyte above the sample surface to probe the concentration of dissolved ions and their chemical state. This was also coupled with the use of optical microscopy to provide a full-field view of the surface *in situ*.

It was found that the passive film on the studied Ni-Cr-Mo alloys mainly contains Cr oxides and Mo oxides, while Ni does not participate in the oxide film. The film is only one nanometer thick and forms rapidly upon exposure to oxygen. It was shown that even if the initial oxidation kinetics are rapid, it takes time for a true steady-state composition to be reached, and aging of the sample surface in air affects the oxide thickness and composition. It was also found that Ni-Cr-Mo alloys exhibit a transpassive breakdown mechanism that is different from that of typical Cr-containing alloys. This mechanism was also found to be connected to the catalytic activity towards the oxygen evolution reaction, which takes place at increased anodic potentials. Lastly, this thesis also covers some method development of both X-ray-based and optical surface-sensitive methods that were used to study the thin oxide films at the solid-liquid interface *in situ*.

Populärvetenskaplig sammanfattning

Denna avhandling handlar om att förstå korrosion, hur det går till, och hur det kan undvikas. Men vad är korrosion? Korrosion är kemiska och elektrokemiska reaktioner som ger upphov till förstörelse och frätning av metaller när de exponeras för, till exempel, saltvatten eller en syra. Rost bildas när järn och legeringar av järn, så som stål, korroderar. Detta sker när metallen är exponerad för syre, som finns i luft och vatten. Korrosion resulterar årligen i stora kostnader. 4 % av alla länders BNP spenderas på service, lagning och andra kostnader relaterade till korrosion. Framställning av metaller släpper även ut stora mängder växthusgaser. Så om vi kan undvika korrosion så skulle det även ha en positiv klimatpåverkan.

Forskare har tidigare lyckats utveckla en del legeringar som spontant kan stå emot korrosion. En legering är ett metalliskt material som består av en blandning av grundämnen. Den mest kända legeringen är stål, som är en legering av järn och kol. Rostfritt stål, som är den mest kända korrosionsmotståndiga legeringen består framförallt av järn och krom. När rostfritt stål exponeras för syre eller vatten så bildas inte rost, som är järnoxider och hydroxider, utan en kemisk förening av krom och syre, en kromoxid. På den rostfria stålytan bildas ett väldigt tunt skyddande lager av denna kromoxid. Oxidlagret är bara några få atomlager tjockt, ca en nanometer. Detta är 100,000 gånger tunnare än ett hårstrå.

Dessa tunna skyddande oxidfilmer som spontant kan bildas på vissa metallytor kallas för passiva filmer, då de får ytan av en metall, som annars skulle frätas sönder, att bli ”passiv” även i aggressiva miljöer. Passivitet hos vissa legeringar är något som studerats länge men det är fortfarande debatterat och inte ett fullt förstått koncept. Även material så som rostfritt stål kan få korrosionsangrepp i vissa aggressiva miljöer, genom att det passiva oxidskiktet bryts ner och ej längre är stabilt.

Inom användningsområden där rostfritt stål inte duger, till exempel inom kemiindustrin, kärnkraftverk och jetmotorer, så kan en legering av nickel, krom, och molybden användas. Ett material som alltså inte är järn-baserat. Dessa nickellegeringar är kända för att klara höga påfrestningar och höga temperaturer och började utvecklas på 1950 talet. Från många års erfarenhet inom industrin är det välkänt att dessa legeringar har ett utomordentligt korrosionsmotstånd. Men detaljerna kring den passiva filmen som bildas på nickellegeringar, som ger upphov till materialets korrosionsmotstånd, är inte så väl kända. Hur det passiva oxidlagret bildas, vad det består av och hur det bryts ner på nickellegeringar är vad denna avhandling fokuserar på att försöka lista ut.

Att studera dessa oxidfilmer, 100,000 gånger tunnare än ett hårstrå, som existerar i gränssnittet mellan metall och vätska är inte enkelt. Denna avhandling syftar även till att utveckla och förbättra experimentella verktyg som vi forskare kan använda för att studera dessa tunna, komplexa och viktiga oxidlager. De flesta experiment

som är del av denna avhandling har utförts på så kallade synkrotronljusanläggningar. Man kan likna det vid ett enormt mikroskop som låter oss forskare "se" och studera pyttesmå saker. MAX IV i Lund är en sådan synkrotronljusanläggning, en partikelaccelerator med en omkrets på 528 meter (samma omkrets som Colosseum i Rom), som skapar röntgenstrålar som vi använder för våra experiment. Med hjälp av sådana storskaliga anläggningar har vi kunnat få en ökad förståelse för de tunna oxidfilmer som ger upphov till korrosionsmotståndet hos avancerade nickel-baserade legeringar.

Avhandlingen avslutas med ett antal artiklar. I de tre första (**Paper I**, **Paper II** och **Paper III**) så bestäms kompositionen och tjockleken på de tunna oxidlagren som spontant bildas på tre industriella nickellegeringar. Det redovisas även hur de initialt bildas när en icke-oxiderad metallyta exponeras för syre, samt hur lagring i luft kan påverka den kemiska sammansättningen och tjockleken på de skyddande oxidlagren som bildas på ytan av dessa nickellegeringar.

I de två senare artiklarna i avhandlingen (**Paper IV** och **Paper V**) visas det hur det passiva oxidlagret bryts ner under accelererade korrosionstester. Inom industrin är det viktigt att kunna göra trovärdiga accelererade tester av ett materials korrosionsmotstånd för att kunna förutsäga och veta, vilket material som klarar vilket användningsområde. En ny och okänd korrosionsmekanism redovisas i avhandlingen, en mekanism som uppkommer under accelererade korrosionstester av vissa nickellegeringar. Denna korrosionsmekanism får som konsekvens att materialen bedöms felaktigt. Det är då inte möjligt att hitta någon koppling mellan hur materialen beter sig under de accelererade testerna, där de presterar dåligt, och ute i den verkliga världen hos användaren, där materialen presterar mycket väl. Denna nya kunskap kan tillåta industrin att utveckla nya och mer trovärdiga accelererade testprotokoll för att mäta korrosionsmotståndet av nickellegeringar.

De sista fyra artiklarna i avhandlingen (**Paper VI**, **Paper VII**, **Paper VIII**, och **Paper IX**) är dedikerade till utvecklingen av yt-känsliga experimentella metoder som kan användas för att studera metallytor och de tunna oxidlager som potentiellt kan skydda dem mot korrosion.

Popular summary

This thesis covers the topic of corrosion, how it takes place, and how it can be avoided. But what is corrosion? Corrosion is when chemical and electrochemical reactions degrade and dissolve metallic materials once they are exposed to, for example, salt water or an acid. Rust forms when iron and alloys containing iron, such as steel, corrode. This happens when the metal surface is exposed to oxygen, which can be present both in the air we breathe and the water we drink. Corrosion results in huge costs annually. Up to 4% of each nation's GDP is spent on costs related to corrosion, such as service and maintenance or loss of material. The production of metals also emits large quantities of greenhouse gases. So, if we could avoid corrosion, it could save huge costs as well as have a positive impact on climate change.

Researchers have previously succeeded in developing alloys that can spontaneously resist corrosion. An alloy is a metallic material consisting of different elements. The most famous alloy is steel, which is an alloy of iron and carbon. Stainless steel, which is the most famous corrosion-resistant alloy, consists mainly of iron and chromium. When stainless steel is exposed to oxygen and water, it does not form rust, which is iron oxides and hydroxides. Instead, a chemical compound of chromium and oxygen is formed: chromium oxide. On the surface of the stainless steel, a very thin layer of chromium oxide is formed. This oxide layer is only a few atomic layers thick, only a few nanometers. This is 100,000 times thinner than a human hair.

These thin protective oxide films that spontaneously form on certain metal surfaces are known as passive films since they make a metal surface, which otherwise would react and dissolve rapidly, to become “passive” even in aggressive environments. The passivity of alloys has long been studied, but it is still debated and not fully understood. Even materials such as stainless steel can be susceptible to corrosion in certain aggressive environments, where the passive oxide film may break down and no longer offer protection.

In applications where stainless steel does not meet the requirements, for example, in the chemical industry, nuclear power and jet engines, alloys of nickel, chromium, and molybdenum can be used. A material that is not iron-based. These nickel-based alloys are known to withstand high loads and high temperatures and started to be developed in the 1950s. From many years of empirical experience within the industry, it is well known that these alloys exhibit exceptional corrosion resistance. However, the details surrounding the passive films that form on these Ni-based alloys, which give rise to their excellent corrosion resistance, are not well studied and understood. The formation, the chemical nature, and the breakdown of passive films on nickel alloys are the topics to which this thesis is dedicated.

Studying these oxide films, 100,000 times thinner than a human hair, existing at the interface between metal and an external liquid environment is not an easy task. During this thesis, I have developed and utilized experimental tools that we, as scientists, can use to study these thin, complex, and important oxide layers. Most of the results in this thesis come from experiments that have been carried out at so-called synchrotron radiation facilities. They can be compared to a large microscope that allows us scientists to “see” and study tiny things. MAX IV in Lund is such a synchrotron radiation source, a particle accelerator, 528 meters in circumference (the same circumference as the Colosseum in Rome), which generates X-rays that we use for our experiments. With the help of these large-scale facilities, we have obtained an increased understanding of these thin oxide films that provide nickel-based alloys with exceptional corrosion resistance.

At the end of the printed thesis, the scientific papers are attached. In the first three (**Paper I**, **Paper II**, and **Paper III**), the thickness and composition of the thin oxide layers that spontaneously form on the nickel-based alloys in air was studied. How the oxide film initially forms once a bare metal surface is exposed to oxygen, as well as how the effect of aging time in the air affects the oxide film composition and thickness, was also studied.

In the two later papers (**Paper IV** and **Paper V**), it was shown how the passive oxide layer breaks down during accelerated electrochemical corrosion tests. In industry, it is important to be able to make reliable accelerated tests to assess the corrosion resistance of different materials to know and predict which material can be used in which corrosive conditions during applications. A new and unknown corrosion mechanism is reported in the thesis. This is a mechanism that occurs during accelerated tests of some nickel-based alloys, which makes direct assessment during accelerated tests difficult for these alloys. It also means that there is no clear link between the accelerated tests, where the material performs poorly, and the real-world applications, where the material performs well. This new knowledge can allow the industry to develop more credible and accurate accelerated tests for these types of nickel-based alloys.

The last four papers of the thesis (**Paper VI**, **Paper VII**, **Paper VIII**, and **Paper IX**) are dedicated to the development of surface-sensitive experimental methods that can be used to study metal surfaces and the thin oxide layers that can protect them from corrosion.

Acknowledgments

First of all, I would like to acknowledge **Edvin Lundgren**, my main supervisor and mentor during my PhD studies. I am grateful for all the opportunities, support, freedom, and trust that you have given me, which has allowed me to evolve as a scientist and as a person. You have given me the room to really grow, but you were also always present to steer me back on track if needed. I am forever grateful!

Gary Harlow, my co-supervisor, thanks for being patient with me during my master's thesis and the beginning of my PhD. And thanks for teaching me the basics of electrochemistry. Thanks also to **Johan Zetterberg**, my second co-supervisor. Thanks for creating a good work environment that allows for great scientific collaboration between our divisions. I have always felt very welcome in combustion physics.

I also want to acknowledge **Jinshan Pan** from KTH. Since around halfway through my PhD, when I switched projects, you have been like a mentor and an in-official supervisor to me. I am grateful for everything you have taught me about electrochemistry and corrosion. It has also been a pleasure to work together during numerous beamtimes and travel to conferences together.

Lindsay Merte, thanks for your razor-sharp, straightforward, and constructive comments. Your scientific integrity is an inspiration!

Fredrik Höök, thank you for all our interesting discussions and your wise suggestions. I appreciate the time we spent together a lot.

Giuseppe Abbondanza, TVB! I still remember the nightshifts we did during the first beamtime I joined, which was at the APS in Chicago. We had a lot of espresso and a lot of interesting discussions. Since then, we have had many vacations, beamtimes, deep scientific discussions, and, most importantly, good times. I hope that we will continue to have all of the above! **Monica**, thanks for all the times I could borrow Giuseppe, and thanks for your hospitality both in Malmö and in Italy.

Andrea Grespi, without you, the last years of my Ph.D. would have been much less fun and much more difficult. Thanks for all the good times during beamtimes, traveling, and vacations. Sei come un fratello per me.

Konstantin Simonov, thanks for all the discussions on XPS fitting and quantitative data treatment. It is always a pleasure to meet, chat, discuss, have a beer, or enjoy a conference dinner in Brussels.

Xiaoqi Yue, thanks for all the help with the countless beamtimes. Your hard work and dedication during night shifts have definitely impacted this thesis positively! I wish you all the best with your career.

Josefin Eidhagen, thanks for the help with all the sample preparation and help during beamtimes.

Giulio D'Acunto, thanks for all the good times spent together both at and outside work. I learned a lot about XPS from you. Thanks for that!

The Combustion Physics team: **Sebastian Pfaff!** Thanks for all the fun times during after-work, late-night lab sessions, and beamtimes. **Lisa Rämisch** and **Sabrina Gericke**, thanks for the help with beamtimes and for the fun after-work and parties.

Volkmar Koller, it was a pleasure to help with your beamtime, and I am happy that you could help with mine. Thanks for all the good discussions and the suggestions for good music!

The P21.2 team: **Ulrich Lienert**, thanks for all the guidance and support during experiments and data analysis. **Zoltan Hegedüs**, thanks for all the help with our experiments, especially the macros!

The FlexPES team: Thanks, **Alexei Preobrajenski**, for the help with my first XPS measurements during the COVID-19 pandemic. It turned out to be a good paper, I think! Since then, thanks for the support with experiments. Thanks also to **Alexander Generalov** and **Stephan Appelfeller** for your help and support during the experiments.

The HIPPIE team: **Andrey Shavorskiy** and **Mattia Scardamaglia**, thanks for the help with beamtime applications, experiments, and data interpretation. We did not do many beamtimes at HIPPIE, but it has resulted in several nice publications so far. I will be back for more measurements!

Work should be fun! And that has definitely been ensured by all the people at SLJUS. Special thanks to alumni and current students **Ulrike, Nellie, Isac, Rosie, Virgi, Rohit, Hanna, Hanna, Sandra, Lukas, Oskar, Yen Po, Dima, Denis, Stefano, Zephyr, Ahmed, Vidar, Julia.**

Patrik, the division would not be the same without you! Thanks for answering all my questions about economics, and thanks for making the division a fun place to work! Thanks also to **Anne** for making sure that the salary keeps coming.

Thanks to the Puglia family: **Flavio, Massimo, Giovanni, Vito, Jack, and Konstantin.** Good times!

Thanks, **Erik, Claude, Fredrik, Julia, Robin, Elin, Linus, and Patrik.** I am very happy to have a network of such good, supporting friends!

Lastly, I would like to thank my sister, **Elvira**, my entire extended family, my mother, **Karin**, and my father, **Ulf.** Without your guidance, I would not be where I am today. Thanks for your unconditional love and support!

List of abbreviations

Two-Dimensional Surface Optical Reflectance (2D-SOR)

Simple Cubic (SC)

Coordination Number (CN)

Body Centered Cubic (BCC)

Face Centered Cubic (FCC)

Molecular Orbital (MO)

Inner Helmholtz Plane (IHP)

Outer Helmholtz Plane (OHP)

Potential of Zero Charge (PZC)

Standard Hydrogen Electrode (SHE)

Reversible Hydrogen Electrode (RHE)

Saturated Calomel Electrode (SCE)

Point Defect Model (PDM)

Cyclic Voltammetry (CV)

Electrochemical Impedance Spectroscopy (EIS)

Polyetheretherketone (PEEK)

Ambient Pressure X-ray Photoelectron Spectroscopy (AP-XPS)

X-ray Photoelectron Spectroscopy (XPS)

X-ray Absorption Near Edge Structure (XANES)

X-ray Fluorescence (XRF)

X-ray Diffraction (XRD)

X-ray Reflectivity (XRR)

Scanning Electron Microscopy (SEM)

Energy Dispersive Spectroscopy (EDS)

Electron Backscatter diffraction (EBSD)

Grazing Incidence (GI)

1. Introduction

We are all surrounded by metallic materials in our everyday lives. They are part of the buildings where we live and work, and our modes of transportation, cars, boats, bikes, and planes. They are essential to our industries, our ever-shrinking electronics, and part of our art and musical instruments. Even things that do not contain any metal, such as plastics, medicine, chemicals, wood, or concrete, are produced with the help of equipment, tools, or factories where metallic materials play a crucial role. The high strength, ductility, machinability, durability, and thermal and electrical conductivity make metallic materials desirable in all these applications. One can even claim that these metallic materials enable our advanced and modern society [1]. This has also been true throughout history, where societal advancements have been tied to technological developments. The fact that epochs are named after the type of metal technology used, such as the bronze and iron ages, hints towards the importance and strong tie between societal advancements and the use and development of advanced metallic materials. Nowadays, we have moved past simple iron and use several advanced alloys such as stainless and high-strength steel, aluminum alloys for lightweight applications, zirconium alloys in the nuclear industry, and Ni alloys in high-temperature and chemical plant applications.

As mentioned, metallic materials have several desirable properties, but the main factor limiting the lifetime of metallic components in service is corrosion. We have all seen it on our cars, bikes, and maybe some rusty nails around the house. That might not seem so harmful, but costs related to service and maintenance caused by corrosion result in an estimated annual bill of around 4 % of each nation's GDP [2, 3]. That is around 4 trillion USD every year! Corrosion causes enormous economic damage, and the corroded materials cannot be fully recovered and recycled, resulting in huge material waste [4]. If we then factor in the global CO₂ emissions associated with the production of metals, which is responsible for 40 % of industrial greenhouse emissions and 10% of our global energy consumption [5], it becomes clear that corrosion also results in a significant environmental footprint [6, 7]. Leaks in oil and chemical plants caused by corrosion are also severe environmental hazards, and corrosion has historically caused numerous plane crashes, collapsing of bridges, and sunken ships, resulting in the loss of human lives.

The reason why metallic materials corrode is relatively straightforward. Corrosion can be seen as the path towards thermodynamic equilibrium since most metallic materials, except a few so-called noble metals such as gold and platinum, are more

stable in their oxidized state under ambient conditions. This is also the state in which we find iron, aluminum, chromium, and most metals in nature. They are all found as ore, minerals where the metal atom exists in its thermodynamically favorable oxidation state. Suppose the oxides on a metallic surface are soluble in water. In that case, the material will degrade through a vicious cycle of oxide formation and dissolution, which can be seen as the simplest example of aqueous corrosion. Since we cannot change the laws of thermodynamics, we need to master the kinetics, or rate of oxidation and dissolution, to "control" the corrosion process. All metals and alloys, unless they are part of the few exceptions considered noble, oxidize under ambient conditions. However, some metals and alloys can form thin, stable oxide films that protect the underlying metal from further oxidation. This is now a spontaneously forming protective barrier between the metal substrate and the harsh oxidizing environment that can be the air we breathe and the water we drink.

These thin, stable, protective oxide films are called passive films since they make an otherwise active metal passive in an oxidizing atmosphere [1, 8, 9]. This phenomenon was first discovered in the 1800s when it was found that iron readily dissolves in diluted nitric acid but not in concentrated nitric acid [10]. It was postulated that the strongly oxidizing acid reacted with the iron surface and formed a thin layer of iron oxide that stopped the further aggressive dissolution of the bulk metal. Other famous examples of the phenomenon of passivity are stainless steel [11] and aluminum alloys [12], which both form thin, stable oxide films. However, metals and alloys capable of forming a thin protective oxide are not immune to corrosion. This thesis would have been dedicated to a different topic if they were. The thin passivating oxide films exist in a steady state, or kinetically trapped state, living at the border of extinction. Low dissolution rates are balanced by the formation of new oxide in a delicate fashion. Depending on the conditions, this balanced steady state can tip towards the side of oxide dissolution, and if the rate of oxide dissolution is faster than the rate of oxide formation, the metal substrate will corrode rapidly. Ever since its discovery, passivity and passivity breakdown have been extensively studied, but still, to this day, it is not fully understood. It is a fundamentally complex problem to study [13].

To experimentally observe a few nanometers of oxide at the interface between liquid and metal is not trivial, and very few techniques exist that can provide *in situ* structural and chemical information at the solid-liquid interface. Traditional studies of corrosion using electrochemical measurements have been extremely successful over the years. However, such measurement only provides indirect information, which leads to the need for speculations. To try and circumvent this, many studies have been conducted where the sample is exposed to corrosive conditions and then extracted and examined under ultra-high vacuum conditions where most surface science techniques operate [11, 14]. To this day, it is not clear how the sample surface and the protective oxide we want to observe may change upon removal from the liquid, drying, and exposure to ultra-high vacuum. There is definitely a need for

new experimental approaches to illuminate the chemistry and structure of these thin oxide films in realistic aqueous conditions.

In this thesis, a significant focus has been put on the utilization of synchrotron-based techniques to probe the structure and chemistry of passivating oxide films *in situ*. Emphasis has been placed on understanding the formation of the protective oxide and the chemistry and thickness of the native air-formed oxide films that make the starting point for our subsequent studies. A second focus has been to understand how these oxide films evolve and eventually breakdown under simulated corrosive conditions with the help of electrochemistry. Lastly, this thesis also covers some methodology development where we have focused on different ways to combine surface sensitivity, chemical sensitivity, and the possibility of probing the surface through a liquid environment. However, obtaining a microscopic view of the surface processes that occur in our electrochemical cell is also important. Therefore, we have developed an optical technique known as Two-Dimensional Surface Optical Reflectance (2D-SOR) that we have combined with our electrochemical cell. So, in short, this thesis covers the development and utilization of novel *in situ* and synchrotron-based techniques to gain a deeper understanding of the formation and breakdown of passive films.

2. Materials

In this chapter, a basic description of the materials studied in this thesis will be given. The crystalline bulk metal and the Ni-based alloys studied in this thesis will be introduced, followed by a description of relevant oxide structures. The concept of surfaces will be discussed, which is important to the fields of corrosion and electrochemistry since the reactions occur at the surface. The thin amorphous oxides that make up the passive films will be introduced.

Crystals and alloys

A crystal is a solid state of matter where the building blocks of atoms or molecules are arranged in a long-range periodic pattern. But what is the driving force for the ordering of atoms? The answer to this question lies in thermodynamics, where we need to consider the change in the Gibbs' free energy, ΔG . For a given temperature, T , ΔG is given by Equation (1), where ΔH is the change in enthalpy and ΔS is the change in entropy.

$$\Delta G = \Delta H - T\Delta S \quad (1)$$

A system always strives to minimize its free energy, so if ΔG is negative, the reaction or transformation is energetically favorable. For the formation of a crystal, ΔS is typically negative since the positional degree of freedom of the atoms decreases when they are assigned to well-defined sites in a crystal compared to that of a liquid or amorphous solid. The term $-T\Delta S$ is hence positive, meaning that the change in enthalpy must be negative for the formation of a crystal. When a crystal is formed, a large number of favorable bonds are made, resulting in a lowering of the enthalpy (energy), and when ΔH is sufficiently negative, it can drive crystal formation. In a crystal where the atoms are ordered in a periodic arrangement, they maximize the number of favorable bonds to the neighboring atoms compared to unordered solids known as amorphous materials.

As stated earlier, crystals are solids with a long-range periodic ordering of atoms. The arrangement of atoms can be described as a periodic crystal lattice, and to define its structure, it is conventional to consider the smallest repeating unit, termed the

unit cell. The unit cell is defined by the length of the unit cell sides and the angles between them. The simplest class of crystal structures are the cubic structures where all the angles are 90° , and all the sides of the unit cell are of equal length. The Ni-based alloys studied in this thesis have a cubic crystal structure. Here, only the cubic crystal structures will be introduced, but there are many more possible periodic arrangements of atoms in nature.

The most simple crystal structure is the Simple Cubic (SC), defined by a cubic unit cell with one atom in each corner. Each atom in SC binds to 6 other atoms, so the Coordination Number (CN) is 6. If one atom is placed at the center of the SC unit cell, a Body-Centered Cubic (BCC) crystal structure is made. The CN of the atoms in a BCC structure is 8. If atoms are placed at the face of each side of the SC, a face-centered cubic (FCC) structure is realized where the CN is 12. FCC is the most close-packed crystal structure (together with the hexagonally close-packed), and there is no possibility of arranging the atoms to achieve a denser packing. The cubic unit cells are shown in Figure 1 both as open ball and stick models to illustrate the atomic arrangement clearly and more realistically as a densely packed arrangement.

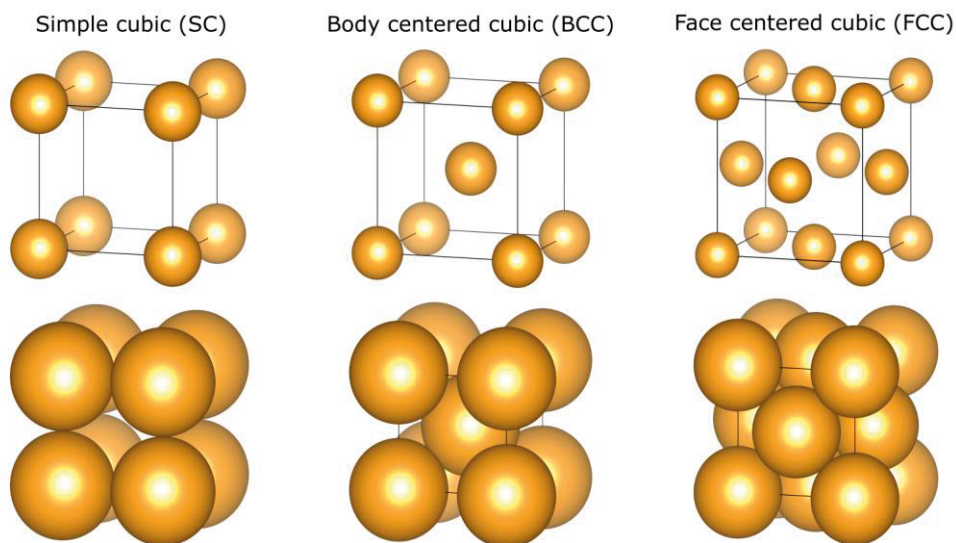


Figure 1: Unit cells of the cubic crystal structures are shown both as open and, more realistically, as densely packed spheres.

Alloys are metallic solid solutions where atoms of different elements are mixed in a structurally non-ordered fashion. The atoms of the different elements randomly occupy sites in the crystal lattice. Steel, for example, is an alloy of iron and carbon.

Stainless steel is an alloy of mainly iron and chromium but may also contain significant amounts of molybdenum and nickel. Most industrial materials are alloys with a complex composition. Many criteria must be optimized when designing an alloy, such as high strength, low creep rate, good corrosion resistance, and good machinability. Many different alloying elements might affect these properties in different ways. Empirically, chromium and molybdenum are, for example, well known to increase the corrosion resistance of an alloy. The hardening of alloys is often achieved by precipitation hardening, where small precipitates form in the microstructure. Specific alloying elements are added to facilitate the formation of these small particles, but this might not be good for corrosion resistance. When designing an alloy, there is always a balance between all the different properties one would like to obtain. However, a more intelligent approach to alloy design could be achieved with a fundamental understanding of how the different alloying elements behave and interplay during the oxidation and corrosion process.

Ni-based alloys

Most of the work carried out in this thesis is based on the study of a class of industrial Ni alloys, namely Ni alloy 59, Inconel 625, and Inconel 718, with the composition shown in Table 1.

Table 1: Elemental composition of the studied Ni-based alloys in wt%.

Grade	UNS No	Ni	Cr	Mo	Fe	Nb
Alloy 59	N06059	60.07	22.70	15.40	0.80	-
Alloy 625	N06625	61.53	21.53	8.63	4.38	2.32
Alloy 718	N07718	52.28	18.34	2.91	19.50	5.10

These alloys are used in demanding applications and in harsh environments, especially at high temperatures in combination with high mechanical strain, for example, in gas turbines, sour oil and gas wells, the nuclear industry, and the chemical industry [15]. These alloys are known for their excellent mechanical and corrosion properties even at elevated temperatures and in very corrosive media [16-20]. Out of the three alloys, a main focus has been placed on Ni-59, which is an alloy containing mainly Ni, Cr, and Mo (Ni-Cr-Mo), which is the simplest of the three and can serve as a sort of model system. Simplifying the system can be of great help in unveiling the intricate and complex mechanisms associated with the corrosion of industrial alloys.

Oxides

The metals we rely on in our society, such as iron, aluminum, chromium, nickel, and copper, are all found in an oxidized state in nature. This is the most thermodynamically stable state of most metal atoms. To obtain the metallic state, the ore must be reduced. This has historically been done for iron by heating the ore in a coal fire, which emits enormous amounts of CO₂ annually [21]. There are now many initiatives to use electrochemically evolved hydrogen to reduce the metal ore, which would greatly reduce CO₂ emissions [22]. Energy must be supplied to reduce the metal oxide into the metallic state to be used in applications. When exposed to an oxidizing environment, most metals are then transformed back towards thermodynamic equilibrium, which means they are re-oxidized.

Metal atoms have an electronic configuration where losing electrons bring the atom closer to the electronic configuration of a noble gas (which is the most stable). These electrons, or charge density, that the metal atom wants to donate need to go somewhere. This is where oxygen comes in. Oxygen wants to gain electrons to fill up the outer shell and achieve a noble gas electron configuration. The metal cations and oxygen anions can form a solid with strong ionic bonds that can be crystalline or amorphous. The chemical bond strength of a material can be estimated from the melting temperature, which, in principle, is how much thermal energy one needs to provide to break the chemical bonds of the solid. Oxides generally have much higher melting temperatures than pure metals [23, 24], indicating that metal-oxygen bonds are stronger and more stable than metal-metal bonds. The most important oxides in this thesis are those of Cr and Mo. The most stable oxidation state of Cr is 3⁺ with an oxide stoichiometry of Cr₂O₃. For most corrosion-resistant alloys, Cr and its oxide play a significant role in the formation of a stable oxide film. Mo has several stable oxidation states, but the ones found in this thesis are Mo⁴⁺ (MoO₂) and Mo⁶⁺ (MoO₃). The oxide structures of Cr₂O₃, MoO₂, and MoO₃ are shown in Figure 2. As seen, both Cr₂O₃ and MoO₂ form a solid network, while MoO₃ shows a layered structure without a continuous network of metal-oxygen bonds. This could explain the thermal instability of MoO₃, which was seen to disappear from the oxide film upon heating [25]. Moreover, Mo was also found in the oxidation state of 5⁺ in the oxide films on the Ni alloys in this thesis. There is, however, no well-defined structure for the Mo⁵⁺ oxidation state. Its presence can be attributed to the very disordered nature of the thin oxide films, a complex mixed oxide stoichiometry, associated with defects in the oxide film, or be attributed to Mo⁴⁺ hydroxide.

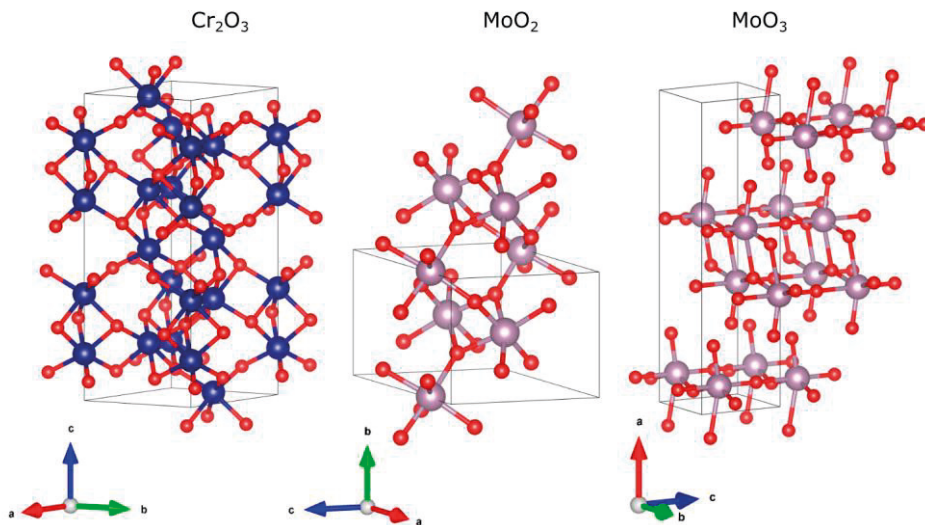


Figure 2: Atomic structure of oxides of chromium and molybdenum (Cr_2O_3 , MoO_2 , and MoO_3) important for this thesis. The structure of MoO_2 and MoO_3 was extended beyond the unit cell marked in black for better visualization. The structures are drawn using VESTA [26] with atomic coordinates from Refs [27-29]. The arrows denote the crystallographic axes of the unit cells.

Surfaces and atomic planes

In crystallography, it is important to be able to denote directions and lattice planes in a crystal, as will be seen when talking about X-ray diffraction. To define directions and planes, Miller indices are used, consisting of three integers: h , k , and l . The three integers can define a direction, denoted as $[hkl]$, a plane normal to that direction (hkl) , a family of directions $\langle hkl \rangle$, or a family of planes $\{hkl\}$. To determine the Miller index for a specific lattice plane, one must first find where the plane intercepts the unit cell's axes. To have the same notation for parallel planes, the convention is set to take the intercepts' inverse and convert them to the smallest possible integers. The three principal low-index planes defined by the Miller indexes (100) , (110) , and (111) for the FCC structure are shown in Figure 3, together with their surfaces. All electrochemical reactions, including oxidation and dissolution, take place at the surfaces of materials. Surface structures are therefore important and determine the function of the material. The atomic arrangement at the surface will be different depending on how a crystal is terminated. The (111) surface is the most close-packed plane with a CN of 9 since each atom at the surface bonds

to 9 other atoms. As shown earlier, bulk FCC has a CN of 12, so the surface atoms are less coordinated than bulk atoms, which changes the chemistry at the surface compared to the bulk. The CN for the (110) surface is 7, and the CN for the (100) surface is 8.

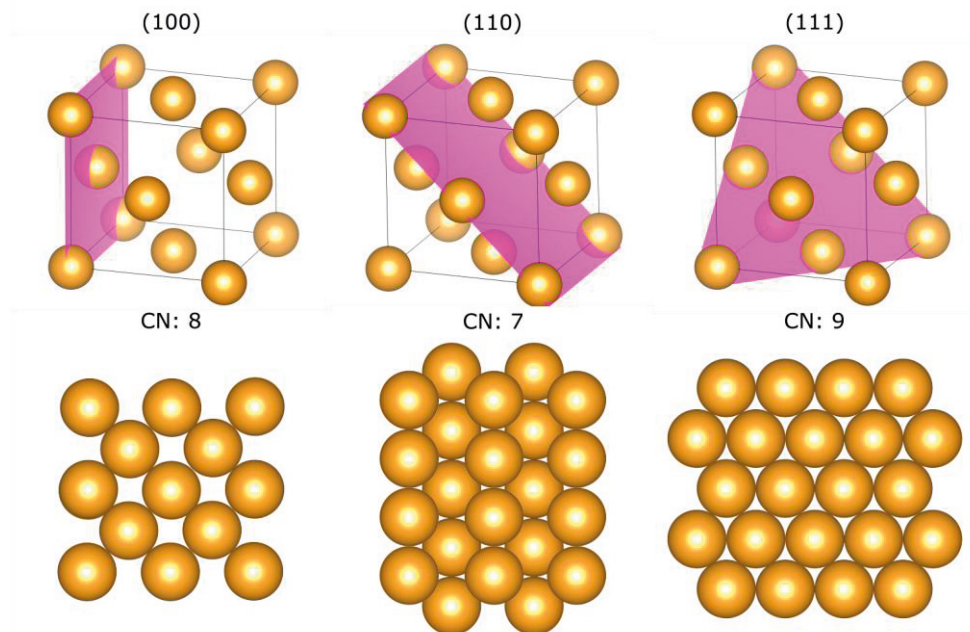


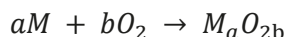
Figure 3: Top: Lattice planes defined by Miller indexes (100), (110), and (111) drawn in an FCC unit cell as pink. Bottom: The atomic-scale structures of the (100), (110), and (111) surfaces.

Thin oxide films on metal surfaces

Corrosion protection of passive metals and alloys is almost exclusively governed by nanometer-thin oxide films on metal surfaces. Studying these thin oxide films and their structural and chemical properties is the main focus of this thesis. While the metal substrate is crystalline and well-defined, the oxide films that form on the surface at room temperature are, to a large extent, amorphous. There are reports that the atoms in the oxide films can have some degree of local ordering in the form of nanocrystalline domains [30-33]. However, such ordering was not observed for the thin oxide films on the Ni-based alloys studied in this thesis.

As stated above, according to thermodynamics, a piece of steel or Ni-based alloy should completely oxidize when exposed to oxygen, and there should be no metal

left at equilibrium. However, that is not what is observed practically. What happens when a bare metallic surface is exposed to oxygen? When writing down the chemical reactions, the metal atoms, M , will react with oxygen molecules to form a metal oxide, where a and b define the stoichiometry of the oxide that depends on the oxidation state of the metal M .



But which metal atoms do react? And do they react with oxygen atoms or oxygen molecules? In “dry” oxidation, it is oxygen molecules that are the supply of oxygen. But for the oxidation reaction to occur, the oxygen molecules need to dissociate. The oxygen-oxygen bond of the molecules needs to be broken before they can react to form metal oxide. Many metal surfaces are good catalysts for oxygen dissociation and can, therefore, supply the metal atoms at the surface with reactive oxygen atoms [34-36]. Electron donation can take place, and chemical bonds can be formed. This is the initial stage of oxidation, the formation of the first monolayer of oxide. But what happens when a monolayer of oxide has formed on the surface? There is now a barrier between the two species that should react, metal and oxygen, in order for the oxide to grow further. Here, we need to consider the diffusion in solids at room temperature (in this thesis, most experiments were carried out at room temperature). We also need to consider whether oxygen molecules can still dissociate. After the formation of one monolayer of oxide, it is the oxide surface that is exposed to the surrounding environment, which completely changes the energy landscape for interactions with molecules. For a diffusion coefficient of 10^{-27} m²/s (for oxygen in vanadium oxide, taken from Ref [37]), the time required to diffuse 1 nm according to random walk is 10^9 seconds. That is around 30 years! From this simple estimation of the rate of solid diffusion at room temperature, we can clearly see that there must be something else that drives the mass transfer during oxide growth.

More than 70 years ago, Cabrera and Mott developed a theory of the oxidation of metals [38, 39]. They postulated that a strong electric field builds up across the thin oxide film that can drive ion migration, which has then been experimentally confirmed [40]. Considering a monolayer of metal oxide as the starting point, we now want to understand how it can further grow. First, oxygen molecules adsorb and dissociate into atomic oxygen at the oxide surface. Second, electron tunneling can occur across the thin metal oxide (metal oxides are, in general, assumed to be insulators and non-conductive, therefore, electron transport across this barrier occurs by tunneling). Here, it is also assumed that the movement of electrons and ions across the interface can happen independently of each other. The electrons that tunnel from the metal substrate to the oxygen atoms adsorbed on the surface generate oxygen anions at the surface. We now have a potential difference between the metal and the oxide surface, which results in an electric field with an electric field strength, E , as described in Equation (2),

$$E = \frac{V}{d} \quad (2)$$

where V is the potential drop across the oxide film, and d is the oxide film thickness. The potential difference is in the order of magnitude of 1 V, which results in a very large electric field, on the order of $1e7$ V/cm, when considering that the oxide thickness is on the order of a few nanometers (around 1-2 nanometers for the oxide films formed on the Ni alloys studied in this thesis). In this electric field, metal cations can move through the oxide film by field-assisted migration. The cations can then form ionic bonds with the oxygen anions at the surface and, in this way, build up the oxide lattice. A schematic illustration of this proposed mechanism is shown in Figure 4 a).

The rate of ion migration is orders of magnitude slower than the electron tunneling across the oxide. With a steady supply of oxygen, this results in a steady state where there will always be a potential drop across the oxide since the oxygen anions form much faster than the supply of metal cations to the oxide surface. Isotopic labeling experiments have shown that it is indeed, to a large extent, the metal cations that move in the electric field [41]. This can be due to the higher charge of most metal cations (Cr^{3+} and Mo^{6+} , which play a central role in this thesis) compared to the O^{2-} ions. The metal cations should, therefore, experience a larger force in the electric field. The radius of metal cations is also smaller than that of oxygen anions [42]. The rate of cation transport, dictating the rate of oxidation, depends on the strength of the electric field. The electric field strength depends to some degree on the Mott potential but mainly on the oxide thickness separating the charges of the oxygen anions and metal cations. As the oxide grows thicker, the electric field strength decreases, resulting in a decreasing oxide growth rate. This results in a logarithmic description of oxide growth (the integral of the growth rate, which is proportional to $1/d$), as shown in Figure 4 b), which depicts the oxide thickness for a Ni-Cr-Mo alloy measured using XPS (which will be introduced later) as a function of time in 10^{-8} mbar of oxygen. However, a logarithmic function never reaches an asymptotic value, so according to this model, the oxide growth would continue forever only at evermore decreasing rates. What experimentally is observed is that the oxide film stops growing completely at some point once a so-called self-limiting thickness is reached. What defines this thickness? Here, we again need to consider the dissociation of the oxygen molecules at the surface. It was shown that the limiting thickness for aluminum oxide on aluminum was caused by the diminishing driving force for the dissociation of molecular oxygen at increasing oxide thicknesses [43]. So, at some oxide thickness, it is no longer favorable to dissociate oxygen molecules at the oxide surface, which is necessary to further drive the oxidation reactions.

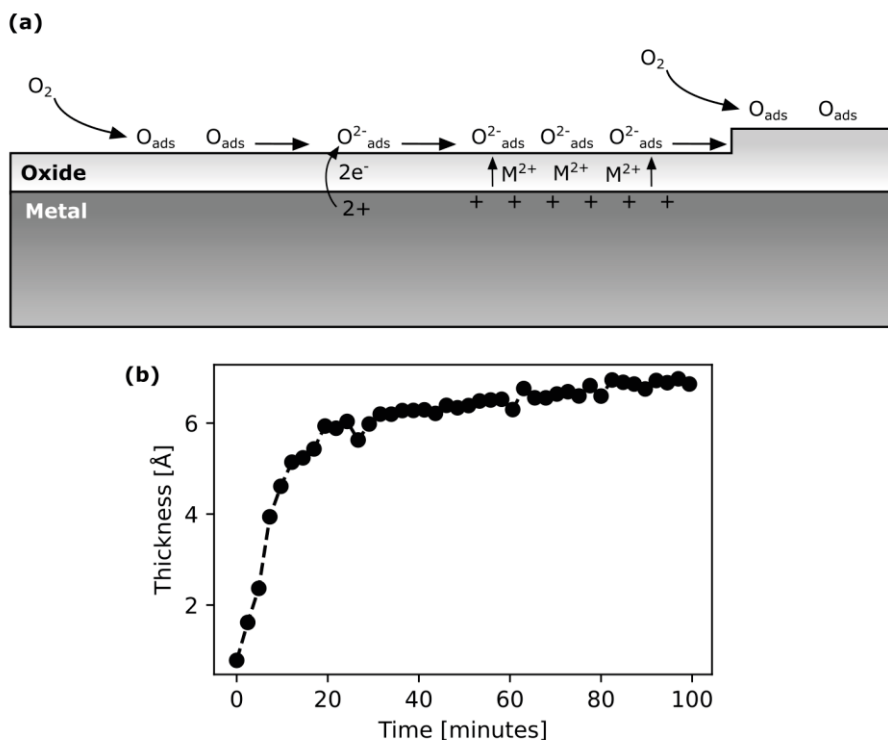


Figure 4: a) Schematic of the Cabrera Mott model for oxide growth on metal surfaces. b) Oxide thickness as a function of oxidation time for a Ni-Cr-Mo alloy determined using XPS in 10^{-8} mbar of oxygen.

The above model was developed for “dry” oxidation, which means only in the presence of O_2 . Then, we may wonder if the formation of so-called native oxides (oxides grown spontaneously in air) on industrial alloys follows this model. The answer is yes, as far as we know [35]. But in air, with some level of humidity, water also needs to be considered. At sufficient humidity, surfaces can even be covered by a thin (nanometers) layer of liquid water [44]. This means that what we might consider “dry” oxidation in normal ambient air, in reality takes place in a liquid environment at the surface. This we can observe experimentally in the form of hydroxide groups present on the surface after oxidation in air. Hydroxylation of the oxide surface should not take place in the presence of only oxygen. There are also reports in the literature of hydroxide layers several nanometers thick after oxidation in air. This could indicate that some dissolution of the oxide film has occurred and that metal ions dissolved in the solution are hydroxylated and precipitate at the oxide surface. These phenomena cannot be described by simply considering “dry” oxidation.

3. Electrochemistry

Fundamentals

Electrochemistry is a branch of chemistry that is concerned with chemical reactions coupled to the transfer and flow of electrons across a solid-liquid interface. The flow of electrons is what is known as an electrical current, and an electrical current flows in the presence of a complete electrical circuit and a potential difference. Electrochemistry concerns the transfer of electrons between two phases: one electrical conductor (metals or semiconductors) and one ionic conductor. In this thesis, we will only consider aqueous solutions containing electrolyte species such as Na^+ , Cl^- , H^+ , and OH^- . The birth of electrochemistry can be seen as Alessandro Volta's discovery of the first working battery in the beginning of the 19th century [45]. This was a stack of different metals, namely copper and zinc, with a layer of electrolyte in between, which resulted in the generation of electrical energy and a potential difference, with a unit given by the name of the inventor, between the bottom and the top of the metal stack. So why do two metals submerged in an electrolyte generate a potential difference that can drive an electrical current?

At the surface of the two metals, or so-called electrodes, redox reactions are taking place that involve electron transfer. Neither copper nor zinc are noble metals, so both would spontaneously oxidize if not being electrically connected. However, when the two electrodes have an electrical connection, electrons can flow. This means that at one electrode, electron transfer will take place from the electrode to a species at the electrode surface or in the solution. This is known as a reduction reaction since the donation of a negative charge will decrease the oxidation state of the reacting species. At the other electrode, electrons will be transferred from a species at the electrode surface or in the solution to the electrode. This is an oxidation reaction since the oxidation state of the species increases upon losing electrons. Copper is more noble relative to zinc, which means that there is less driving force for copper to be oxidized. This, in turn, means that when connected, an oxidation reaction will take place at the zinc electrode, and the metallic zinc surface will oxidize. This will be coupled with a reduction reaction at the copper electrode surface where copper ions in the solution will be reduced, as shown in Equations (3) and (4). This builds up a potential difference between the two metals and an electrical current will flow. [46]



An external potential can also be applied to drive or force electrochemical reactions. The oxidation and reduction reactions can then be illustrated, as shown in Figure 5. When a positive potential is applied to an electrode surface, the energy of the electrons in the metal decreases, which is also associated with a decrease in the Fermi-level energy. The Fermi level can then overlap with the energy level of an occupied molecular orbital (MO) of a species in the solution (or with an electronic state of the metal atoms at the electrode surface which results in surface oxidation, which plays a crucial part in the formation of passive films as we will see later). Electron transfer can then occur from the molecule to the electrode, which will be an oxidation reaction. In contrast, if a negative potential is applied, the energy of the electrons in the metal electrode, and the Fermi level energy, will increase and can align with an unoccupied MO of a species in solution. Electron transfer can then occur, which corresponds to a reduction reaction of the solution species. [37][47-49]

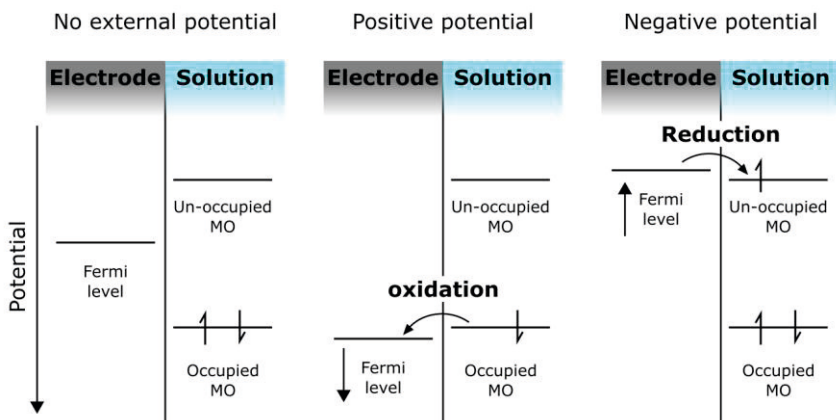


Figure 5: Crude schematic of the electronic structures and potentials to illustrate the concept of oxidation and reduction reactions at the electrode solution interface.

So far, we have only considered electron transfer as tunneling from one phase to another without much detail. Rudolph A. Marcus developed the theory of electron transfer in the 1950s [50, 51], for which he received the Nobel Prize in chemistry in 1992 [52]. Electron transfer is very rapid compared to nuclear motion. This implies that as an electron is transferred from one phase or species to the other, the

arrangement of the atoms and molecules is completely static, almost as if they were frozen. That is how fast electrons are transferred. This, in turn, has some implications. When an atom is oxidized or reduced, there is no time to rearrange its environment. When looking at the free energy curves of the reactants and products, as shown in Figure 6, we can see that the overall free energy can be minimized when moving from the reactants to the products. But since electron transfer is so rapid that no rearrangement of the atoms and molecules can occur, it means that an electron transfer is also associated with a reorganization energy, similar to the activation energy in thermally driven reactions. Just like the classical thermal activation energy, the reorganization energy in Marcus' theory of electron transfer can be overcome by the thermal kinetic energy of atoms and molecules.

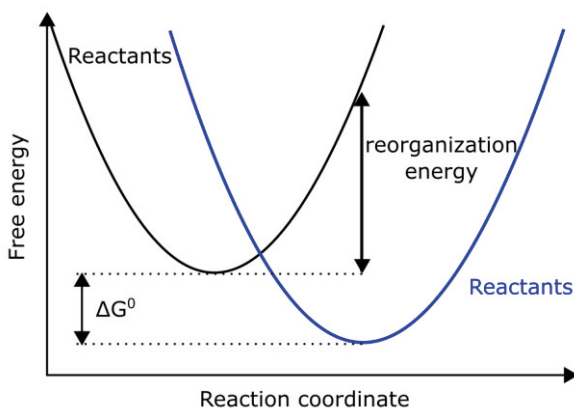


Figure 6: Free energy landscape of electron transfer along the reaction coordinate or nuclear coordinate. The rapid electron transfer is also associated with a reorganizational energy of the reactants towards the products.

Next, let us take a look at where the electron transfer reactions actually take place, which leads us to ask: what does the solid-liquid interface look like? Let us here only consider the interface of a pure metallic surface in contact with an electrolyte. In the following chapter, we will also consider a thin oxide on the metal surface. Depending on the charge of the metal surface, it will be balanced by the attraction and adsorption of cations in the case of a negative surface charge and anions in the case of a positive surface charge. There will also be some preferred orientation of the polar water molecules at the surface. Let us consider a positively charged surface. The surface charge will be balanced by counterions, here anions, that screen the electrolyte further out from the surface charge of the metal. The anions can be specifically adsorbed at the surface (the region known as the Inner Helmholtz Plane (IHP)). The anions can also be fully solvated at the surface in the so-called Outer Helmholtz Plane (OHP). Further away from the surface, there will be a diffuse layer

with decreasing anion concentration that eventually reaches the bulk electrolyte value. A schematic of this electrochemical double-layer region and the resulting potential drop from the surface out towards the solution is illustrated in Figure 7. When an electrochemical potential is applied to an electrode, this will result in the formation of this double-layer structure. To achieve this, both ions and electrons must move, which results in the charging of the surface in the same way as a classical capacitor. There will also be an external potential versus a given reference point, where the electrode surface polarity changes from negative to positive. This point is known as the potential of zero charge (PZC), at which the capacitance of the double layer reaches a minimum. [46, 47].

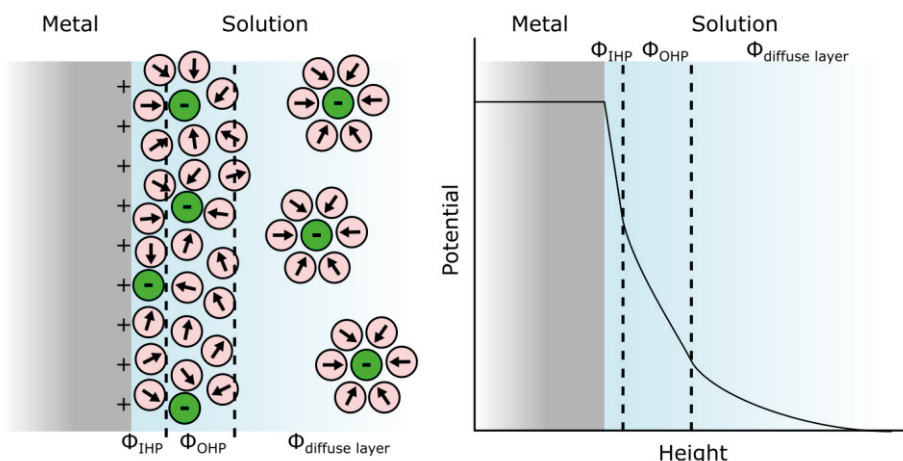


Figure 7: Schematics of the electrochemical double layer and the associated potential distribution into the solution phase.

In order to do well-defined and repeatable experiments in electrochemistry, we need to control the potential. This is done by always measuring and applying a potential difference with respect to a well-defined so-called reference electrode. This is an electrode at which the potential is static under the experimental conditions. Throughout this thesis, an Ag/AgCl reference electrode has been used. This is, in principle, a silver wire in an aqueous solution of KCl. The wire and solution are contained inside a compartment with a semipermeable membrane towards the bulk electrolyte used in the experiment. All standard potentials in electrochemistry are given with respect to the Standard Hydrogen Electrode (SHE), which serves as a universal standard reference. The most common reference electrodes and their shifts with respect to the SHE are given in Table 2.

Table 2: The most common reference electrodes and their shift versus SHE.

Reference electrode	Shift [mV]
Standard hydrogen electrode (SHE)	0
Reversible hydrogen electrode (RHE)	-pH*59
Ag/AgCl	-197
Saturated calomel electrode (SCE)	-241

In an experimental electrochemical cell, three electrodes are used, as shown in Figure 8. The working electrode, which is the sample of interest, the reference electrode described above, and a counter electrode. The potential and current are measured and controlled by an instrument known as a potentiostat. The potential is controlled and measured between the working electrode and the reference electrode, while the current flows between the working electrode and the counter electrode. In order not to limit the current measurement, the counter electrode should have a large surface area and be of an inert material to not contaminate the system. In this thesis, a Pt rod or coiled wire was used as the counter electrode. To maintain a current flowing through the electrochemical cell, there will be an oxidation reaction happening at one electrode surface and a reduction reaction at the other. This is also coupled with the movement of ions in the solution, which can close the circuit and compensate for any buildup of charge at the two electrodes. The potential applied defines if the oxidation reaction occurs at the working electrode or at the counter electrode. From here on, we will use the term anode for the electrode where the oxidation reaction occurs and the term cathode for the electrode where the reduction reaction occurs.

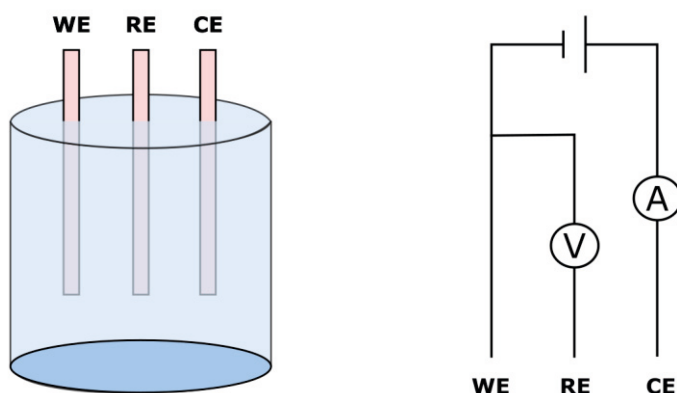


Figure 8: (right) Schematic of a three-electrode electrochemical cell with working electrode (WE), reference electrode (RE), and counter electrode (CE). (left) A crude description of the circuit inside the potentiostat.

Traditionally, in chemistry, energy is supplied in the form of heat, and there are energy barriers, or activation energies, for reactions to take place due to the energetic cost of breaking bonds before new bonds can be formed. In electrochemistry, the electrochemical potential is the driving force for electron transfer and, hence, electrochemical reactions. The Butler-Volmer equation describes the kinetics of a single electron transfer reaction, giving the relation between the current, j , and applied potential, E , as shown below in Equation (5) [53]. Here, j_0 is the exchange current density, a_a is the anodic charge transfer coefficient, a_c is the cathodic charge transfer coefficient, z is the number of electrons involved in the electrode reaction, F is the Faraday's constant, R is the universal gas constant, T is the temperature, and $\eta = E - E_{eq}$ is the overpotential, where E_{eq} is the equilibrium potential.

$$j = j_0 \left\{ \exp \left[\frac{a_a z F \eta}{RT} \right] - \exp \left[- \frac{a_c z F \eta}{RT} \right] \right\} \quad (5)$$

The Butler-Volmer equation states that the rate of electrochemical reactions, which is proportional to the current, increases exponentially with the applied potential above the equilibrium potential for a given reaction. The equilibrium potential is calculated from the Nernst equation, as shown in Equation (6) [46],

$$E_{eq} = E^0 + \frac{RT}{nF} \ln \left(\frac{[Ox]}{[Red]} \right) \quad (6)$$

where E^0 is the standard potential, which is a thermodynamic property unique to every electrochemical reaction or redox couple.

As stated above, the electrochemical current is directly proportional to the number of electrons transferred every second. More precisely, one Ampere is equal to $6.24 \cdot 10^{18}$ electrons per second. Michael Faraday realized that it is then straightforward to calculate how much products have formed for a certain amount of charge passed through the electrochemical cell, where the total charge is the time-integrated current. Faraday's law of electrolysis, which describes the mass of product produced, is shown in Equation (7) [46],

$$m = \frac{QM}{vF} \quad (7)$$

where Q is the total electrochemical charge transferred during the reactions, M is the molar mass of the product, and v is the number of electrons involved in the reaction.

The Butler-Volmer equation is similar to the Arrhenius equation in that it is an exponential equation determining the kinetics, or rate of a chemical reaction, as a

function of energy. The Arrhenius equation is shown below in Equation (8), where k is the rate constant, E_a is the activation energy.

$$k \sim \exp\left(\frac{E_a}{RT}\right) \quad (8)$$

The most significant difference between the Arrhenius and Butler-Volmer equation is that in electrochemistry, the rate is not only governed by temperature but, more importantly, by electrical potential.

The Butler-Volmer equation does, however, not consider the concentration of species at the electrode surface, multi-step reactions, or solvation effects. During electrochemical reactions, species are consumed and formed at the electrode surface, altering the local concentration of products and reactants. These effects can also influence the kinetics of electrochemical reactions.

Passivity

The phenomenon of passivity was briefly touched upon in the introduction, but let us now delve deeper into this topic. Let us first look at it from an electrochemical point of view with a simple polarization curve where the electrochemical current is plotted against the electrochemical potential, as shown in Figure 9. According to the Butler-Volmer equation, we expect the current of an electrochemical reaction to increase exponentially as we increase the potential. At increasing cathodic polarization, we see an increasing current due to the hydrogen evolution reaction where protons are reduced. At slightly more positive potentials, the current initially increases, followed by a rapid decrease in what is known as the active region. As the potential is further increased, the current density remains at very low values ($\mu\text{A}/\text{cm}^2$) in a large potential window. This is the definition of the passive region, where the potential can be further increased without an increase in the electrochemical current. At sufficiently large anodic potentials, the current will increase in what is known as the transpassive region. Now that we have seen some experimental evidence of passivity, let us try to work out how passivity is achieved and how it may break down. [54]

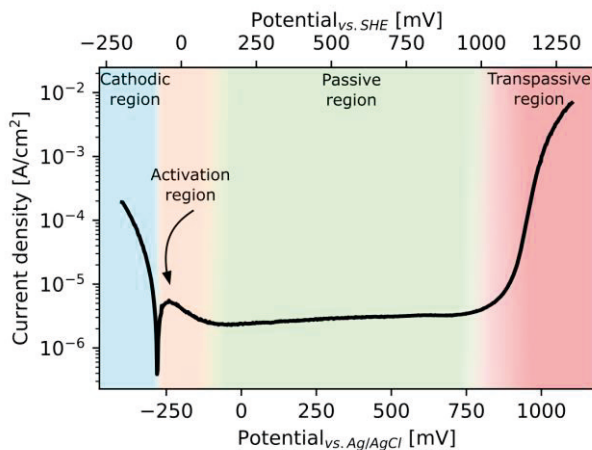


Figure 9: Polarization curve of Alloy 59 in 1 M NaCl at pH 2.

Passive film growth

In Chapter 2, the Cabrera Mott model for thin oxide film growth was introduced for gas phase oxidation. Here, we will consider how oxide films grow in an electrochemical environment. This is described by the Point Defect Model (PDM) developed by Digby Macdonald [1, 9, 55]. In the PDM, the oxide structure is thought to consist of an oxide layer between the metal and solution phases, as shown in Figure 10. Similar to the Cabrera Mott model for dry oxidation, this model only considers the growth (or destruction of the film resulting from a negative growth rate) and not the initial oxide formation from the bare metal surface. The thin oxide layer is considered as a highly defective semiconductor containing metal cations, oxygen anions, as well as cation and anion vacancies. The oxygen vacancies are created at the metal/oxide interface, and cation vacancies are created at the oxide/solution interface. These vacancies can move across the film to annihilate at the opposite interfaces (oxygen vacancies are consumed at the oxide/solution interface, and cation vacancies are consumed at the metal/oxide interface). The outer hydroxide layer in the PDM originates from the hydroxylation and deposition of ejected cations from the oxide layer. Since we now consider oxide growth in the electrochemical realm, we also need to include the electrochemical potential. For a metal in solution, there will always be a potential drop across its surface (unless the metal surface is at the potential of zero charge), either due to the open circuit potential or due to external polarization. This will result in a potential drop across the oxide layer. Since we have a potential drop across the physical dimension of the thin oxide layer (thickness in the range of one or a few nanometers), there will be a large electric field across the oxide layer, similar as in the Cabrera Mott model, as shown in Figure 7.

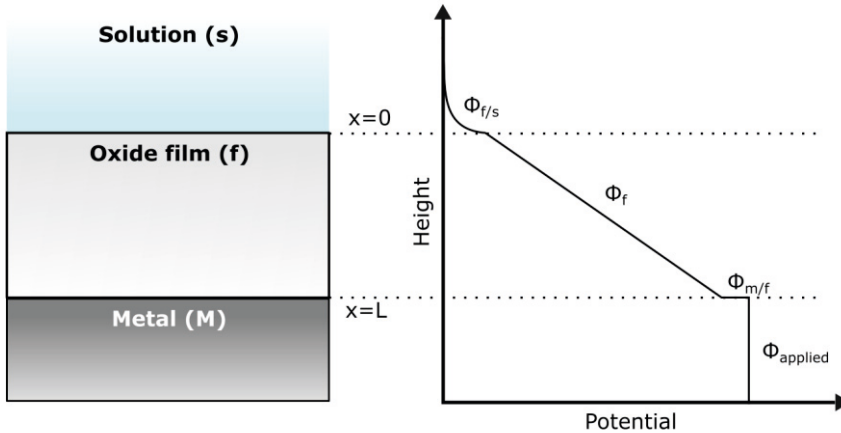


Figure 10: Oxide structure according to the PDM and the corresponding potential drop across the interface.

Now, let us consider the most important reactions that can take place at the metal/oxide and oxide/solution interfaces, as shown in Figure 11. At the metal/oxide interface, the metal atoms can be oxidized and incorporated into the oxide lattice. This can be done either by filling a cation vacancy, as in equation (1) in Figure 11, or by creating an oxygen vacancy, as shown in equation (2). At the oxide/solution interface, an oxygen vacancy can be filled by an oxygen atom supplied by a water molecule or an OH ion present in solution from the self-dissociation of water through deprotonation, as shown in equation (4) in Figure 11. If indeed oxygen is supplied from water molecules, the water needs to be able to dissociate at the oxide surface or at an oxygen vacancy at the oxide surface. This is, however, not considered in the PDM, but there might be some implications if the dissociation of water determines the rate of incorporation of oxygen into the oxide lattice. This rate constant could then depend on the thickness of the oxide, as was shown for oxygen dissociation in gas-phase oxidation, which describes the mechanism for a real steady-state self-limiting thickness [43]. However, in a solution, there are other ways to achieve a self-limiting thickness for a thin oxide film [56]. The metal oxide can dissolve at the oxide/solution interface by ejection of a cation from the oxide lattice into the solution, which can involve further oxidation of the metal cation or not, as shown in equation (3). The metal oxide can also be dissolved by a chemical reaction with protons present in the solution, as seen in equation (5). This can also include charge transfer or not. These are the reactions needed to describe the oxide growth and its steady-state thickness.

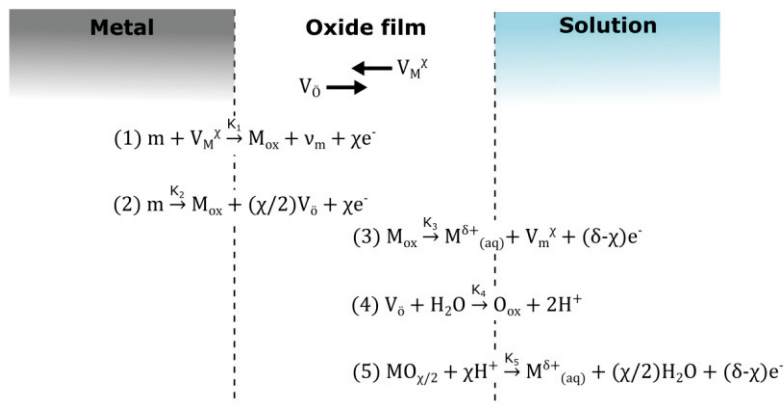


Figure 11: Chemical reactions system as part of the PDM. V_δ : oxygen anion vacancy two times positively charged, V_M^X : metal cation vacancy with charge X , m : metal atom in the metal, M_{ox} : metal cation in the oxide lattice, v_m : vacancy of a metal atom in the metal, $M^{\delta+}(aq)$: metal cation in solution with charge δ , O_{ox} : oxygen anion in the oxide lattice.

In the electric field generated across the thin oxide film, cations and anions can migrate across the oxide film with oxygen vacancies moving from the metal/oxide interface towards the oxide/solution interface and cations in the opposite direction during anodic polarization. This electric field is responsible for the driving force of oxidation, which requires not only the change of oxidation state of the metal atoms but also the movement of cation and oxygen vacancies, which essentially is the movement of cations and anions in the opposite direction. Imagine now that we have a very thin oxide film on the metal surface, and we apply a large anodic potential to our electrode. This will result in a large potential drop across the oxide, which in turn generates a large electric field. This will trigger the movement of cation and oxygen vacancies, and the oxide film will start to grow. As the oxide grows thicker under a constant applied electrochemical potential, the electric field strength in the oxide layer will decrease, which in turn slows down the growth rate of the oxide layer (again, similar to the Cabrera Mott model). As the oxide grows, the electric field strength will continue to decrease but never reach zero. So, the oxide should always keep growing thicker. But this is not what is observed experimentally. To make the model agree with reality, we consider the always present, but slow dissolution of the oxide layer. These reactions do not have to involve any transfer of electrons (if $\delta=X$ in equations (3) and (5) in Figure 11) and are hence of a pure chemical nature. This means that the rate of the dissolution reactions is independent of the electrochemical potential and the resulting electric field strength. This is different from the reaction involved with oxide growth, which is electrochemical and hence has a rate that depends on the electrochemical potential. These two types of reactions, oxide growth and dissolution, will at some point reach a balance, a steady state, where the rate of oxide growth is equal to the rate of dissolution. This

steady-state thickness is both potential and pH-dependent. As the potential is increased, the steady-state oxide thickness will increase, and as the pH decreases, so will the steady-state oxide thickness, as illustrated in Figure 13 a). This also means that in the passive state of a metal, the electrochemical current is never zero. There will always be a finite passive current due to the electron transfer associated with the oxide growth, which is needed to keep up with the slow dissolution.

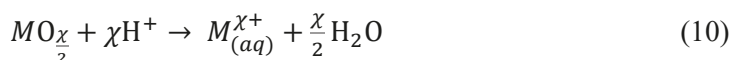
Passive film breakdown and corrosion reactions

In the previous chapter, the PDM was introduced for the passive state, where the steady-state oxide thickness under electrochemical polarization was discussed. Let us now have a look at how the oxide film can transition from a stable state into an unstable state where passivity breaks down.

First, let us consider the effect of pH, and especially that of low pH. If we assume that no change of oxidation state occurs during the dissolution of the oxide ($\delta=X$ in equation (5) in Figure 11), the rate of the dissolution is only dependent on the concentration of protons, $[H^+]$, in solution, which is the definition of the pH as shown in Equation (9).

$$pH = -\log ([H^+]) \quad (9)$$

The dissolution reaction can then be expressed as shown in Equation (10)



There can then be a point where the rate of dissolution is larger than the rate of oxide growth for a given pH. This means that no stable oxide film can form on the surface, and the material will dissolve rapidly. The prediction of the thermodynamically stable species as a function of pH and electrochemical potential is described in the Pourbaix diagram developed by Marcel Pourbaix [54]. The Pourbaix diagram of Cr is shown in Figure 12.

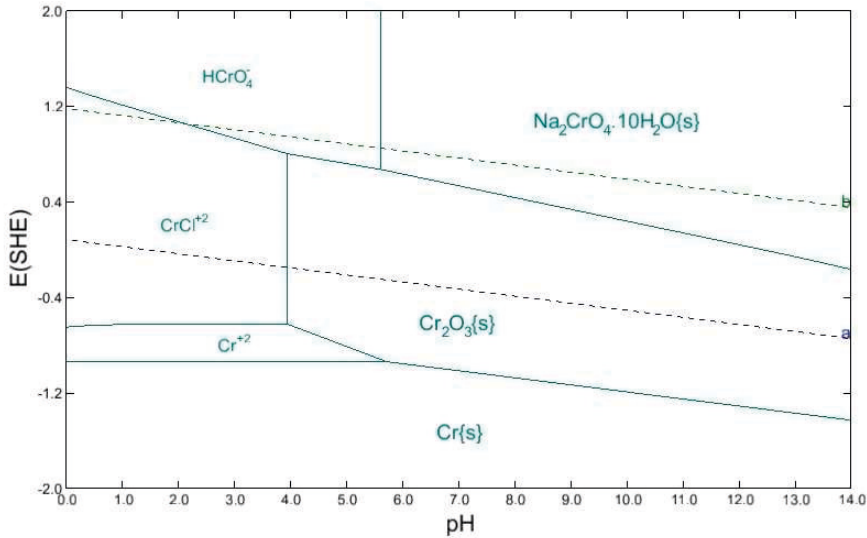


Figure 12: Pourbaix diagram of Cr in 1 M NaCl at 25 °C. The dotted lines indicate the stability window of water. Below, hydrogen evolution occurs, and above oxygen evolution.

As can be seen, there is a large potential-pH window where Cr_2O_3 is the most thermodynamically favored species. Under these potential and pH conditions, an alloy rich in Cr will be in the passive state. But according to the Pourbaix diagram, alloys relying on a Cr-rich oxide, such as stainless steel and many Ni alloys, would not be stable in solutions with a pH lower than ~ 5 where Cr_2O_3 is no longer the most thermodynamically stable species (this does not necessarily mean that solid Cr_2O_3 is thermodynamically unstable which is very important to point out), but instead, the aqueous Cr^{3+} ion is the most stable. In practice, however, stainless steel and other Cr-rich alloys can display stable passive films in very acidic solutions outside the thermodynamically predicted stability window of the Pourbaix diagram. This is due to the kinetics of oxide formation and dissolution. If the oxide film becomes thinner due to chemical dissolution, the electric field strength would increase dramatically and drive the reactions for oxide formation. Therefore, a kinetically stable passive film can exist outside the thermodynamically stable region of the Pourbaix diagram, as shown in Figure 13 b). Since passivity is a steady state phenomenon, governed by kinetics, and not an equilibrium state, the Pourbaix diagram is not always the best prediction for passivity and passivity breakdown. But as stated before, for a given potential, there will be a pH value that is low enough to trigger a chemical passivity breakdown of the oxide film. It is just often much lower in practice than predicted by the Pourbaix diagram. [57]

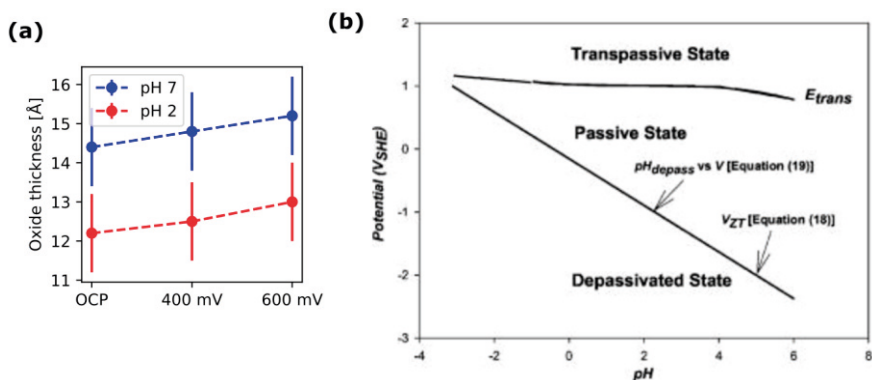


Figure 13: a) Oxide thickness for Ni alloy 59 as a function of potential for neutral and acidic pH. Note that the oxide film grows thicker as the potential is increased and that the oxide is thinner in acidic pH. b) Kinetic stability diagram for a Ni-Cr-Mo alloy as a function of potential and pH adapted from Ref [57]. Note the large difference to the stability window predicted by the Pourbaix diagram based on thermodynamic equilibrium.

Now, let us look into how the electrochemical potential might affect the stability of the oxide film. In the previous chapter, we saw that the driving force for oxidation, which is the electric field across the oxide layer, is potential dependent, and the higher the anodic polarization, the thicker the oxide film would grow for a given pH value. But is there an upper potential limit for this? Well, here we can have another look at the Pourbaix diagram. Above, we discussed the effect of pH, which in principle means moving along the horizontal axis in the Pourbaix diagram, where we moved from stable and solid Cr_2O_3 at pH above 5 to the aqueous Cr^{3+} ion below pH 5. This did not include any change in the oxidation state of the Cr. But if we move along the potential axis of the Pourbaix diagram, we will move into a region where Cr^{3+} (in the solid oxide or in solution) is oxidized to Cr^{6+} . As seen from the Pourbaix diagram, the most thermodynamically stable species of Cr^{6+} are dissolved in the solution at low pH. This means that if we increase the potential, we will move into a regime where the stable Cr_2O_3 will change oxidation state and become soluble. This is known as transpassive breakdown and is usually associated with a drastic increase in the electrochemical current compared to in the passive state. However, the current might not be the best measure of true transpassive breakdown since OER can also considerably contribute to the current at high anodic potentials for catalytically active alloys [58, 59] and can also trigger passivity breakdown. It is not only the pH and electrochemical potential that governs the corrosion rate or can trigger passivity breakdown.

Empirically, chloride ions are known to initiate and facilitate corrosion. It is present in many environments, such as seawater, salt on roads, in food, and in the chemical

industry. This makes NaCl one of the most studied and widely used electrolytes for corrosion research. Chloride ions can adsorb or bind to oxygen vacancies at the oxide/electrolyte interface and can make complexes with the metal cations, which facilitates their dissolution from the oxide surface [54]. The dissolution of the metal cation is the rate-determining step for the dissolution in the passive state and, therefore, determines the passive current density [60]. Chloride also plays a significant role in localized corrosion (pitting corrosion), which was not observed or studied in this thesis, but it deserves recognition since it is a widely observed corrosion mechanism for many lower-grade alloys, resulting in severe damage to the material [61-63].

Electrochemical techniques

Electrochemical techniques have been used extensively and have improved our understanding of electrochemical phenomena that take place on electrode surfaces. However, these techniques do not provide any direct chemical or structural information from the surface, which leads to the need for speculation. But combined with other techniques, they serve as indispensable tools to access the electrochemical behavior, which can then be correlated with spectroscopic or structural techniques to get a complete understanding of how surface chemistry and structure are connected to the material behavior.

Polarization curve

One of the most fundamental electrochemical measurements is to measure the electrochemical current as a function of potential. This can be known as a polarization curve or a cyclic voltammogram (CV) if the potential is cycled back and forth several times. We have already encountered a polarization curve in Figure 9, where we saw how the current varies as the potential is linearly increased for a sample of Ni alloy 59 in a 1 M NaCl solution at pH 2. During a polarization curve, the potential is linearly increased from a starting point to a maximum potential at a given sweep rate. The potential sweep rate influences the measured current, and typically, during corrosion experiments, a slow sweep rate is used (1-0.1 mV/s). This allows the system to stay close to thermodynamic equilibrium. This also minimizes the contribution from any non-faradaic processes to the measured current, such as the charging of the electrochemical double layer. At very high sweep rates, the apparent overpotential for a reaction will increase since the system has not been given enough time for the reaction to take place.

Electrochemical impedance spectroscopy

To study the resistive and capacitive properties of the solid/electrolyte interface, and in particular the passive film at the surface, frequency modulation can be used. This is done with Electrochemical Impedance Spectroscopy (EIS), in which a sinusoidal wave with a given amplitude is superimposed on the applied potential. The measured current will then also be sinusoidal with a given amplitude and phase shift relative to the applied potential. Here, we also need to introduce or remind us about the impedance or the complex number representation of electrical resistance. A normal resistor has no imaginary contribution, while a capacitor has a purely imaginary contribution and is frequency dependent, as shown in Equation (11), where ω is the frequency, and C is the capacitance. This furthermore introduces a phase shift of 90 degrees to the measured current.

$$Z_C = 1/j\omega C \quad (11)$$

This implies that at infinitely high frequencies, the impedance of a capacitor is zero, while the impedance is infinitely large at a frequency of zero, which, in principle, is direct current. These different responses of electrical circuit elements can be exploited and explored using frequency-based spectroscopy, which is the premise for EIS. The most common (and most simple) circuit used to model the passive film on metals is shown in Figure 14, together with the corresponding impedance spectra. At high frequencies, the resistance of the circuit is defined only by the solution resistance R_s , and at low frequencies, it is dominated by the resistance for charge transfer (this is not really the same as the resistance of the barrier layer since one also needs to consider if there are other reaction that are thermodynamically possible such as OER and HER at sufficient anodic and cathodic potentials). At intermediate frequencies, the impedance is governed by both the capacitor and the charge transfer resistance. EIS data can be represented as a Nyquist plot where each data point measured at a separate frequency is plotted in the complex plane of the impedance (imaginary part on the y-axis and real part on the x-axis). One can also illustrate the data using the Bode plot where the magnitude of the impedance (in logarithmic scale) and the phase shift of the measured current are plotted against the frequency of the AC potential component in logarithmic scale.

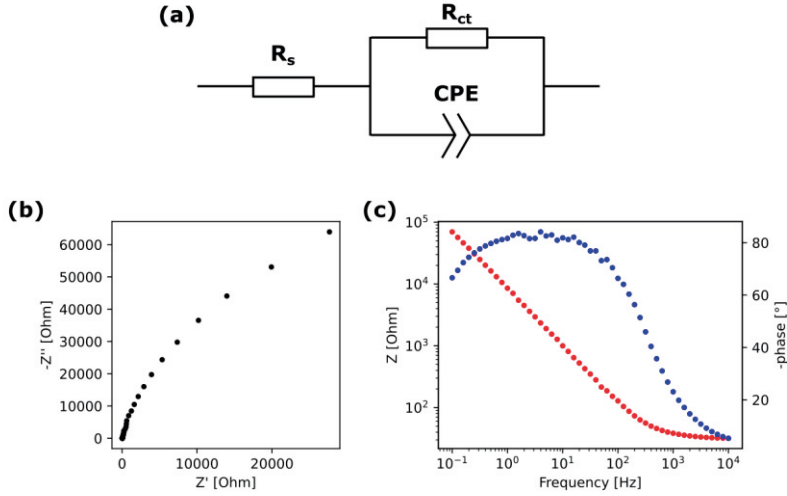


Figure 14: a) Equivalent circuit to model EIS data of an alloy in the passive state. b) Nyquist representation of EIS data. c) Bode representation of EIS data.

Mott-Schottky analysis

One can take the frequency-modulated analysis one step further to study the semiconducting properties of the thin oxide films on the metal surface through the Mott-Schottky analysis (same Sir Nevil Mott, who developed the theory of oxidation of metals introduced above). As discussed in the chapter about passive film growth, the PDM relies on cation and anion vacancies as modes of transport of charged species across the oxide film in the presence of the electric field. With Mott-Schottky analysis, the concentration of these “dopants” or defects can be calculated from the slope of the inverse square of the capacitance plotted against the potential, as shown in Equation (12) [64],

$$C^{-2} = -\left(\frac{2}{q\epsilon\epsilon_0N_A}\right)(E - E_{fb}) \quad (12)$$

where C is the capacitance, q is the elementary charge, ϵ_0 is the vacuum permittivity, ϵ is the dielectric constant of the oxide, E is the applied potential, and E_{fb} is the so-called flat band potential.

Electrochemical cell for synchrotron experiments

Most of our *in situ* synchrotron experiments have been performed using our own dedicated electrochemical flow cell [65-68], as shown in Figure 15. The cell is made of polyetheretherketone (PEEK) and has a thin window (200 μm) where the X-rays can pass through. The sample, which has a top-hat shape and acts as the working electrode in the cell, is mounted from below. From the top, a glass window is mounted, which gives optical access for simultaneous 2D-SOR measurements. From the sides, the inlet and outlet for the electrolyte are mounted, which is circulated using a peristaltic pump from a glass bottle reservoir. From the sides, the reference and counter electrode are also mounted. This cell is dedicated to hard X-ray studies where the 8 mm of water in the beam path does not significantly attenuate the signal. We have found that the practical limit lies somewhere around 10 keV. The rotational symmetry of the cell allows us to perform measurements where rotation of the sample is necessary (this is essential for surface X-ray diffraction, which is an excellent technique used to study surface structures in electrochemistry [68-70]) and when access from the side of the cell is of interest as was done with XRF.

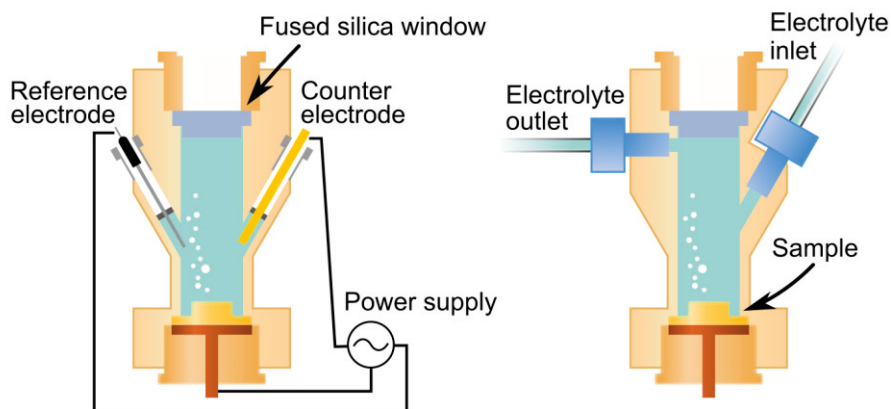


Figure 15: Electrochemical cell used for *in situ* hard X-ray and 2D-SOR studies seen from two different projections. Reproduced from Ref [66].

4. X-ray based techniques

Introduction to X-rays

X-rays were discovered in 1895 by Wilhelm Röntgen [71], who later received the first Nobel prize in physics for his discovery in 1901. At the time of the discovery, it was an unknown form of radiation, but it is now well established that it is electromagnetic radiation, just like the visible light that our eyes can detect, but with a much smaller wavelength and much higher energy, as shown in Figure 16. Today, X-rays are used in medical applications both as diagnostic tools and in treatments. X-rays are used at airports and customs to image the interior of luggage and even entire trucks. X-rays are also used extensively in science and technology to determine the structure and chemistry of matter. The specific energy range of X-rays makes them an excellent probe for studying matter. X-rays have the right energy range to interact with and excite core-level electrons in atoms, which is exploited to probe the chemical environment of the atoms within a sample. The highly energetic X-rays are also penetrative, making it possible to probe hidden structures such as the bones in a broken arm at the hospital. The wavelength of X-rays is also of the same length scale as the distance between atoms. When X-rays interact with a crystalline sample, interference effects can be utilized to determine the structure of the crystal.

THE ELECTROMAGNETIC SPECTRUM

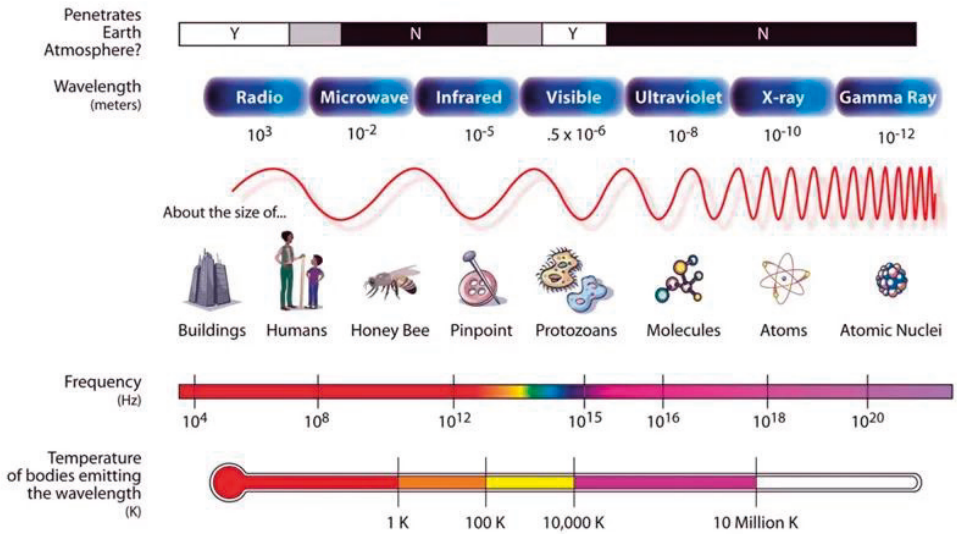


Figure 16: The electromagnetic spectrum spanning from radio waves to gamma rays and contains the spectral ranges of visible light and X-rays that were used in this thesis. Image credit: NASA.

Electromagnetic radiation, such as X-rays and visible light, is characterized by the wavelength and frequency of the electromagnetic waves. The wavelength, λ , and frequency, ν , are coupled by the speed of light and are energy-dependent, as shown in Equation (13) below, where h is Planck's constant, and c is the speed of light. [72]

$$E = \frac{hc}{\lambda} = h\nu \quad (13)$$

Electromagnetic radiation can be described using a vector formalism, which will be used later in the coming chapter. The light is then characterized by its wave vector, \mathbf{K} , which has a direction and a magnitude, as shown in Equation (14) below. [72]

$$|\mathbf{K}| = \frac{2\pi}{\lambda} \quad (14)$$

For X-rays, a complex refractive index is used to describe the interaction with matter, as shown in Equation (15) below.

$$n = 1 - \delta + i\beta \quad (15)$$

Contrary to visible light, in the X-ray regime, materials have a refractive index, n , lower than unity (since the refractive index is defined as the ratio of the speed of light in vacuum divided by the speed of light in the medium a refractive index less than one would mean that X-rays travel faster than the speed of light in matter, which would defy a fundamental law of physics. This is, however, not the case since it is the phase velocity that is faster than the speed of light, not the speed at which energy or information travels for X-rays in matter). Therefore, total external reflection of X-rays can occur at the interface between a less dense material and a dense material, such as a solid surface in air or liquid. The angle at which this takes place is known as the critical angle for total external reflection [73]. This is used extensively in X-ray optics to focus and redirect X-ray beams and gain surface sensitivity during measurements, as will be shown later. The imaginary part of the refractive index for X-rays relates to the mass attenuation coefficient related to the absorption of X-rays in the medium.

X-rays can interact with matter through different mechanisms. An incoming X-ray can be absorbed by an atom, or it can be scattered (here we ignore inelastic scattering and pair production). Absorption by an atom can lead to the ejection of a photoelectron, which is the basis for XPS. The probability of absorption as a function of energy can be measured as in XANES, and when the excited atom relaxes, a fluorescence photon is emitted, which is measured in XRF. All these phenomena related to absorption depend on the electronic structure of the atom and are hence connected to the chemistry of matter, which is probed by the mentioned spectroscopic techniques. Scattering of the X-rays can lead to constructive interference at various length scales depending on the arrangement of the atoms in space. XRD and XRR rely on the scattering of X-rays and are, therefore structure-sensitive methods.

Synchrotron radiation and beamlines

Traditionally, X-rays were generated using X-ray tubes where electrons are accelerated towards a metal target [74]. When the electrons are decelerated in the metal target by deflection due to the interaction with charged particles, namely electrons and nuclei, a broadband spectrum of X-rays is emitted called bremsstrahlung. The atoms in the metal target can also be excited and re-emit the absorbed energy as electromagnetic radiation in the X-ray range, resulting in sharp peaks in the X-ray spectrum. These sources are still used in medical applications and lab-based scientific instruments.

A new type of X-ray source emerged in the 1960s by accelerating electrons radially in a magnetic field [72]. This is known as synchrotron radiation [75]. Modern synchrotrons are particle accelerators where relativistic electrons are traveling near

the speed of light in vacuum. The path of the electrons is in the shape of a polygon with straight segments and many bends, as shown in Figure 17 a). The electrons are directed in the curved path by bending magnets. Synchrotron radiation is emitted with a broad divergence when the electrons bend in the magnetic field [74]. More sophisticated ways have been developed to generate synchrotron radiation with a smaller divergence, where the electrons travel through a periodic array of magnets oriented in opposing polarity. This forces the electron to make many sharp turns as the pole of the magnetic field switches, and the electron “wiggles” through the magnet array, emitting synchrotron radiation in the forward direction with a low divergence [74]. There are two main types of insertion devices, namely wigglers and undulators, both of which are based on these arrays of opposing magnetic poles, as shown in Figure 17 b) and c). In an undulator, the magnetic field is smaller, and therefore, the deviation of the electrons from their initial trajectory is small, resulting in smaller and less divergent X-ray beams. The undulator is designed such that the electromagnetic radiation produced at each magnetic pole interferes constructively such that a narrow energy spectrum is achieved with a primary energy as well as higher harmonics. A wiggler uses larger magnetic fields such that the electrons “wobble” with a larger amplitude, which results in a broad energy spectrum and a larger spot size [76, 77]. The relativistic nature of the electrons in the storage ring results in synchrotron radiation being produced in the forward direction with a low divergence in the insertion devices [74]. Compared to X-ray tubes, synchrotron sources can generate monochromatic and broadband radiation with tunable energy in a broad energy range from UV light to hard X-rays with an energy of more than 100 keV. Synchrotrons also generate a photon flux many orders of magnitude higher than lab sources [72], and the X-rays can be focused down to a spot of a few tens of nanometers [73]. All these properties of synchrotron radiation make it a very suitable and versatile tool for studying the atomic structure and chemistry of materials under operating conditions. The research in this thesis was carried out at the first 4th generation synchrotron facility in the world: MAX IV in Lund, Sweden [78-80], as well as at PETRA III, DESY in Hamburg, Germany [81, 82].

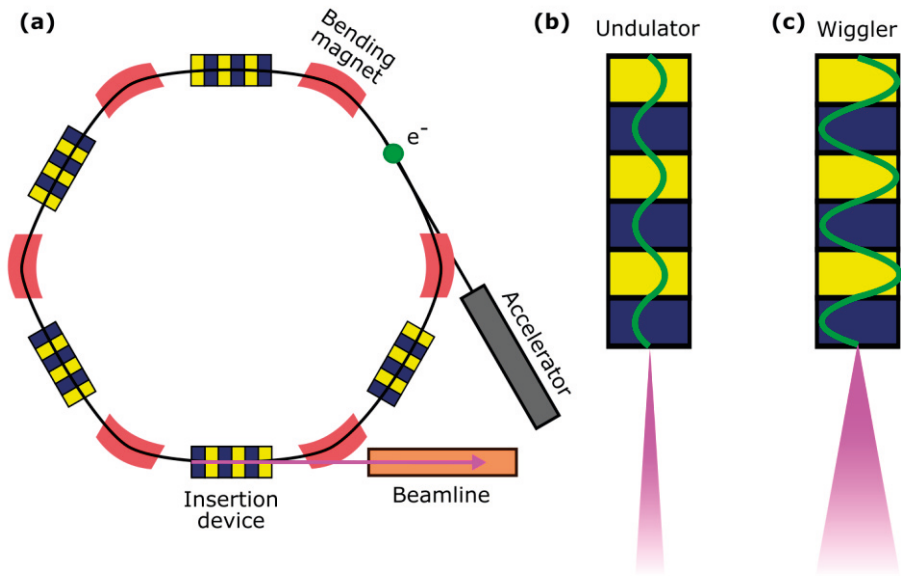


Figure 17: a) The polygon-shaped electron storage ring of a synchrotron with bending magnets and insertion devices. b) Schematic illustration of an undulator insertion device. c) Schematic illustration of a wiggler insertion device.

Once the synchrotron radiation is generated in the dedicated insertion device, it enters the so-called beamline, where the properties of the beam are tuned before it reaches the end station, where the experiments are performed. Typical elements of a beamline are shown schematically in Figure 18, which depicts the HIPPIE beamline at MAX IV. The first element is usually a mirror to take a significant amount of the heat load of the intense X-ray beam as well as to collimate the beam. Afterward comes the monochromator, which is a crucial part of every beamline. The monochromator is used to select the energy of the X-ray beam and make it monochromatic. This is done by using either two large single crystals as in a Double Crystal Monochromator (DCM) [83, 84] or two gratings as in the Plane Grating Monochromator (PGM) [85, 86]. From the crystal or grating, the X-rays diffract, and the initially polychromatic beam is spectrally dispersed since the diffraction angle is energy dependent, as will be seen in Bragg's law. From Bragg's law, we can also understand why crystals work for hard X-ray beamlines but not soft X-ray beamlines (100-2000 eV). For a Si(111) crystal, which is commonly used in DCM, a primary diffraction angle of 90 degrees is reached at 3.7 keV. Therefore, a grating with a larger lattice spacing than a crystal is needed to diffract the soft X-rays at a lower angle for a monochromator to function. After the monochromator, more focusing elements can be added. These can be curved mirrors that make use of total external reflection [87, 88] or Compound Refractive Lenses [89], which work

similarly to optical lenses used in optics, only that the dense material of an optical lens has to be replaced with a less dense material in the X-ray regime since the refractive index of dense materials is lower. Since CRLs require the transmission through matter for focusing, these optical elements work only for hard X-rays where attenuation is less of an issue. After all these elements that have collimated, monochromatized, and focused the X-ray beam, the X-rays can then go to the end station where the experiments are performed.

The research in this thesis is based on several different synchrotron X-ray techniques, and several beamlines have been used throughout my work and will be listed and briefly introduced below.

- FlexPES, at MAX IV, is a soft X-ray undulator beamline with a photon energy range of 40 to 1500 eV dedicated to XPS and Near Edge X-ray Absorption Fine Structure (NEXAFS). We have used the Surface and Materials Science end-station dedicated to XPS of solid samples in UHV [90]. Papers I, II, and III are based on data from FlexPES.
- HIPPIE at MAX IV is a soft X-ray undulator beamline with a photon energy range of 250 to 2200 eV dedicated to AP-XPS. We have used the electrochemical AP-XPS end station with a dedicated dip and pull setup [91], as shown in Figure 19. Papers IV and VI are based on data from HIPPIE.
- P21.2, the “Swedish Materials Science” beamline at PETRA III, is a high-energy undulator beamline with a photon energy range of 40 to 150 keV dedicated to diffraction, small angle scattering, and imaging. At P21.2, we have used our own electrochemical flow cell described in Figure 15 and performed *in situ* XRD, XRR, and XRF combined with electrochemical control, as shown in Figure 20. Papers I, and IV are based on data from P21.2.
- P64, the “advanced XAFS” beamline at PETRA III, is a hard X-ray undulator beamline with a photon energy range of 40 to 150 keV dedicated to high time resolution XAFS and XAFS on diluted systems [92]. At P64, we used our own electrochemical flow cell described in Figure 15 and measured XAFS from dissolved metal ions in solution and the chemistry at the surface after corrosion in grazing incidence with the setup shown in Figure 21. Papers IV and IX are based on data from P64.

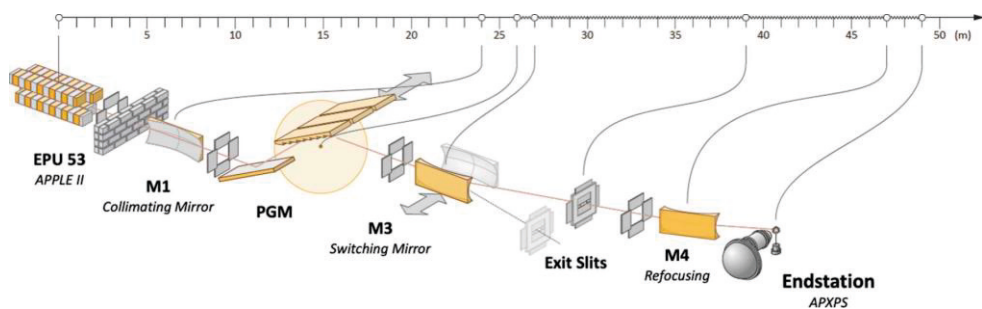


Figure 18: Illustration of the main elements in a synchrotron beamline. This particular illustration is for the HIPPIE beamline at MAX IV, taken from Ref [91].

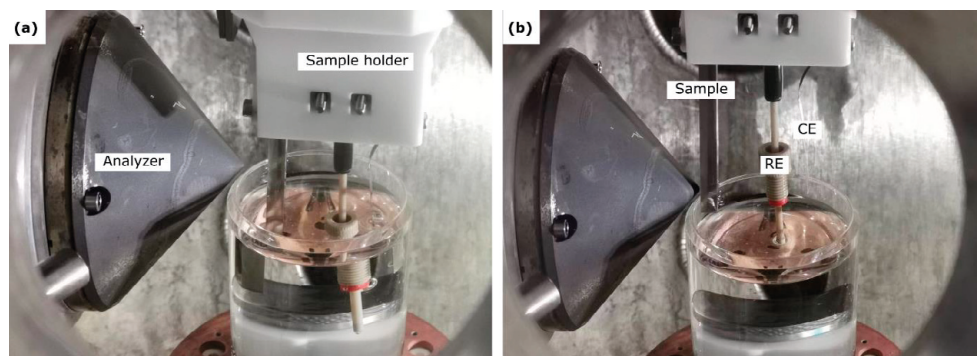


Figure 19: Experimental setup inside the chamber at the HIPPIE beamline, MAX IV. a) The sample is in the dipping position for electrochemical exposure. b) The sample is in the measuring position.

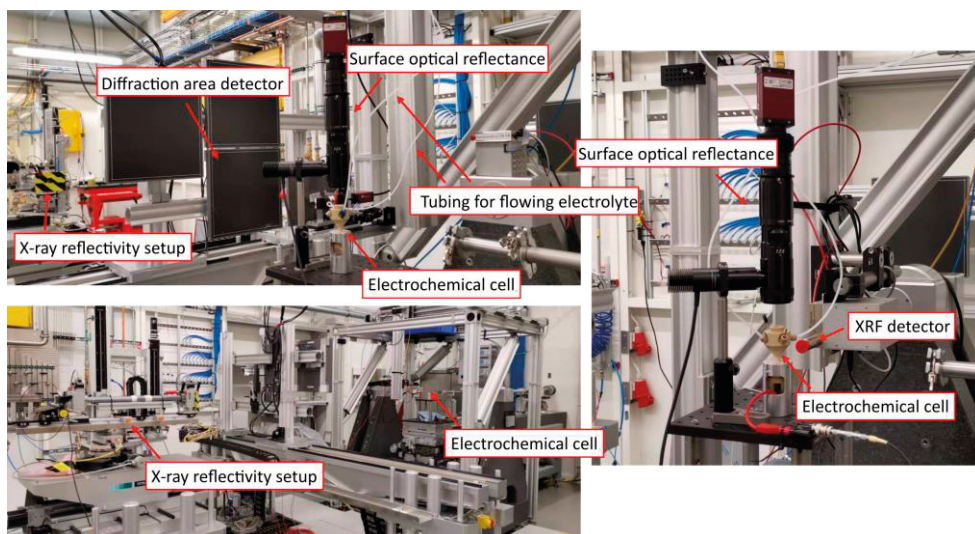


Figure 20: Experimental setup at the P21.2 Swedish Material Science Beamline, PETRA III, DESY. This setup was used to perform simultaneous XRD, XRR, and XRF measurements.

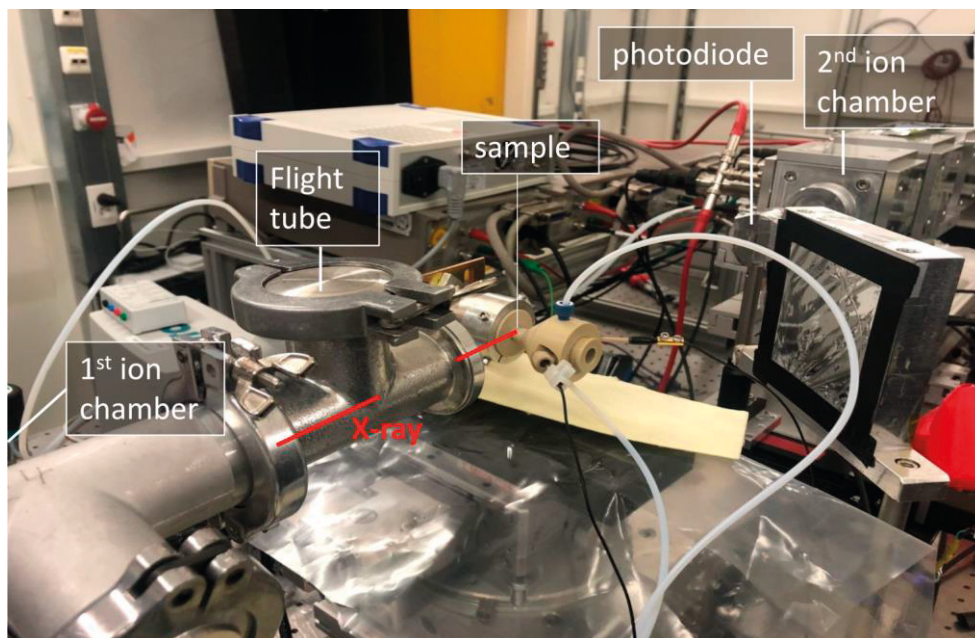


Figure 21: Experimental setup at P64, PETRA III, DESY.

X-ray photoelectron spectroscopy

XPS was developed by Kai Siegbahn, who was awarded the Nobel Prize in Physics in 1981 "for his contribution to the development of high-resolution electron spectroscopy" [93]. XPS is now a cornerstone of experimental material science and surface science and is a widely available tool in laboratories around the world [94, 95].

The basis of XPS is the photoemission process (or photoelectric effect), described first by Einstein in 1905 [96] for which he received the Nobel prize in 1921, where an incoming photon is absorbed and excites a core-level electron of an atom that is emitted into the continuum, as shown in Figure 22 a). This results in the creation of a core hole in the excited atom and a photoelectron. The kinetic energy, E_k , of the emitted photoelectron, depends on the photon energy, $h\nu$, the binding energy of the core-level electron, E_B , and the work function of the surface, Φ , which is the energy needed to remove an electron from a solid surface into vacuum, as shown in Equation (16).

$$E_k = h\nu - E_B - \Phi \quad (16)$$

Once the photoelectron has been generated, we also need to detect it. Spectroscopic techniques based on electrons have several advantages since electrons are easily focused, their energy is easily tuned by electric fields, they are relatively easy to count, and with an electric field, they can be spectrally separated in energy. This makes it relatively straightforward to analyze the intensity of the emitted photoelectrons as a function of their kinetic energy, which is performed using a hemispherical electron energy analyzer [97]. The kinetic energy scale can then be transferred into the binding energy scale using Equation (16), and plotted as shown in Figure 22 b). The zero on the binding energy scale can be calibrated by measuring the Fermi level or a well-defined core level (for that, Au 4f is often used). [98]

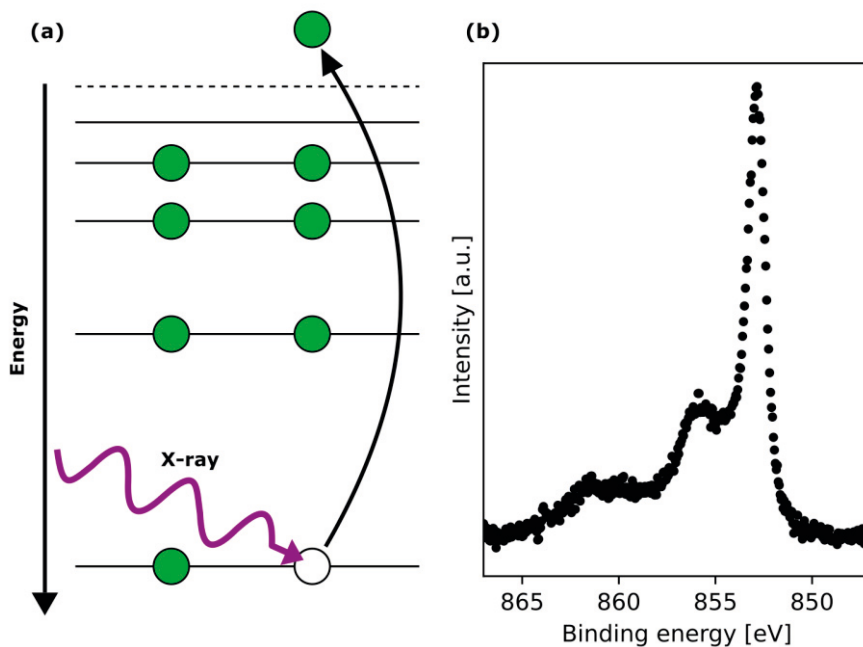


Figure 22: a) Simple schematic of the photoemission process where an electron is excited from a core level into the continuum upon absorption of a photon. b) XPS spectra of the Ni $2p_{3/2}$ core level from the Ni-Cr-Mo alloy.

There is one more property of electrons that must be added to the list above, and that is the strong interaction with matter. This means that the low-energy photoelectrons cannot travel far in condensed matter, and as a result, only the photoelectrons that are generated near the sample surface can escape and be detected. The mean-free path, λ , of electrons as a function of kinetic energy in solids shown in Figure 23 is known as the universal curve. The mean free path is defined as the distance where the intensity has decayed to $1/e$, or 63.2 %, of the original value. The information depth, d , in XPS experiments, where around 95 % of the measured signal originates, is usually defined as $d=3\lambda$. The strong interaction of electrons with matter is both a blessing and a curse. It makes XPS an inherently surface-sensitive technique (5-30 Å, as seen in Figure 23), but it also means that, without a large effort, XPS is limited to operation in UHV. In the next chapter, we will see how it is possible to move beyond that and perform XPS under near-ambient pressure.

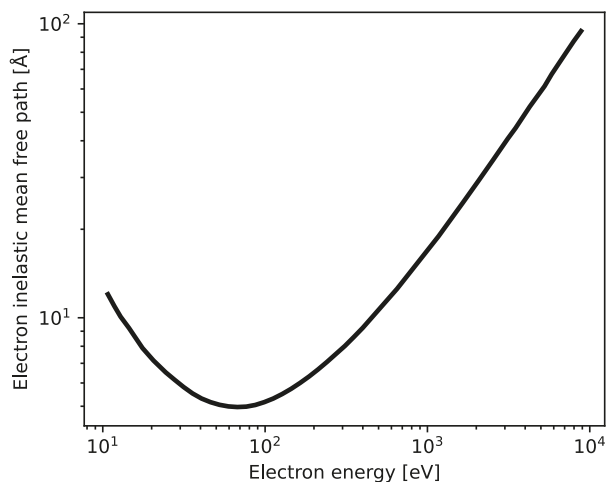


Figure 23: Electron mean free path as a function of the electron kinetic energy. Data is taken from Ref [99].

The binding energies of core levels of different elements are usually well separated in energy, such that individual photoemission lines can be studied without overlap. This allows for a clear identification of the elements present in any given sample in the probed volume. However, core-level binding energies are not only elemental specific. They also depend on the chemical environment of the specific atom, and the difference in the binding energy of a core-level electron that can arise from chemical bonding is called a chemical shift. A clear example of chemical shifts in an XPS spectrum is seen in the famous example of the ethyl trifluoroacetate molecule shown in Figure 24, where the four chemically different carbons have different chemical shifts. The origin of the chemical shift can be explained by considering the screening of the charge of the nucleus by the valence electrons. For example, fluorine is very electronegative and wants to accept electrons to achieve a full $2p^6$ electron configuration. The carbon atom binding to the three fluorine atoms in Figure 24, therefore, has much less of its $2p$ electron wavefunction localized around its nucleus. Therefore, the $C\ 1s$ core electrons are more strongly bound by the unscreened nucleus, and we can experimentally observe that as a higher binding energy for the $C\ 1s$ photoelectrons originating from the carbon atom binding to three fluorine atoms. The opposite would be the case when looking at the $F\ 1s$ photoemission spectra. The fluorine atoms that accept electrons from the carbon atom to achieve the full $2p^6$ electron configuration would have more screening of the nucleus by increased electron density in the valence $2p$ orbital. This will result in lower binding energy of the $F\ 1s$ electrons for fluorine binding to carbon compared to a free fluorine atom. [100]

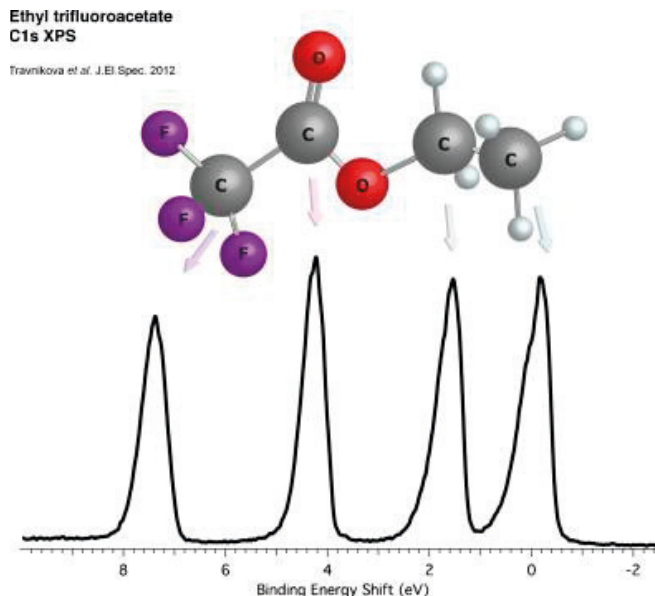


Figure 24: Chemical shift of the C 1s core level for different carbon species in the ethyl trifluoroacetate molecule taken from Ref [101].

An example of chemical shifts in the Ni 2p_{3/2}, Cr 2p_{3/2}, and Mo 3d spectra from the Ni-Cr-Mo alloy studied in this thesis is shown in Figure 25. Just like in the example of carbon binding to electronegative fluorine above, metal oxides exhibit higher binding energies than the metallic components, and the higher the oxidation state, the higher the binding energy is, as seen from the Mo 3d core level spectra, which contains several oxidation states. From the deconvolution of the spectra, the chemical states that exist in the probed volume near the surface are determined. Quantitative analysis to determine the amount of each chemical state, or the composition, in the oxide film and in the metal substrate underneath is possible based on the photoelectron intensities of the deconvoluted components. Here, the photon flux (which is energy dependent at the synchrotron beamlines), the photoelectric cross-section, the attenuation of the photoelectron signal escaping through the solid, and a theoretical layered model of the interface must be carefully considered.

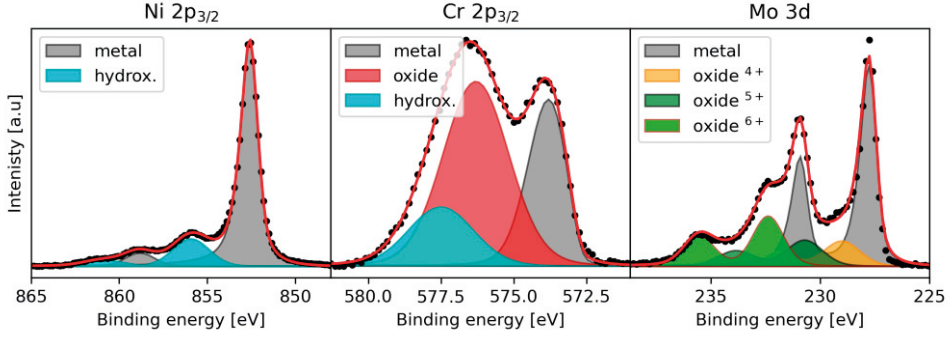


Figure 25: Example of XPS spectra of Ni 2p_{3/2}, Cr 2p_{3/2}, and Mo 3d from the native oxide formed on the Ni-Cr-Mo alloy.

The thickness of thin films can also be determined using XPS [102]. This quantitative analysis relies on the strong attenuation of the photoelectrons as they travel through the solid. For a clean metallic surface, the XPS spectra would only show a strong signal associated with the metal, as shown in Figure 26 a). If a monolayer of oxide was formed on that surface, a component would appear at higher binding energy in the spectra associated with the oxide, and the metallic component would decrease slightly in intensity due to attenuation of the photoelectrons from the metal substrate through the thin oxide layer, as shown in Figure 26 b). As the oxide film grows thicker, the oxide signal would continue to increase while the metallic signal would continue to decrease, as shown in Figure 26 a). At some point, the oxide would be so thick that all photoelectrons from the metal substrate are scattered and lost before they could escape and be detected. From this simple thought experiment, we can see that the ratio between the oxide and metal signal is related to the oxide thickness.

Considering a simple over-layer model as the oxide in Figure 26, the photoelectron intensity originating from the metal substrate, I_m , can be written as shown in Equation (17), and the photoelectron intensity originating from the oxide layer, I_{ox} , can be written as shown in Equation (18) [103-105],

$$I_m = N_m \lambda_m \sigma \cdot e^{\left(-\frac{d}{\lambda_{ox}}\right)} \quad (17)$$

$$I_{ox} = N_{ox} \lambda_{ox} \sigma \cdot \left(1 - e^{\left(-\frac{d}{\lambda_{ox}}\right)}\right) \quad (18)$$

where N_i is the number of atoms per unit volume in matrix i , λ_i is the mean free path of the photoelectrons in matrix i , σ is the photoelectric cross-section, and d is the oxide layer thickness. By dividing and rearranging the expressions for the oxide and metal signal, we arrive at the expression shown in Equation (19). [102, 106]

$$d = \lambda_{ox} \cdot \ln \left(\frac{I_{ox} N_m \lambda_m}{I_m N_{ox} \lambda_{ox}} + 1 \right) \quad (19)$$

For a more complex model with several layers consisting of different elements that are measured with different photon energies, a large system of equations can be constructed and solved to obtain the atomic concentrations in each layer as well as the thicknesses. [107, 108]

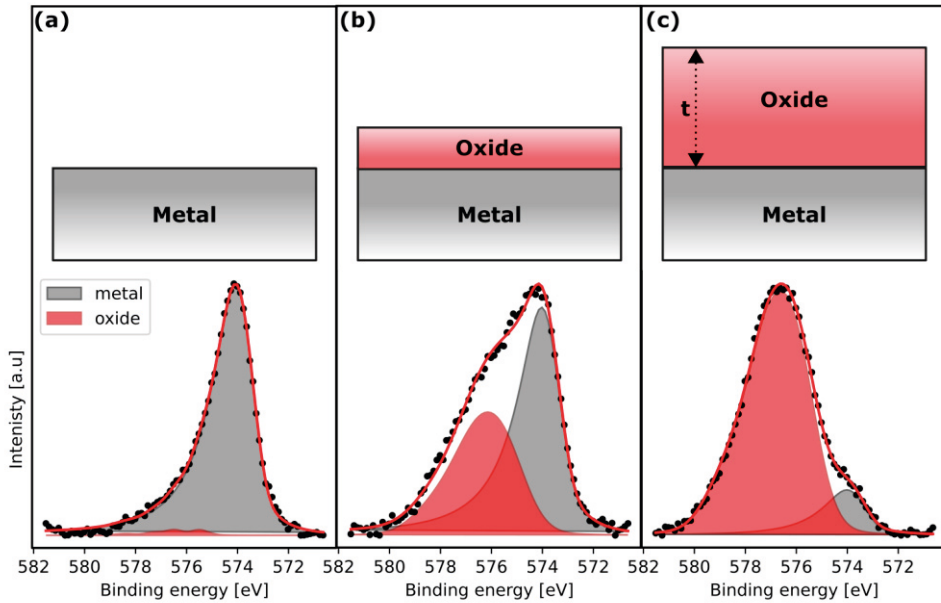


Figure 26: Oxide and metal component in the Cr 2p_{3/2} spectra during oxidation from a clean metallic surface to a thick oxide layer with corresponding schematic layered models.

Ambient pressure X-ray photoelectron spectroscopy

As stated in the previous chapter, electrons interact strongly with matter. This makes XPS an inherently surface-sensitive technique. But this also means that the sample must be analyzed in UHV. Otherwise, the photoelectrons would be scattered and lost before they could ever be detected. The above statement and the limitation to UHV were true until the 1970s when Siegbahn's group in Uppsala developed the first near ambient pressure XPS instruments dedicated to the study of liquid/vapor interfaces [109]. The instrument developed in the 1970s was limited to less than 1 mbar, but now it is possible to perform AP-XPS at pressures up to 1 bar [110-112].

The technique has also seen a significantly growing interest since the beginning of the 2000s [113].

Since the attenuation of electrons is high in a gas phase atmosphere, the path of the electrons needs to be minimized for XPS to be possible to perform at elevated pressures. This is done first by placing the cone, or nozzle, that accepts electrons into the electron analyzer system close to the sample surface. For the case of the HIPPIE beamline where our AP-XPS experiments were performed, the distance between the sample and the nozzle is 300 μm , and a pressure of 17 mbar was used. To place the analyzer close to the sample also requires a small spot size of the X-ray beam. The second important development is the introduction of differential pumping and electron focusing in the pumping system [114] between the sample compartment and the electron analyzer, which is required to operate under high vacuum, as shown in Figure 27. To separate the sample compartment containing the gases from the X-ray source (lab source or synchrotron beamline), an X-ray transparent window is used. In this way, a pressure in the high millibar regime can be maintained in the sample compartment while the X-ray source and the hemispherical analyzer are kept in vacuum. [115, 116]

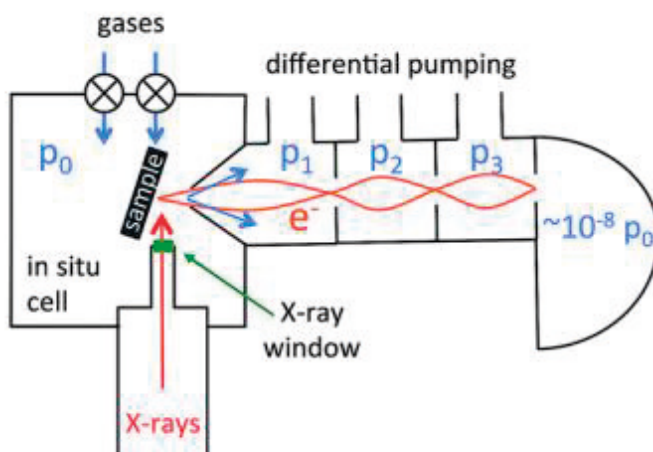


Figure 27: Schematic of an AP-XPS instrument with differential pumping and electrostatic focusing of the electrons between the sample compartment and the hemispherical electron energy analyzer. Taken from Ref [117].

In 2015, an elegant solution was presented for how AP-XPS could be used to study the solid-liquid interface under electrochemical control [118]. Since then, several papers have been published using this approach [108, 117, 119-126], and the technique is available at several beamlines [91, 118, 127] and lab based instruments [128, 129]. To combine electrochemistry and AP-XPS, a thin liquid film of electrolyte needs to be created on the sample surface. This is achieved by the so-called “dip and pull” method, as illustrated in Figure 28, where the sample can be submerged into the electrolyte and then retracted while still maintaining a thin liquid film on the surface. This thin film can be maintained with some effort, and the area probed by XPS can then be under potential control. In this thesis, the dip and pull method was used in a quasi *in situ* approach where the sample was fully retracted after exposure to the electrolyte while still maintaining a thin film of liquid water on the electrode surface, as seen in the O 1s spectra shown in Figure 27 c). This removed the cumbersome worry of maintaining a stable thin electrolyte meniscus with potential control, and all the core levels from the multi-component Ni-Cr-Mo alloy could be measured reliably, which allowed for detailed quantitative analysis to be performed. Since we only used AP-XPS to study how the passive film evolved upon anodic polarization (which is the formation of a stable oxide layer that will not disappear once the potential is terminated), the true operando conditions with full potential control were not necessary in this case. In the future, it would be interesting to study the dynamics of passive film growth with time resolution under potential control, which is something that is possible to perform with AP-XPS and the dip and pull method. Other advances in the field of combining XPS with electrochemistry deserve to be mentioned as well, where the offset droplet method [130], lab based setups [129], and closed cells with a thin electron transparent membrane [131, 132] have been shown to provide surface spectroscopic information in an electrochemical environment.

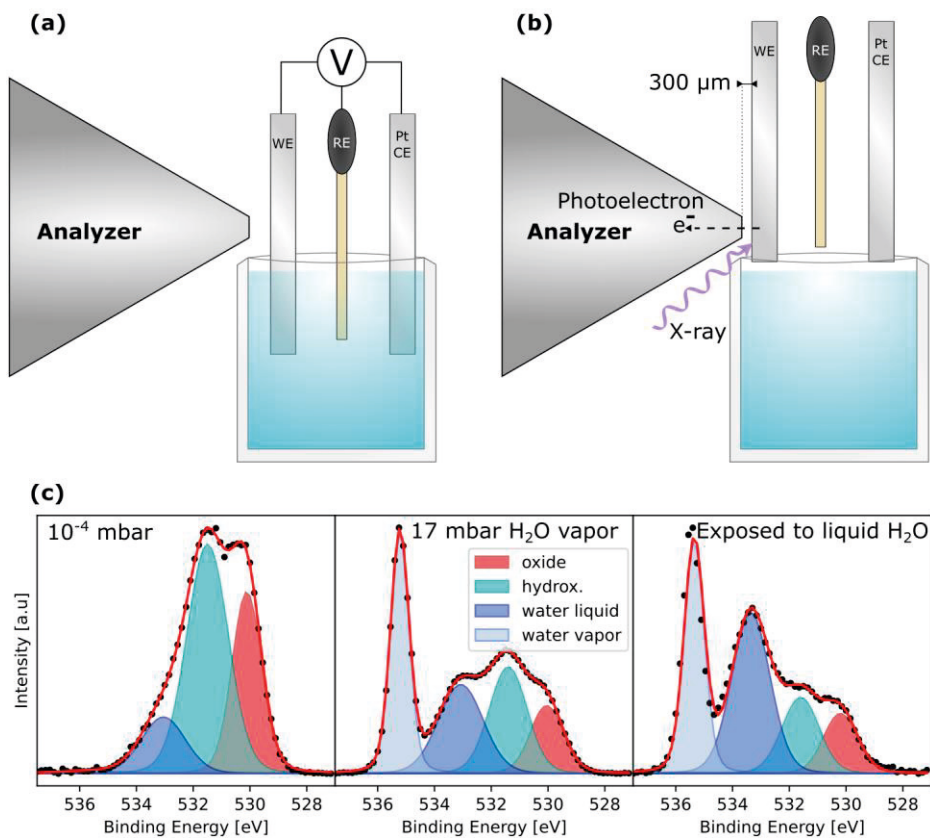


Figure 28: a)-b): Schematic of setup used to combine AP-XPS and electrochemistry through the so-called "dip and pull" approach. Dipping of the sample is seen in a) to expose it to the electrolyte, and pulling is seen in b) where the sample is retracted and AP-XPS spectra are collected. c) O 1s XPS spectra measured in 10^{-4} mbar (lowest pressure we could achieve in the electrochemical chamber at the HIPPIE beamline), 17 mbar of water vapor (vapor pressure of our electrolyte), and after exposure to the aqueous electrolyte. Note the appearance of the water vapor peak and the growth of the liquid water peak after introducing water vapor in the chamber. After exposure to the electrolyte, the liquid water peak further grew.

X-ray absorption near edge structure

Above, we discussed how surface chemistry could be explored by studying the ejected photoelectrons after photoionization. In this chapter, we will instead focus on the absorption event and how that can be used to learn about the chemistry of materials.

In X-ray Absorption Near Edge Structure (XANES), the probability of an atom absorbing a photon, which is proportional to the absorption cross section (or absorption coefficient), is measured as a function of the photon energy. This will give rise to a characteristic absorption spectrum for a given material where an increase in the absorption cross section is seen when the X-ray energy is sufficient to excite a core-level electron to an unoccupied electronic state or into the continuum (the electrons that are analyzed in an XPS experiment), as shown in Figure 29 a). This sharp increase in the absorption coefficient is known as the absorption edge. Before the edge, in the so-called pre-edge region, electronic transitions can occur from the core level to an unoccupied bound electronic state.

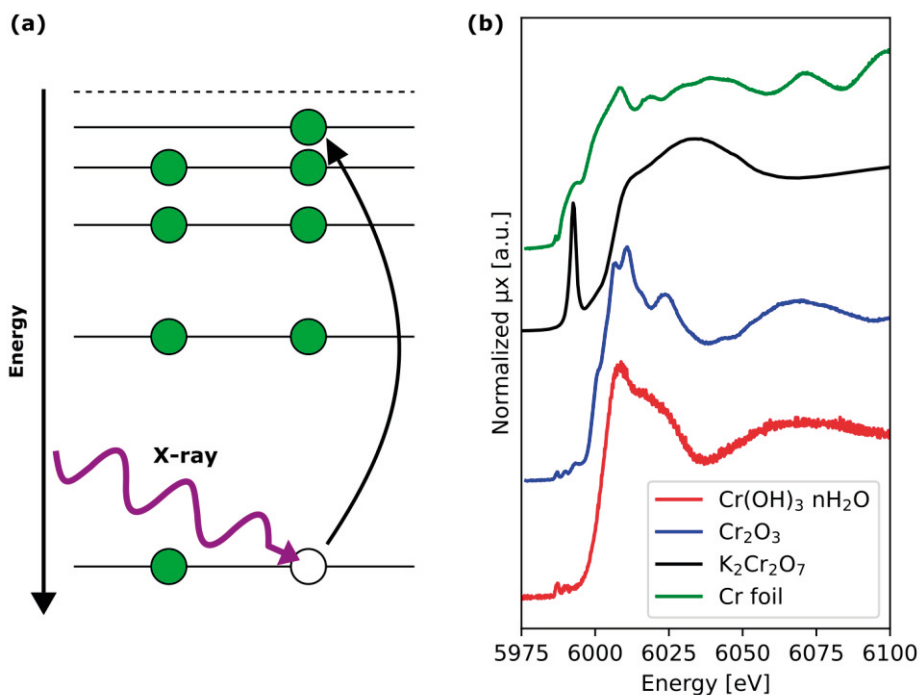


Figure 29: a) Absorption process of a core electron to an unoccupied electronic state. b) XANES spectra of different Cr species.

The features in a XANES spectrum originate from the electronic structure of the specific atom that is probed and depend heavily on the chemical environment and bonding geometry of the atom that is studied. Examples of XANES spectra of different Cr species are shown in Figure 29 b). XANES is an elemental specific technique since the core-level binding energies of different elements are well separated, especially in the hard X-ray regime. The interpretation and modeling of XANES spectra is complex, and it is therefore often used as a fingerprinting technique, which is also how the technique was used in this thesis. This requires a comparison of XANES spectra from the sample of interest with spectra from reference material, which are also measured at the beamline. These references are often measured from powdered material pressed into pellets, metallic foils, or ions in solution. During a XANES experiment, the absorption of the X-rays in the material is measured. This is most commonly performed in a transmission geometry by measuring the attenuation of the X-ray beam derived from the intensity before and after the sample. It can also be measured in fluorescence mode, where one measures the total fluorescence intensity and assumes that the absorption is directly proportional to the fluorescence detected.

Since XANES relies on the detection of photons, it is an inherently bulk sensitive technique compared to XPS. In this thesis, XANES was measured in the electrolyte to determine the chemical state of the dissolved metal ions during corrosion experiments. It was also measured in a grazing incidence geometry, as will be explained in more detail later, to study the chemical state of corrosion products deposited on the sample surface.

X-ray fluorescence

After a core hole is generated through photoelectric absorption, the atom will relax, which can be done by the filling of the core hole with an electron from a higher energy level. The difference in energy between these two electronic states is then emitted, when the atom relaxes, in the form of a photon with a characteristic energy in the X-ray regime, as shown in Figure 30 a). This is known as X-ray Fluorescence (XRF), which is a technique that provides elemental information obtained from the spectra of emitted Fluorescence X-rays, as shown in Figure 30 b). XRF was used in this thesis to quantify the amount of dissolved metal ions in the electrolyte solution *in situ* while the sample was electrochemically polarized to drive dissolution and passivity breakdown.

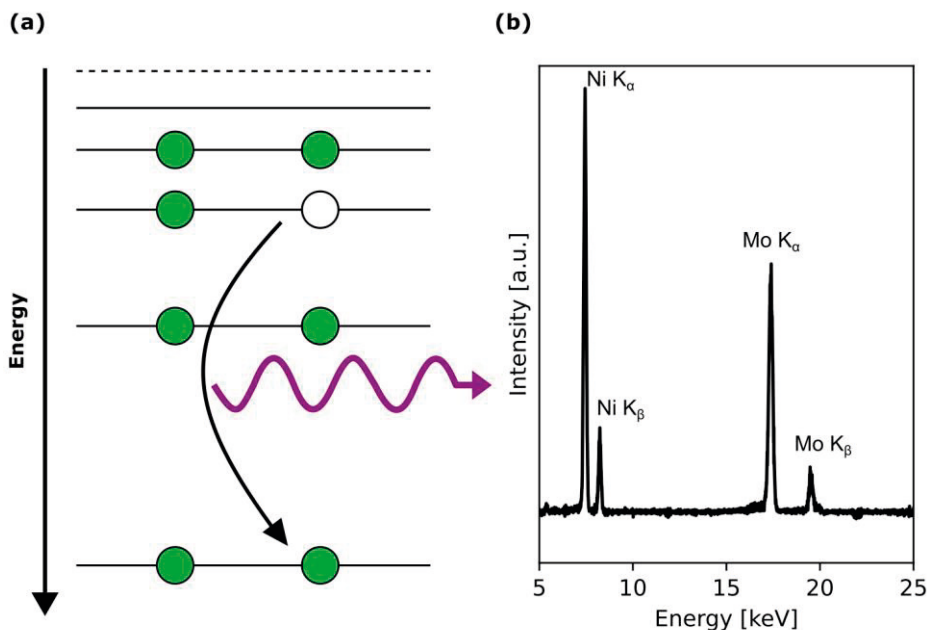


Figure 30: a) Emission of a characteristic X-ray after filling of a core hole by a higher energy level electron. b) Example of XRF spectra from dissolved Ni and Mo in the electrolyte.

X-ray diffraction

Shortly after discovering X-rays, scientists realized that the periodic structure of a crystal could act as a grating for X-rays where interference effects give rise to X-ray Diffraction (XRD). This was awarded two Nobel prizes, in 1914 to Max von Laue and in 1915 to father and son Bragg, who derived the famous Bragg's law that will be introduced shortly. But let us start at the beginning and first introduce the scattering of X-rays from a single electron as a point-scatterer.

When an electron interacts elastically with X-rays, it starts to move in the electric field of the electromagnetic wave due to its charge. The electron starts to oscillate with the same frequency as the incoming radiation and, in turn, induces a new electromagnetic field, emitting X-ray radiation spherically [72]. If we have two point scatterers that emit two spherical waves, these will overlap and interfere destructively and constructively in different directions. Considering instead scattering from a crystal containing many atoms (which in turn contains many electrons that are responsible for the interactions with X-rays as described above) in an ordered periodic structure, the scattered radiation will interfere constructively in

very specific directions, as seen in Figure 31. This is what is known as X-ray diffraction. The directions in which the scattered X-rays will interfere constructively is described by Bragg's law [133], derived by father and son Bragg, who received a Nobel prize, as mentioned earlier. The equation is derived by considering scattering from two atomic planes separated by a distance d . A primary beam of X-rays intercepts the crystal with an incidence angle θ and is scattered with an equal exit angle θ from the top and bottom atomic planes. The path difference between the X-rays scattered from the top and bottom atomic planes is equal to $2d\sin(\theta)$, and if this path difference is equal to an integer multiple of the wavelength, $n\lambda$, the two waves will interfere constructively. Now, the famous Bragg's law is derived, which is shown below in Equation (20). Notice that the angle θ is used in Bragg's law, but in a diffraction measurement, the angle 2θ is measured, which is the angle between the primary beam and the scattered beam.

$$2d\sin(\theta) = n\lambda \quad (20)$$

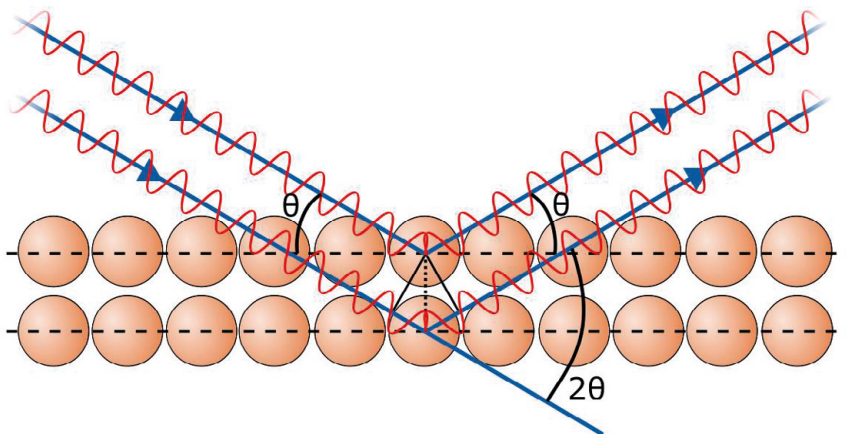


Figure 31: Scattering from a solid crystal resulting in constructive interference governed by Bragg's law.

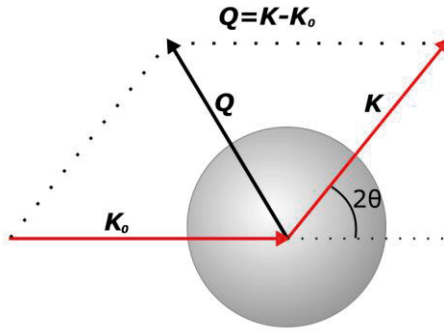


Figure 32: Definition of the scattering vector \mathbf{Q} during a scattering event between the scattered beam \mathbf{K} and the primary beam \mathbf{K}_0 .

The scattering vector \mathbf{Q} describes the momentum transfer during a scattering event, which can be graphically illustrated, as shown in Figure 32. Mathematically, the scattering vector can be defined as the difference between the scattered propagation vector and the incoming beam propagation vector $\mathbf{Q} = \mathbf{K} - \mathbf{K}_0$ [72]. As seen in Figure 32, the magnitude of the scattering vector, q , is related to the scattering angle and is mathematically described as shown below in Equation (21), where λ is the X-ray wavelength and θ is the scattering angle. The magnitude of the scattering vector is a common unit to use in XRD instead of the scattering angle since it is wavelength independent.

$$q = |\mathbf{Q}| = \frac{4\pi}{\lambda} \sin(\theta) \quad (21)$$

For X-ray diffraction measurements on single crystals, the sample must be rotated to fulfill the diffraction conditions in different directions, and a pattern of discrete spots would be seen. If several crystallites in the volume of the X-ray beam are randomly oriented relative to each other, there will be more atomic planes oriented such that the diffraction condition is met. In the extreme case of an infinite number of crystallites, there would be a crystallite with a set of lattice planes that meet the diffraction condition for each direction, which adds up to solid rings in reciprocal space or on the detector. This is what is known as powder diffraction, and the rings are called powder rings, as seen in Figure 33. Thinking in terms of Bragg's law, that there will always be crystallites oriented so that Bragg's law is fulfilled for an infinite number of crystallites. The powder rings all correspond to a specific momentum transfer and lie at a scattering angle of 2θ relative to the direct beam. Each ring corresponds to diffraction from a specific set of lattice planes rotated differently in real space.

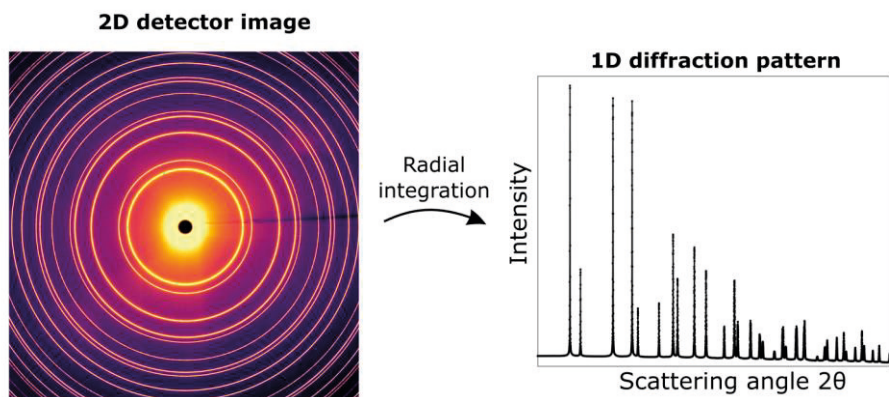


Figure 33: 2D diffraction pattern recorded on an area detector and the corresponding one-dimensional diffraction pattern for a CeO_2 sample with an FCC structure.

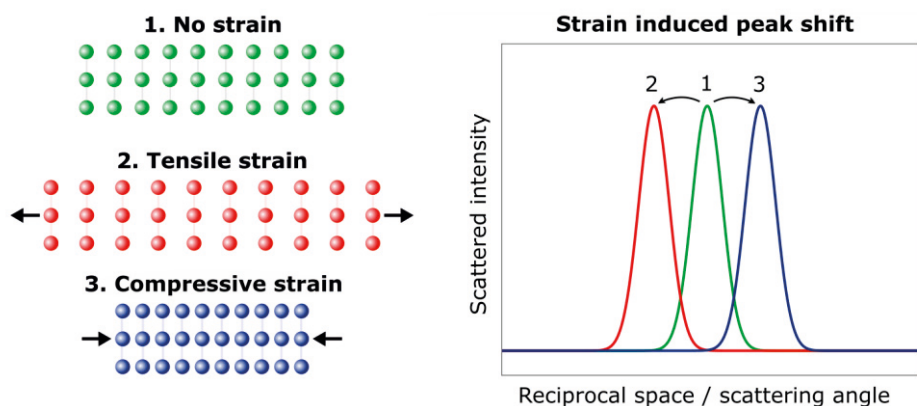


Figure 34: Influence of lattice strain on peak position. Tensile strain leads to a shift toward a lower scattering angle, and compressive strain results in a shift toward a higher scattering angle.

The position of the atoms in the crystal lattice may systematically deviate from their equilibrium position, which is known as strain. This can originate from externally applied forces; if a compressive force is applied to a crystal, the distance between lattice planes in that direction will decrease, and if a tensile force is applied, the lattice plane spacing will increase. If the lattice plane spacing changes in real space, the diffraction peaks will shift in reciprocal space, as seen in Figure 34. Due to the reciprocal nature of the transformation between real and reciprocal space, if the lattice plane spacing increases in real space, it will shift to a lower momentum

transfer in reciprocal space, resulting in a lower scattering angle and vice versa. This makes diffraction very suitable and sensitive to measure and quantify the displacements of atoms in a crystal. The strain ϵ in a direction $[hkl]$ in a lattice can be calculated as shown below in Equation (22), where d_{hkl} is the lattice plane spacing with Miller indices hkl , and d_{hkl}^0 is the equivalent lattice plane spacing but unstrained.

$$\epsilon_{hkl} = (d_{hkl} - d_{hkl}^0)/d_{hkl}^0 \quad (22)$$

Grazing Incidence Geometry

Since electrochemical reactions take place at the surface of the electrodes, it is of great interest to obtain structural and chemical information from the surface. As discussed, XPS is an inherently surface-sensitive technique. However, the strong interaction of electrons with matter also makes it difficult to perform real electrochemical experiments *in situ* combined with XPS. XRD and XANES, which are not electron-based techniques and rely on hard X-rays, are not inherently surface-sensitive. However, the surface sensitivity of these techniques can be enhanced by performing the measurement in a grazing incidence geometry where the X-ray beam intercepts the sample surface with an incidence angle of less than one degree, as shown in Figure 35. When the X-ray beam enters the sample at such low incidence angles, the path length of the X-rays becomes very long without penetrating very deep into the sample. This results in a decay of intensity, following Beer-Lamberts law, as the X-rays penetrate into the sample. As a result, the X-rays that escape all originate from a volume close to the sample surface.

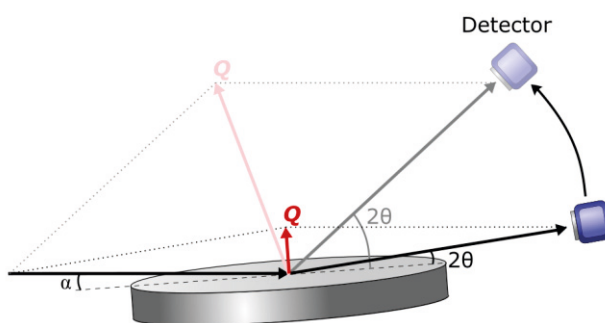


Figure 35: Grazing incidence geometry where the beam intercepts at the sample with an incidence angle α and the detector is scanned out of plane. Note that the Q vector changes direction as the detector is moved.

The incidence angle can be chosen below the critical angle for total external reflection to further increase the surface sensitivity. The penetration depth or information depth is defined as the depth into the sample surface from which 1/e, or 63% of the scattered signal, is generated [134]. The penetration depth as a function of the incidence angle is shown in Figure 36. Both geometrical effects and total external reflection are considered. As can be seen at incidence angles larger than the critical angle, the penetration depth is governed by geometrical effects, but below the critical angle for total external reflection, the penetration depth decreases more than one order of magnitude. So, to be surface-sensitive, the incidence angle should be chosen below the critical angle. The critical angle for X-rays is shown in Equation (23) below,

$$a_c = \sqrt{2\delta} \quad (23)$$

where δ is the real part of the refractive index of the substrate material, the real part of the refractive index is related to the scattering of X-rays.

The penetration depth, Z_{geo} , considering only geometrical effects, is shown below in Equation (24),

$$Z_{geo} = \frac{\sin(\alpha) \cdot \sin(\beta)}{\mu(\sin(\alpha) + \sin(\beta))} \quad (24)$$

where α is the incidence angle, β is the outgoing angle, and μ is the attenuation coefficient of the material, which is energy dependent.

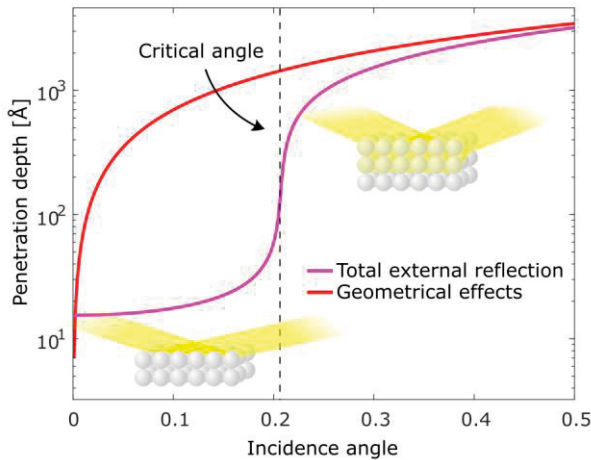


Figure 36: Penetration depth of X-rays in a grazing incidence geometry as a function of incidence angle for Pd at 18 keV.

The penetration depth, Z_{crit} , considering the effect of total external reflection, is described in Ref [134] and can be written as shown in Equation (25),

$$Z_{crit} = \frac{\lambda}{\frac{4\pi}{\sqrt{2}} \sqrt{(\alpha^2 - \alpha_c^2)^2 + 4\beta^2 - (\alpha^2 - \alpha_c^2)^2}} \quad (25)$$

where λ is the X-ray wavelength, α is the incidence angle, α_c is the critical angle, and β is the imaginary part of the refractive index related to absorption.

X-ray reflectivity

A technique that is based on grazing incidence is X-ray Reflectivity (XRR), where the intensity of the reflected X-ray beam is measured as a function of the incidence angle [135]. Similar to XRD but at a larger length scale, interference can occur between X-rays reflected at the interfaces of layers on a surface, which gives rise to constructive and destructive interference of the reflected X-ray beam at different incidence and exit angles, as shown schematically in Figure 37 a). An experimental XRR profile for the Ni-Cr-Mo alloy is shown in Figure 37 b). The position of these maxima and minima depends on the thickness of the films on the surface as well as their density (which affects the refractive index). At low incidence angles, below the critical angle for total external reflection, the full intensity of the beam is reflected. At angles above the critical angle, the reflected intensity rapidly decays several orders of magnitude. The decay of the reflected intensity depends on the roughness of the sample surface and the interfaces of the surface film. This technique is excellent for studying the thickness of thin oxide films on metal surfaces in real *in situ* electrochemical conditions. The measured reflectivity curves are modeled by calculated reflectivity profiles based on a physical layered model where the thickness, density, and roughness of each layer are defined [136, 137].

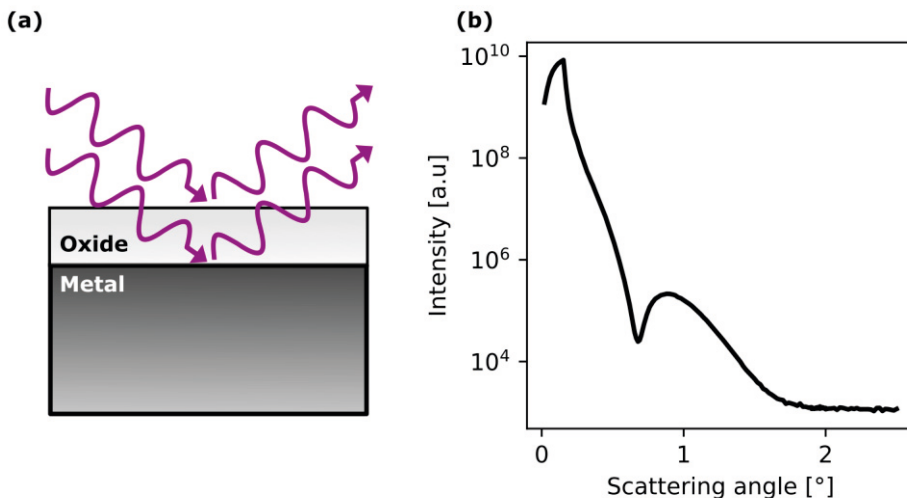


Figure 37: a) Schematic of X-rays reflected at the oxide surface and metal oxide interface giving rise to constructive or destructive interference. b) XRR curve measured for the Ni-Cr-Mo alloy in a 1 M NaCl solution, indicating the presence of a thin oxide film.

In situ vs. operando studies of electrochemical interfaces

Since electrochemical reactions take place at the surfaces of the electrodes, it is of great importance to understand the atomic structure and chemistry of the surface since it governs the reactivity and stability of the surface. As we have seen, electron-based techniques serve as the primary tool for surface scientists since they are inherently surface-sensitive. However, they become problematic to use in combination with liquid environments. These problems we can circumvent, as with the case of AP-XPS, which can be combined with electrochemistry. However, this still poses many challenges since the electrochemical reactions in the thin liquid layer that is probed with AP-XPS in the “dip and pull” method, are far from the electrochemical conditions that take place in a bulk electrolyte. With hard X-ray methods such as GI-XRD, we can measure the sample surface under true *operando* conditions where the sample is exposed to a bulk electrolyte environment and electrochemical potentials can be applied. Here, one significant drawback is that diffraction methods are not sensitive to amorphous structures, and we have seen from experience that oxide films that form on metal surfaces at room temperature in electrochemical conditions are not ordered. Therefore, we are “blind” to these thin oxide films from a diffraction point of view. With XRR, we can see even the amorphous thin oxides in true *operando* conditions. However, with XRR, we do not get any chemical information from the surface, only morphological. This leads us

to use XANES in total reflection mode, which makes a bulk-sensitive technique surface-sensitive. With this technique, we can study the surface chemistry in true *operando* conditions. With both XANES, AP-XPS, and XRR, we can see the chemistry, thickness, and morphology of the thin oxide films on the metal surface under electrochemical conditions.

Beam damage and beam-induced effects

The advancements that have been made in the photon flux and brilliance of X-ray sources have enabled many new experiments and opened the door for new scientific questions that people could only dream of pursuing when X-rays were first discovered. But with the recent developments of 4th generation synchrotron storage rings, such as MAX IV, the damage or alterations to samples is becoming an important issue. Under static experimental conditions, any alterations of the signal over time when the sample is exposed to X-rays can be attributed to beam damage in a straightforward way. However, during a time-resolved or *in situ* experiment where structural and chemical changes are expected to happen, it is difficult to separate contributions originating from beam damage from the desired real effects one wants to observe and investigate. [138]

X-rays primarily interact through photoelectric absorption in the energy range of 10 eV to 50 keV [139]. Every photoelectric absorption event is accompanied by a cascade of electrons and the generation of ions and radicals [140], and the generated electrons are thought to play a significant role in the beam damage phenomena in organic molecules [141]. The nature and extent of beam damage is highly material-system specific [142], which hints towards a complex range of mechanisms that can contribute to what, in the end, is observed as alterations of a sample caused by X-rays.

Exposing water to X-rays can induce radiolysis, generating reactive radicals [143, 144], which makes water a very strong oxidizer when irradiated. This we have observed during an experiment of corrosion in an oxygen free environment where rust (iron oxyhydroxide), which is not supposed to form under such conditions, was observed where the beam had impinged on the sample. This observation we cannot explain in any other way than the radiolysis of water, which generates oxidizing radicals.

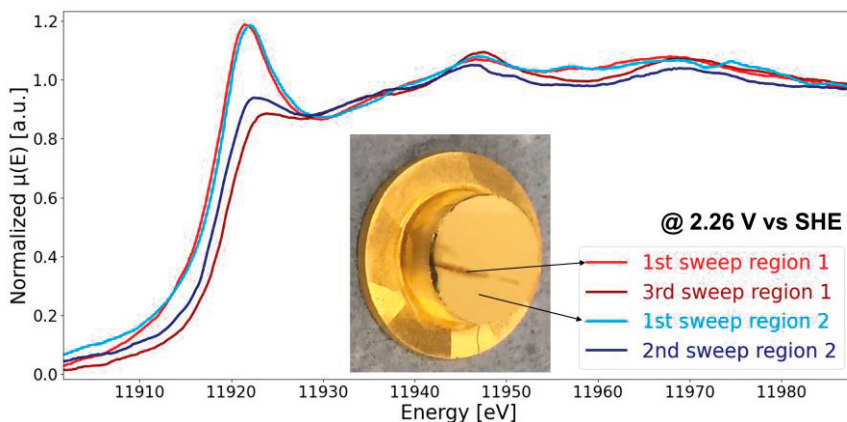


Figure 38: XANES data from the electrochemical surface oxidation of a Au polycrystal. Upon several sequential XANES energy sweeps, the Au oxide was reduced, as seen from the decreasing white line intensity. This was repeated in a second area, and the same effect was observed.

In Chapter 2, the Cabrera Mott model for oxidation of metals was introduced. This model predicts a self-limiting thickness when the barrier for dissociation of oxygen on the oxide surface is considered [56]. Surprisingly, our group once observed that the oxide film on Al locally grew thicker in the area exposed to the X-ray beam when the sample was measured in air. This was attributed to the photodissociation of oxygen in the air [145], which removes the necessity for molecular oxygen to dissociate at the oxide surface. Irradiating the oxygen molecules in the air may also generate oxygen radicals or other strongly oxidizing species. This has also been observed for platinum [146].

Photoreduction is also a commonly observed form of beam damage [138, 147, 148]. This we have experienced when working with electrodeposition and electrooxidation of gold. Au ions in solution are spontaneously reduced to the metallic form, which can be observed by the appearance of the metallic gold diffraction peak over time when the system is being irradiated. Also, solid Au oxide is reduced to its metallic state upon exposure to radiation, as seen in Figure 38. For oxides, it has also been observed that cations and anions can move to interstitial sites in the oxide lattice by the creation of Frankel defects [149, 150]. Combined with strong electric fields across thin oxide films, as in electrochemistry, this can result in the migration of these defects, which alters the electrochemical interface [151].

The Ni alloys have proved to be a system resilient towards beam damage, and damage was not clearly observed in this thesis work. However, measures were taken to reduce the amount of beam damage whenever possible, and several suggestions exist in the literature [116, 138, 152-154]. In our case, this was done by minimizing the exposure of a given area by spreading the beam footprint over the surface, as

well as moving across the surface and not measuring at the same point twice. A good way to monitor if beam damage occurs is to stay at one position and measure over time in static conditions to see if any changes in the signal are observed. Another thing to keep in mind for grazing incidence studies of electrochemical systems is to minimize the amount of beam that goes through the electrolyte without hitting the surface. This means having a sufficiently small vertical beam size such that the entire beam is spread across the sample surface. This will reduce the amount of unnecessary radiolysis in the water. For scattering studies, such as GI-XRD, XRR, or surface XRD, where one is not limited in energy to a specific absorption edge as in XANES, higher X-ray energies are beneficial to reduce the amount of beam damage since the absorption cross section decreases as a function of energy to a larger extent than the scattering cross section [139]. Another helpful method is to use 2D-SOR in conjunction with the X-ray measurements. The 2D-SOR may easily detect any beam damage as a darker streak across the surface, which is a fingerprint of radiation-induced changes of the surface, as seen in Figure 39 [68].

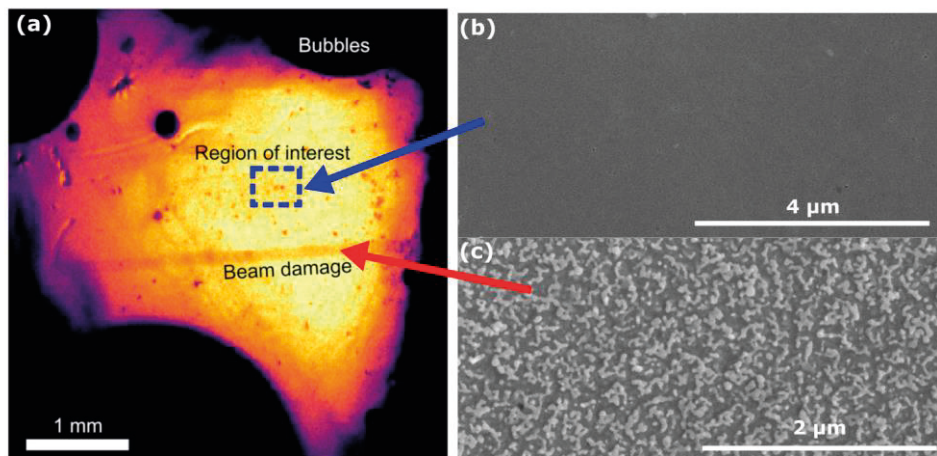


Figure 39: a) Example of beam damage of a Au(111) surface during a surface XRD experiment of Au electrooxidation and reduction. The dark streak across the surface is beam-induced damage. Modified from Ref [68]. b) SEM image of the surface region without beam damage. c) SEM image of sample area with beam damage.

5. Complementary techniques

Two-Dimensional Surface optical reflectance

2D-SOR is a rather trivial but useful technique where collimated light (we have operated this technique in the range of visible light) is impinging normally to a sample surface and is reflected and subsequently detected. This technique, which is sometimes also called reflectance microscopy, was introduced by Onderwaater et al. in 2017 [155, 156]. Since then, it has been further developed in the field of thermal catalysis and electrochemistry, in part here at Lund University [65, 66, 68, 157-166]. The 2D-SOR setup is shown in Figure 40 a). An LED light (660 nm) shines onto a beam splitter and is directed down towards the sample surface at normal incidence. Part of the light is reflected and travels up the microscope before it is detected. An optically transparent window at the top of our electrochemical cell dedicated to *in situ* synchrotron experiments allows for the combination of 2D-SOR with electrochemical measurements, as shown in Figure 40 b). A typical 2D-SOR image of the Ni alloy microstructure after preparation is shown in Figure 40 c).

The reflected intensity depends on the roughness of the surface, the optical properties of the surface that are material-dependent, and interference effects arising in thin films on the surface. For very thin oxides in the range of nanometers, the intensity decrease of the reflected light is very low. For the well-defined surface oxide formed on Pd, which is 2.5 Å thick, the intensity of the reflected light decreases by only 0.3 %, but this is well within the accuracy of 2D-SOR [159]. With 2D-SOR, we can follow relative changes in reflected intensity and report the reflected intensity with respect to the intensity at the time of potential zero. It is trivial to measure changes in reflectance upon subjecting a sample to electrochemical polarization, but it is less trivial to attribute these changes to some physical or chemical change of the surface. Therefore, 2D-SOR works as a great complement to other surface-sensitive techniques or to disentangle the local electrochemical response from a heterogeneous surface.

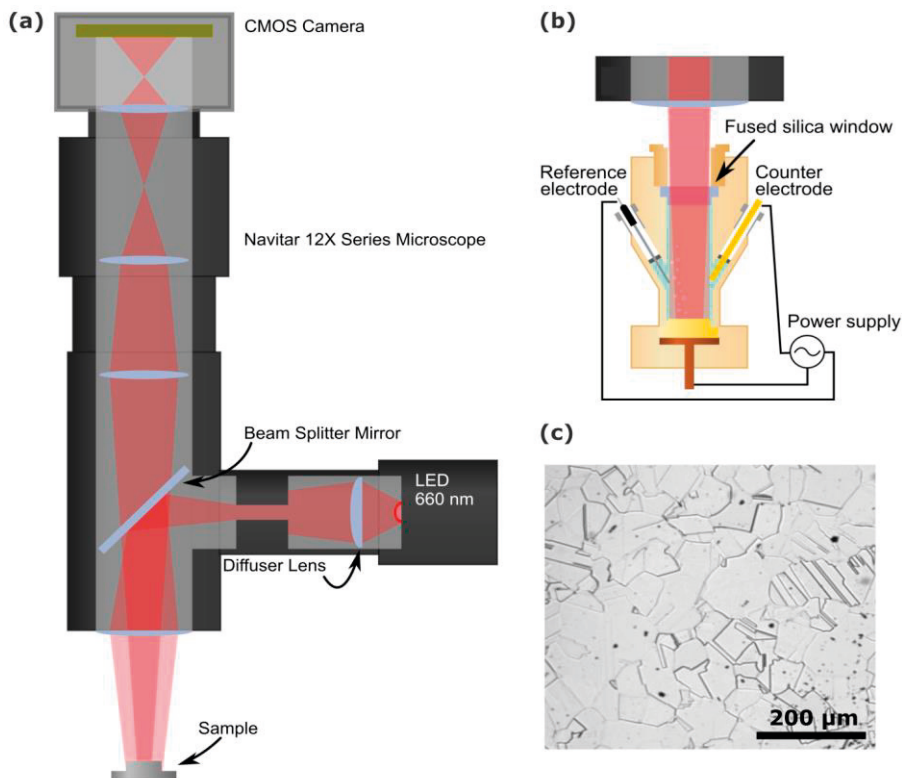


Figure 40: a) Schematic of the 2D-SOR setup. b) Combination of 2D-SOR with an electrochemical cell for synchrotron studies. c) Example of a 2D-SOR image of a Ni alloy sample (Ni 59).

Scanning electron microscopy

Scanning electron microscopy (SEM) is a technique used to image objects in the micron to submicron range. In the SEM, an electron gun is the radiation source, emitting electrons in the energy range of 1 keV to 30 keV. The electrons are accelerated down a column and focused to a point at the sample surface by electromagnetic lenses. This focused point is then raster scanned across the sample surface. The incident electrons can interact elastically or inelastically with the atoms in the sample. During inelastic interactions, electrons can be emitted from the atoms in the sample. These electrons are termed secondary electrons (SE) and have low energy compared to the incident electrons. Due to the lower energy, SE have a lower mean-free path inside the bulk of the sample, which means that only SE generated close to the surface can escape and be detected. Figure 41 shows the excitation

volume from where different signals can escape in the SEM. As seen, the SE can only escape from a small volume close to the sample surface. This makes SE imaging surface sensitive and increases the resolution since the SE are only generated within a small volume with the same area as the focused electron beam. SE imaging does not result in much chemical or compositional contrast. The most substantial contrast in secondary electron imaging is the edge contrast. When the incident beam hits an edge, more secondary electrons can escape, and the edge appears bright. SE imaging was used to study the corrosion scales that formed on the surface of the Ni-Cr-Mo alloy after corrosion, as shown in Figure 42 a). The electrons can also be back-scattered and detected. Back-scattered electron (BSE) imaging can result in chemical contrast, where heavier atoms scatter the electrons more strongly, or channeling contrast where crystalline grains of different orientation can be distinguished as in Figure 42 b).

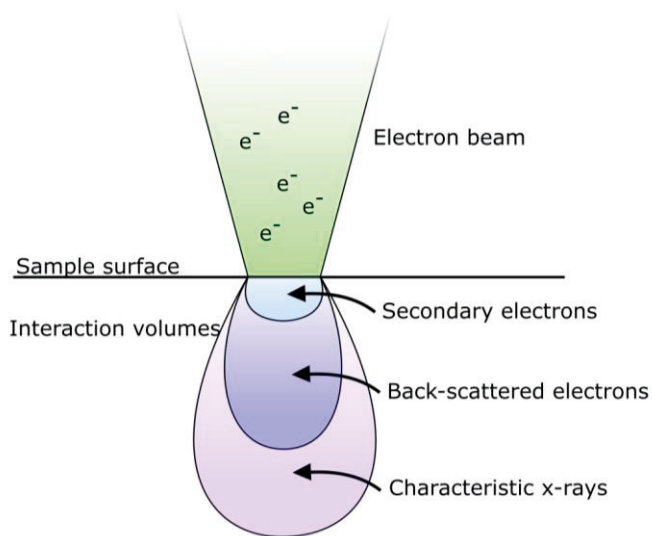


Figure 41: A schematic cross-section view of the excitation volume of different signals generated in SEM.

The SEM can also be coupled with Energy Dispersive Spectroscopy (EDS), where XRF is induced by the excitation of atoms in the sample by the primary electron beam. In this way, EDS spectra can be collected at every point in the image to make a spatially resolved map of the elements present. This technique has a low energy resolution, which does not allow for the separation of different chemical states but only elemental information.

Electron backscatter diffraction (EBSD) is another technique performed in an SEM where, at each point, the backscattered diffraction pattern is recorded and analyzed such that the local orientation of crystalline material can be determined at each point in the image. This results, in the end, in a map of the crystallographic orientation of each grain in a polycrystalline material.

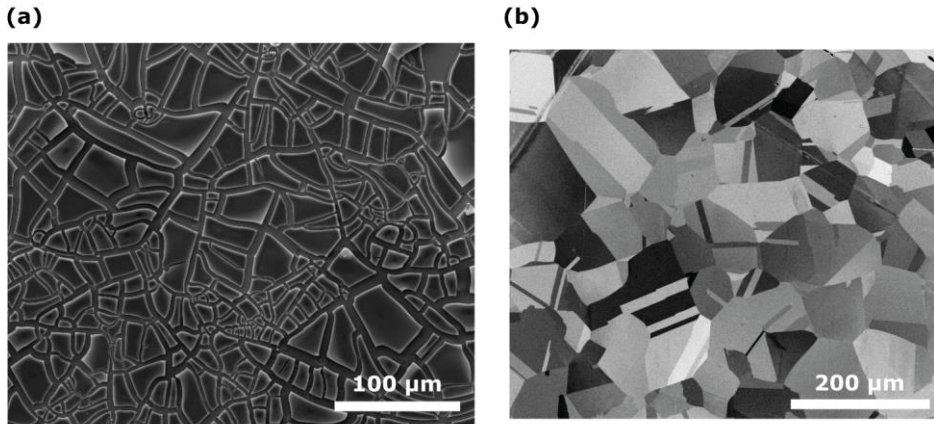


Figure 42: SEM images. a) Secondary electron image of corrosion scales formed on the Ni-Cr-Mo alloy surface. b) Back-scatter electron image of the Ni-Cr-Mo alloy microstructure.

6. Summary of papers

The papers included in this thesis can be separated into three main topics. First, the study of passive film formation and their thickness and composition. Second, the study of passive film breakdown under electrochemical conditions. Lastly, this thesis also covers some method development dedicated to new ways of studying electrochemical surfaces *in situ* with means of optical and X-ray-based techniques.

Passive film formation

Paper I.

Thickness and composition of native oxides and near-surface regions of Ni superalloys

In this paper, XPS and XRR were used to study the thickness and chemical composition of the spontaneously air-formed native oxide films on three different grades of industrial Ni-based alloys (alloy 59, 625, and 718). Both XPS and XRR reveal that the surface of all three alloys is covered by a 1 nm thick oxide layer. On top of the oxide layer, one monolayer of hydroxide is present. The oxides were enriched in Cr^{3+} , $\text{Mo}^{(4,5,6)+}$, and Nb^{5+} oxide, while no Ni was present in the oxide, even if Ni is the base metal in the alloy. The alloy composition right under the oxide layer was also accessed with XPS, and it was found that Ni was heavily enriched while Cr and the other oxide-forming elements were depleted just underneath the oxide film. It was also found, using thermodynamics, that the oxide composition correlated with the enthalpy of oxide formation for the metal elements in the alloy.

Paper II.

Dynamics of early-stage oxide formation on a Ni Cr-Mo alloy

In this paper, the early-stage oxide formation on Ni alloy 59 was studied *in situ* using XPS. The experiments were carried out in the UHV system at the FlexPES beamline, and the native oxide was removed by argon sputtering. Afterward, O_2 was dosed at 10^{-8} mbar while XPS was measured. Immediately upon oxygen exposure,

Cr³⁺ oxide, Mo⁴⁺, and Mo⁶⁺ oxide were formed, and after 20 L of O₂ exposure, a self-limiting thickness was reached. It was found that this self-limiting thickness was caused by the depletion of Cr and Mo near the surface. A mechanism to explain the bi-layer oxide model observed for Ni-Cr-Mo alloys is also proposed.

Paper III.

Synchrotron XPS and Electrochemical Study of Aging Effect on Passive Film of Ni Alloys

In this paper, XPS was used to study the effect of aging time on the oxide composition, thickness, and electrochemical properties of Ni alloy 59 and 625. The native air-formed oxide film was measured, then the sample surfaces were cleaned by argon sputtering to remove the oxide. The clean metallic surfaces were then exposed to air for 5 minutes, after which XPS was again measured. It was found that after 5 minutes in air, the oxide film was thinner and less Cr-rich compared to the sample stored in air for one month. It was also found that the open circuit potential, which is proportional to the nobility of the surface, was much lower right after polishing but reached the same value as the aged samples after one hour in 1 M NaCl electrolyte. This study indicates that even if the initial oxide formation is rapid, there are changes occurring in the oxide thickness and composition also during longer timescales.

Passive film breakdown

Paper IV.

The Oxygen Evolution Reaction Drives Passivity Breakdown for Ni–Cr–Mo Alloys

In this paper, AP-XPS, XANES, XRF, GI-XRD, and XRR were combined *in situ* together with electrochemical methods to study the passive film growth and breakdown during electrochemical polarization of Ni alloy 59. It was found that the material is stable and passive until the onset of the Oxygen Evolution Reaction (OER), where an enrichment of Mo⁶⁺ oxide and Cr³⁺ hydroxide is seen on the surface. At the onset of OER, severe dissolution of the alloy also takes place. From the quantitative analysis of the dissolution current, it was found that the OER contributes significantly to the total measured electrochemical current. From *in situ* XANES measurements from the electrolyte, it was possible to exclude Cr⁶⁺ as a dissolution product, which indicates that the observed passivity breakdown mechanism is different from the typical transpassive breakdown mechanism of Cr-containing alloys. Lastly, this mechanism of passivity breakdown is discussed in

relation to the degradation of electrocatalyst model systems of IrO₂ and RuO₂ under OER conditions.

Paper V.

Operando Surface Optical Reflectance Microscopy Study of Corrosion Film Growth on a Ni-Cr-Mo Alloy During Anodic Polarization

In this paper, 2D-SOR was used to follow the formation of corrosion products on the surface of Ni alloy 59 at increasingly elevated potentials. The growth of corrosion products on the surface results in constructive and destructive interference of the light reflected from the metal/corrosion product interface and the surface of the corrosion product film. This gives rise to oscillations in the 2D-SOR intensity while the corrosion product film is growing. From these oscillations, the total thickness and the growth rate of the corrosion products could be determined. The *in situ* 2D-SOR data was complemented by *ex situ* SEM and EDS measurements of the corrosion product morphology, thickness, and composition.

Method development

Paper VI.

In situ quantitative analysis of electrochemical oxide film development on metal surfaces using ambient pressure X-ray photoelectron spectroscopy: Industrial alloys

In this paper, AP-XPS combined with electrochemistry was used to study the passive film growth of Ni-59 *in situ*. The methodology of “dip and pull” was expanded to industrial alloys with multiple elements to be measured. To facilitate this, AP-XPS was measured without potential control, which allowed for increased stability of the system. This made it possible to perform a quantitative analysis of the oxide film thickness and composition where the water layer and attenuation of the photoelectrons through the water vapor environment were considered.

Paper VII.

An electrochemical cell for 2-dimensional surface optical reflectance during anodization and cyclic voltammetry

In this paper, an electrochemical flow cell was developed for combining 2D-SOR and synchrotron measurements with electrochemistry. A glass window at the top of

the cell gives optical access for 2D-SOR measurements from the electrode surface while exposed to the electrolyte and under potential control. As a proof of principle, anodization of Al, cyclic voltammetry of Au(111) and Pt(111) was used. It was found that the derivative of the 2D-SOR signal follows the current in the cyclic voltammogram.

Paper VIII.

Operando Reflectance Microscopy on Polycrystalline Surfaces in Thermal Catalysis, Electrocatalysis, and Corrosion

In this paper, the 2D-SOR capabilities were further developed into a microscope and applied to detailed studies of polycrystalline materials with three examples: CO oxidation over polycrystalline Pd in the gas phase, electrooxidation and reduction of a Au polycrystalline surface, and cyclic voltammetry of a duplex stainless steel sample. The 2D-SOR data was also complimented with EBSD in the case of Au and Pd, which allows for the direct correlation between surface orientation and the 2D-SOR signal. This also enabled the disentanglement of the global electrochemical current response into the contribution from each grain in the case of Au. It also allowed us to establish the relationship between surface orientation and overpotential for surface oxidation.

Paper IX.

Probing the electrode-electrolyte interface using operando total reflection X-ray absorption spectroscopy

In this paper, a demonstration of *in situ* total external reflection XANES applied to electrochemistry is presented. By measuring XANES in total reflection, very high surface sensitivity can be achieved for an otherwise bulk-sensitive technique. Two case studies are chosen: the anodic polarization of a Ni-Cr-Mo alloy in sodium chloride at pH 7 and pH 12, as well as the electrooxidation of a gold polycrystalline surface in sulfuric acid. For the Ni alloy, a difference in surface chemistry was observed, with more Ni(OH)₂ present in pH 12. At higher anodic potentials, thicker layers of MoO₃ were observed at both pH 7 and pH 12. For the gold sample, a thin layer of Au(OH)₃ (sub-nanometer) was detected at the potential corresponding to surface oxidation in the cyclic voltammogram. At higher anodic potential where OER occurs, a thicker (few nanometer) hydroxide layer was observed. This shows the capabilities of the technique to detect nanometer thick oxide layers during *operando* conditions in an electrochemical environment.

7. Summary & Outlook

This thesis has focused on the development and utilization of *in situ* and *operando* synchrotron and optical techniques to access structural and chemical information from the solid-liquid interface of electrode surfaces exposed to an electrolyte. Electrochemistry is vital not only for understanding and studying corrosion but also for electrocatalysis, fuel cells, and batteries. The electrochemical properties, such as stability and reactivity, are governed by the atomic structure and the chemistry of the electrode surface. It is, therefore, vital to understand, measure, and quantify the structure and chemistry of the electrode surface under realistic electrochemical conditions. Traditional electron-based surface-sensitive techniques operated in UHV have provided detailed chemical and structural information and have been the backbone of surface science for decades [167, 168], but these techniques are not compatible with electrochemistry. Due to the presence of the electrolyte, which is an absorbing medium compared to vacuum or the gas phase, the electrode surface is notoriously difficult to study under realistic conditions [169].

In this thesis, I have worked with advanced techniques that make it possible to bridge the realm of electrochemistry and surface analysis with varying degrees of *in situ* capabilities. AP-XPS provides excellent surface sensitivity and chemical sensitivity. However, this technique is difficult to operate in combination with electrochemistry, and the low mean free path of photoelectrons limits the electrolyte film in the analyzed area to a few nanometers. This introduces mass-transfer issues and a significant potential drop such that if measured under “potential control”, the actual electrochemical potential at the point measured with AP-XPS might not be the true electrochemical potential applied with the potentiostat. We have also developed and used XANES in total reflection for electrochemical studies. This is a hard X-ray technique that relies on photons in and photons out, which means that penetrating through millimeters of electrolyte with the X-ray beam is no problem. It is, however, less trivial to deconvolute the spectra and assign specific chemical states. Also, quantitative analysis of oxide film composition and thicknesses is not yet developed for this technique, but I believe that it holds great potential. GI-XRD and XRR can be used in true *operando* conditions, just like total reflection XANES, and can provide structural information from the interface exposed to an electrolyte and under electrochemical conditions. These X-ray-based techniques, which do not provide any spatially resolved information from the surface, can be combined with 2D-SOR to obtain a microscopic view of the sample surface during the experiments.

This can be used for detailed analysis of oxide formation or to follow the growth of corrosion products. But it can also be a valuable tool to check, in real-time at the synchrotron, for beam damage, heterogeneous sample behavior, and bubble formation, which can indicate the presence of, for example, oxygen evolution.

With these techniques, I have been able to follow the passive film growth and breakdown of Ni alloys under electrochemical conditions and at elevated anodic potentials. From studies in UHV, we have characterized the native oxide films on these Ni alloys in detail, and with AP-XPS, we could also perform a detailed quantitative analysis of the oxide films after electrochemical exposures. From the combination of all the above-mentioned X-ray-based techniques, I could obtain a detailed picture of the passivity breakdown at increased anodic potentials and attribute this to the presence of the oxygen evolution reaction, which induces passivity breakdown through a mechanism that was previously unknown and different from that of typical Cr containing alloys.

I believe that the techniques and methodology used and developed during this thesis can have a great impact on the electrochemical community, and it opens the door to tackle open questions that were previously difficult to answer with conventional electrochemical techniques or traditional *ex situ* surface analysis. I also believe that electrochemistry is an increasingly important topic with applications that may have a great impact on the societal challenges that we face. Very important research fields, such as CO₂ reduction into useful chemicals [170, 171], green production of H₂ for use in industrial sectors and energy storage [172], fuel cells [173], batteries [174], as well as corrosion, are all encompassed by the field of electrochemistry. Corrosion results in huge costs [2, 3], and the production of metals is responsible for 40 % of industrial greenhouse emissions and 10 % of our global energy consumption [5, 175]. Therefore, a fundamental understanding of corrosion and corrosion inhibition could have a significant impact on reducing greenhouse gas emissions.

With the advances in modern synchrotrons, dream experiments can become a reality. For example, with *operando* AP-XPS combined with electrochemistry, the passive film formation at anodic potentials and reduction at cathodic potentials could be studied in real time to elucidate the dynamics of oxide formation, which governs passivity. Also, *operando* AP-XPS combined with electrochemistry could be used to study the interaction of organic corrosion inhibitors with metal surfaces in realistic aqueous conditions to obtain a better understanding of the interplay between these molecules, metal or oxide surfaces, and the aqueous environment. Total reflection XANES could be used in real time to study the active state and the degradation mechanism of important electrocatalysts for OER, which is the bottleneck in green H₂ production. These materials could be Pt and IrO₂ for acidic conditions, as well as more earth-abundant and affordable materials such as Ni and Co oxides and hydroxides used in alkaline media. XANES measured *in situ* from

the electrolyte could also be used to shed light on the degradation mechanism of electrocatalysts by studying the chemical state of the dissolution products.

I am happy, and I feel privileged to have been able to contribute (however insignificantly) to the body of human knowledge. And I hope that the advances in experimental methodology that came out from this Ph.D. thesis may help to tackle some of the great societal challenges that we have in front of us.

References

1. Macdonald, D.D., *Passivity—the key to our metals-based civilization*. Pure and Applied Chemistry, 1999. **71**(6): p. 951-978.
2. Koch, G., *I - Cost of corrosion*, in *Trends in Oil and Gas Corrosion Research and Technologies*, A.M. El-Sherik, Editor. 2017, Woodhead Publishing: Boston. p. 3-30.
3. Hou, B., X. Li, X. Ma, C. Du, D. Zhang, M. Zheng, W. Xu, D. Lu, and F. Ma, *The cost of corrosion in China*. npj Materials Degradation, 2017. **1**(1): p. 4.
4. Raabe, D., C.C. Tasan, and E.A. Olivetti, *Strategies for improving the sustainability of structural metals*. Nature, 2019. **575**(7781): p. 64-74.
5. Raabe, D., *The Materials Science behind Sustainable Metals and Alloys*. Chemical Reviews, 2023. **123**(5): p. 2436-2608.
6. Bender, R., D. Féron, D. Mills, S. Ritter, R. Bäbler, D. Bettge, I. De Graeve, A. Dugstad, S. Grassini, T. Hack, et al., *Corrosion challenges towards a sustainable society*. Materials and Corrosion, 2022. **73**(11): p. 1730-1751.
7. Zhong, X., M. Hu, S. Deetman, B. Steubing, H.X. Lin, G.A. Hernandez, C. Harpprecht, C. Zhang, A. Tukker, and P. Behrens, *Global greenhouse gas emissions from residential and commercial building materials and mitigation strategies to 2060*. Nature Communications, 2021. **12**(1): p. 6126.
8. Schmuki, P.J.J.o.S.S.E., *From Bacon to barriers: a review on the passivity of metals and alloys*. 2002. **6**: p. 145-164.
9. Macdonald, D.D., *The history of the Point Defect Model for the passive state: A brief review of film growth aspects*. Electrochimica Acta, 2011. **56**(4): p. 1761-1772.
10. Evans, U.R., *The Passivity of Iron*. Nature, 1931. **128**(3243): p. 1062-1065.
11. Olsson, C.O.A. and D. Landolt, *Passive films on stainless steels—chemistry, structure and growth*. Electrochimica Acta, 2003. **48**(9): p. 1093-1104.
12. Evertsson, J., F. Bertram, F. Zhang, L. Rullik, L.R. Merte, M. Shipilin, M. Soldemo, S. Ahmadi, N. Vinogradov, F. Carlà, et al., *The thickness of native oxides on aluminum alloys and single crystals*. Applied Surface Science, 2015. **349**: p. 826-832.
13. Maurice, V. and P. Marcus, *Progress in corrosion science at atomic and nanometric scales*. Progress in Materials Science, 2018. **95**: p. 132-171.
14. Marcus, P., *Surface science approach of corrosion phenomena*. Electrochimica Acta, 1998. **43**(1): p. 109-118.
15. Paulonis, D.F. and J.J.J.S. Schirra, *Alloy 718 at Pratt & Whitney—Historical perspective and future challenges*. 2001. **718**(706): p. 13-23.

16. Sidhu, T., R. Agrawal, S.J.S. Prakash, and c. technology, *Hot corrosion of some superalloys and role of high-velocity oxy-fuel spray coatings—a review*. 2005. **198**(1-3): p. 441-446.
17. Darolia, R.J.I.m.r., *Development of strong, oxidation and corrosion resistant nickel-based superalloys: critical review of challenges, progress and prospects*. 2019. **64**(6): p. 355-380.
18. Klapper, H.S., N.S. Zadorozne, and R.B.J.A.M.S. Rebak, *Localized corrosion characteristics of nickel alloys: a review*. 2017. **30**: p. 296-305.
19. Patel, N.S., V. Pavlík, M.J.C.R.i.S.S. Boča, and M. Sciences, *High-temperature corrosion behavior of superalloys in molten salts—a review*. 2017. **42**(1): p. 83-97.
20. Chittewar, S.L. and N.G.J.M.T.P. Patil, *Surface integrity of conventional and additively manufactured nickel superalloys: A review*. 2021. **44**: p. 701-708.
21. Turkdogan, E., R.J.T.M. Fruehan, Shaping, S. Treating of Steel, and t.e. Refining Volume, RJ Fruehan, ed., AISE Steel Foundation, Pittsburgh, *Fundamentals of iron and steelmaking*. 1998. **11**: p. 125-126.
22. Vogl, V., M. Åhman, and L.J. Nilsson, *The making of green steel in the EU: a policy evaluation for the early commercialization phase*. Climate Policy, 2021. **21**(1): p. 78-92.
23. Kanolt, C.W., *Melting points of some refractory oxides*. 1914: US Government Printing Office.
24. Hlavac, J.J.P. and A. Chemistry, *Melting temperatures of refractory oxides: Part I*. 1982. **54**(3): p. 681-688.
25. Wang, Z., C. Carrière, A. Seyeux, S. Zanna, D. Mercier, and P. Marcus, *Thermal stability of surface oxides on nickel alloys (NiCr and NiCrMo) investigated by XPS and ToF-SIMS*. Applied Surface Science, 2022. **576**: p. 151836.
26. Momma, K. and F. Izumi, *VESTA: a three-dimensional visualization system for electronic and structural analysis*. Journal of Applied crystallography, 2008. **41**(3): p. 653-658.
27. HAAN, Y.D., *Refinement of the a Al₂O₃, Ti₂O₃, V₂O₃ and Cr₂O₃ structures*. Zeitschrift für Kristallographie-Crystalline Materials, 1962. **117**(1-6): p. 235-237.
28. Andersson, G., A. Magneli, L.G. Sillén, and M. Rottenberg, *On the crystal structure of molybdenum trioxide*. Acta Chem. Scand, 1950. **4**: p. 793-797.
29. Bolzan, A.A., B.J. Kennedy, and C.J. Howard, *Neutron powder diffraction study of molybdenum and tungsten dioxides*. Australian Journal of Chemistry, 1995. **48**(8): p. 1473-1477.
30. Machet, A., A. Galtayries, S. Zanna, L. Klein, V. Maurice, P. Jolivet, M. Foucault, P. Combrade, P. Scott, and P. Marcus, *XPS and STM study of the growth and structure of passive films in high temperature water on a nickel-base alloy*. Electrochimica Acta, 2004. **49**(22): p. 3957-3964.
31. Maurice, V., W.P. Yang, and P. Marcus, *XPS and STM Study of Passive Films Formed on Fe-22Cr(110) Single-Crystal Surfaces*. Journal of The Electrochemical Society, 1996. **143**(4): p. 1182.

32. Kunze, J., V. Maurice, L.H. Klein, H.-H. Strehblow, and P. Marcus, *In situ STM study of the duplex passive films formed on Cu(111) and Cu(001) in 0.1 M NaOH*. Corrosion Science, 2004. **46**(1): p. 245-264.
33. Maurice, V., W.P. Yang, and P. Marcus, *XPS and STM Investigation of the Passive Film Formed on Cr(110) Single-Crystal Surfaces*. Journal of The Electrochemical Society, 1994. **141**(11): p. 3016.
34. Gambardella, P., Ž. Šljivančanin, B. Hammer, M. Blanc, K. Kuhnke, and K. Kern, *Oxygen Dissociation at Pt Steps*. Physical Review Letters, 2001. **87**(5): p. 056103.
35. Honkala, K. and K. Laasonen, *Oxygen Molecule Dissociation on the Al(111) Surface*. Physical Review Letters, 2000. **84**(4): p. 705-708.
36. Hla, S.W., P. Lacovig, G. Comelli, A. Baraldi, M. Kiskinova, and R. Rosei, *Orientalional anisotropy in oxygen dissociation on Rh(110)*. Physical Review B, 1999. **60**(11): p. 7800-7803.
37. Kapoor, R. and S.T. Oyama, *Measurement of solid state diffusion coefficients by a temperature-programmed method*. Journal of Materials Research, 1997. **12**(2): p. 467-473.
38. Cabrera, N. and N.F. Mott, *Theory of the oxidation of metals*. Reports on Progress in Physics, 1949. **12**(1): p. 163.
39. Fehlner, F.P. and N.F.J.O.o.m. Mott, *Low-temperature oxidation*. 1970. **2**(1): p. 59-99.
40. Ramírez, L.P., F. Bournel, J.-J. Gallet, L. Dudy, and F. Rochet, *Testing the Cabrera–Mott Oxidation Model for Aluminum under Realistic Conditions with Near-Ambient Pressure Photoemission*. The Journal of Physical Chemistry C, 2022. **126**(5): p. 2517-2530.
41. Henderson, J.D., A. Seyeux, S. Zanna, M.C. Biesinger, D.W. Shoesmith, J.J. Noël, and P. Marcus, *Investigating the transport mechanisms governing the oxidation of Hastelloy BC-1 by in situ ToF-SIMS*. Corrosion Science, 2019. **159**: p. 108138.
42. Shannon, R.D., *Revised effective ionic radii and systematic studies of interatomic distances in halides and chalcogenides*. 1976. **32**(5): p. 751-767.
43. Baran, J.D., H. Grönbeck, and A.J.P.r.l. Hellman, *Mechanism for limiting thickness of thin oxide films on aluminum*. 2014. **112**(14): p. 146103.
44. Leygraf, C., I.O. Wallinder, J. Tidblad, and T. Graedel, *Atmospheric corrosion*. 2016: John Wiley & Sons.
45. Cecchini, R. and G. Pelosi, *Alessandro Volta and his battery*. IEEE Antennas and Propagation Magazine, 1992. **34**(2): p. 30-37.
46. Ciobanu, M., J.P. Wilburn, M.L. Krim, and D.E. Cliffler, *1 - Fundamentals*, in *Handbook of Electrochemistry*, C.G. Zoski, Editor. 2007, Elsevier: Amsterdam. p. 3-29.
47. Bard, A.J. and L.R.J.E.m. Faulkner, *Fundamentals and applications*. 2001. **2**(482): p. 580-632.
48. Elgrishi, N., K.J. Rountree, B.D. McCarthy, E.S. Rountree, T.T. Eisenhart, and J.L. Dempsey, *A Practical Beginner's Guide to Cyclic Voltammetry*. Journal of Chemical Education, 2018. **95**(2): p. 197-206.

49. Compton, R.G. and C.E. Banks, *Understanding voltammetry*. 2018: World Scientific.
50. Marcus, R.A.J.T.J.o.c.p., *On the theory of oxidation-reduction reactions involving electron transfer. I*. 1956. **24**(5): p. 966-978.
51. Marcus, R.A.J.A.r.o.p.c., *Chemical and electrochemical electron-transfer theory*. 1964. **15**(1): p. 155-196.
52. Marcus, R.A., *Electron Transfer Reactions in Chemistry: Theory and Experiment (Nobel Lecture)*. 1993. **32**(8): p. 1111-1121.
53. Lefrou, C., P. Fabry, and J.C. Poignet, *Electrochemistry: The basics, with examples*. 2012. 1-353.
54. Strehblow, H.-H. and P. Marcus, *Fundamentals of corrosion*, in *Corrosion Mechanisms in Theory and Practice*. 2011, CRC Press. p. 13-116.
55. Macdonald, D.D., *The Point Defect Model for the Passive State*. Journal of The Electrochemical Society, 1992. **139**(12): p. 3434.
56. Baran, J.D., H. Grönbeck, and A. Hellman, *Mechanism for Limiting Thickness of Thin Oxide Films on Aluminum*. Physical Review Letters, 2014. **112**(14): p. 146103.
57. Macdonald, D.D., *On the Existence of Our Metals-Based Civilization: I. Phase-Space Analysis*. Journal of The Electrochemical Society, 2006. **153**(7): p. B213.
58. Bettini, E., C. Leygraf, and J.J.I.J.o.E.S. Pan, *Nature of current increase for a CoCrMo alloy: "transpassive" dissolution vs. water oxidation*. 2013. **8**(10): p. 11791-11804.
59. Larsson, A., A. Grespi, G. Abbondanza, J. Eihagen, D. Gajdek, K. Simonov, X. Yue, U. Lienert, Z. Hegedüs, A. Jeromin, et al., *The Oxygen Evolution Reaction Drives Passivity Breakdown for Ni-Cr-Mo Alloys*. Advanced Materials, 2023. **n/a**(n/a): p. 2304621.
60. Strehblow, H.-H., P.J.C.m.i.t. Marcus, and practice, *Mechanisms of pitting corrosion*. 1995. **201**: p. 238.
61. Marcus, P., V. Maurice, and H.H. Strehblow, *Localized corrosion (pitting): A model of passivity breakdown including the role of the oxide layer nanostructure*. Corrosion Science, 2008. **50**(9): p. 2698-2704.
62. Lin, L.F., C.Y. Chao, and D.D. Macdonald, *A Point Defect Model for Anodic Passive Films: II. Chemical Breakdown and Pit Initiation*. Journal of The Electrochemical Society, 1981. **128**(6): p. 1194.
63. Frankel, G.S., *Pitting Corrosion of Metals: A Review of the Critical Factors*. Journal of The Electrochemical Society, 1998. **145**(6): p. 2186.
64. Morrison, S.R. and S. Morrison, *Electrochemistry at semiconductor and oxidized metal electrodes*. Vol. 126. 1980: Springer.
65. Linpé, W., G.S. Harlow, A. Larsson, G. Abbondanza, L. Rämisch, S. Pfaff, J. Zetterberg, J. Evertsson, and E. Lundgren, *An electrochemical cell for 2-dimensional surface optical reflectance during anodization and cyclic voltammetry*. Review of Scientific Instruments, 2020. **91**(4).
66. Pfaff, S., A. Larsson, D. Orlov, G.S. Harlow, G. Abbondanza, W. Linpé, L. Rämisch, S.M. Gericke, J. Zetterberg, and E. Lundgren, *Operando Reflectance Microscopy on*

- Polycrystalline Surfaces in Thermal Catalysis, Electrocatalysis, and Corrosion*. ACS Applied Materials & Interfaces, 2021. **13**(16): p. 19530-19540.
67. Weber, T., V. Vonk, D. Escalera-López, G. Abbondanza, A. Larsson, V. Koller, M.J.S. Abb, Z. Hegedüs, T. Bäcker, U. Lienert, et al., *Operando Stability Studies of Ultrathin Single-Crystalline IrO₂(110) Films under Acidic Oxygen Evolution Reaction Conditions*. ACS Catalysis, 2021. **11**(20): p. 12651-12660.
 68. Linpé, W., L. Rämisch, G. Abbondanza, A. Larsson, S. Pfaff, L. Jacobse, J. Zetterberg, L. Merte, A. Stierle, Z. Hegedues, et al., *Revisiting Optical Reflectance from Au(111) Electrode Surfaces with Combined High-Energy Surface X-ray Diffraction*. Journal of The Electrochemical Society, 2021. **168**(9): p. 096511.
 69. Harlow, G.S., E. Lundgren, and M. Escudero-Escribano, *Recent advances in surface x-ray diffraction and the potential for determining structure-sensitivity relations in single-crystal electrocatalysis*. Current Opinion in Electrochemistry, 2020. **23**: p. 162-173.
 70. Fuchs, T., J. Drnec, F. Calle-Vallejo, N. Stubb, D.J.S. Sandbeck, M. Ruge, S. Cherevko, D.A. Harrington, and O.M. Magnussen, *Structure dependency of the atomic-scale mechanisms of platinum electro-oxidation and dissolution*. Nature Catalysis, 2020. **3**(9): p. 754-761.
 71. Röntgen, W.C.J.S., *On a new kind of rays*. 1896. **3**(59): p. 227-231.
 72. Als-Nielsen, J.M., *Des X-rays and their interaction with matter*, in *Elements of Modern X-ray Physics*. 2011. p. 1-28.
 73. Als-Nielsen, J.M., *Des Refraction and reflection from interfaces*, in *Elements of Modern X-ray Physics*. 2011. p. 69-112.
 74. Als-Nielsen, J.M., *Des Sources*, in *Elements of Modern X-ray Physics*. 2011. p. 29-67.
 75. Koch, E.E., *Handbook on synchrotron radiation Vol I*. 1983, Netherlands: North-Holland.
 76. Wille, K., *Introduction to insertion devices*. 1998.
 77. Elleaume, P., *Theory of undulators and wigglers*. 1990.
 78. Tavares, P.F., S.C. Leemann, M. Sjöström, and Å.J.J.o.s.r. Andersson, *The MAX IV storage ring project*. 2014. **21**(5): p. 862-877.
 79. Martensson, N. and M. Eriksson, *The saga of MAX IV, the first multi-bend achromat synchrotron light source*. Nuclear Instruments and Methods in Physics Research Section A: Accelerators, Spectrometers, Detectors and Associated Equipment, 2018. **907**: p. 97-104.
 80. Tavares, P.F., E. Al-Dmour, Å. Andersson, F. Cullinan, B.N. Jensen, D. Olsson, D.K. Olsson, M. Sjöström, H. Tarawneh, and S.J.J.o.s.r. Thorin, *Commissioning and first-year operational results of the MAX IV 3 GeV ring*. 2018. **25**(5): p. 1291-1316.
 81. Balewski, K. *Commissioning of Petra III*. in *Proceedings of 1st International Particle Accelerator Conference: IPAC*. 2010.
 82. Drube, W., M. Bieler, W. Caliebe, H. Schulte-Schrepping, J. Spengler, M. Tischer, and R. Wanzenberg. *The Petra III Extension*. in *AIP Conference Proceedings*. 2016. AIP Publishing.

83. Bilderback, D.H., *The potential of cryogenic silicon and germanium X-ray monochromators for use with large synchrotron heat loads*. Nuclear Instruments and Methods in Physics Research Section A: Accelerators, Spectrometers, Detectors and Associated Equipment, 1986. **246**(1): p. 434-436.
84. Bilderback, D.H., A.K. Freund, G.S. Knapp, and D.M.J.J.o.s.r. Mills, *The historical development of cryogenically cooled monochromators for third-generation synchrotron radiation sources*. 2000. **7**(2): p. 53-60.
85. Petersen, H., C. Jung, C. Hellwig, W.B. Peatman, and W. Gudat, *Review of plane grating focusing for soft x-ray monochromators*. Review of Scientific Instruments, 1995. **66**(1): p. 1-14.
86. Follath, R. and F. Senf, *New plane-grating monochromators for third generation synchrotron radiation light sources*. Nuclear Instruments and Methods in Physics Research Section A: Accelerators, Spectrometers, Detectors and Associated Equipment, 1997. **390**(3): p. 388-394.
87. Yamauchi, K., H. Mimura, T. Kimura, H. Yumoto, S. Handa, S. Matsuyama, K. Arima, Y. Sano, K. Yamamura, K. Inagaki, et al., *Single-nanometer focusing of hard x-rays by Kirkpatrick-Baez mirrors*. Journal of Physics: Condensed Matter, 2011. **23**(39): p. 394206.
88. Mimura, H., S. Matsuyama, H. Yumoto, H. Hara, K. Yamamura, Y. Sano, M. Shibahara, K. Endo, Y. Mori, Y. Nishino, et al., *Hard X-ray Diffraction-Limited Nanofocusing with Kirkpatrick-Baez Mirrors*. Japanese Journal of Applied Physics, 2005. **44**(4L): p. L539.
89. Snigirev, A., V. Kohn, I. Snigireva, and B. Lengeler, *A compound refractive lens for focusing high-energy X-rays*. Nature, 1996. **384**(6604): p. 49-51.
90. Preobrajenski, A., A. Generalov, G. Öhrwall, M. Tchapyguine, H. Tarawneh, S. Appelfeller, E. Frampton, and N.J.J.o.S.R. Walsh, *FlexPES: a versatile soft X-ray beamline at MAX IV Laboratory*. 2023. **30**(4).
91. Zhu, S., M. Scardamaglia, J. Kundsén, R. Sankari, H. Tarawneh, R. Temperton, L. Pickworth, F. Cavalca, C. Wang, and H.J.J.o.s.r. Tissot, *HIPPIE: a new platform for ambient-pressure X-ray photoelectron spectroscopy at the MAX IV Laboratory*. 2021. **28**(2): p. 624-636.
92. Caliebe, W.A., V. Murzin, A. Kalinko, and M. Görlitz, *High-flux XAFS-beamline P64 at PETRA III*. AIP Conference Proceedings, 2019. **2054**(1).
93. Hollander, J.M. and D.A.J.S. Shirley, *The 1981 nobel prize in physics*. 1981. **214**(4521): p. 629-631.
94. Baer, D.R., K. Artyushkova, C. Richard Brundle, J.E. Castle, M.H. Engelhard, K.J. Gaskell, J.T. Grant, R.T. Haasch, M.R. Linford, C.J. Powell, et al., *Practical guides for x-ray photoelectron spectroscopy: First steps in planning, conducting, and reporting XPS measurements*. Journal of Vacuum Science & Technology A, 2019. **37**(3).
95. Major, G.H., J.W. Pinder, D.E. Austin, D.R. Baer, S.L. Castle, J. Čechal, B.M. Clark, H. Cohen, J. Counsell, A. Herrera-Gomez, et al., *Perspective on improving the quality of surface and material data analysis in the scientific literature with a focus*

- on *x-ray photoelectron spectroscopy (XPS)*. Journal of Vacuum Science & Technology A, 2023. **41**(3).
96. Einstein, A., *Über einen die Erzeugung und Verwandlung des Lichtes betreffenden heuristischen Gesichtspunkt*. 1905. **322**(6): p. 132-148.
 97. Roy, D. and D. Tremblay, *Design of electron spectrometers*. Reports on Progress in Physics, 1990. **53**(12): p. 1621.
 98. Hüfner, S., *Introduction and Basic Principles*, in *Photoelectron Spectroscopy: Principles and Applications*, S. Hüfner, Editor. 2003, Springer Berlin Heidelberg: Berlin, Heidelberg. p. 1-60.
 99. Shinotsuka, H., S. Tanuma, C.J. Powell, and D.R. Penn, *Calculations of electron inelastic mean free paths. X. Data for 41 elemental solids over the 50 eV to 200 keV range with the relativistic full Penn algorithm*. 2015. **47**(9): p. 871-888.
 100. Hüfner, S., S.J.P.S.P. Hüfner, and Applications, *Core levels and final states*. 2003: p. 61-107.
 101. Travnikova, O., K.J. Børve, M. Patanen, J. Söderström, C. Miron, L.J. Sæthre, N. Mårtensson, and S. Svensson, *The ESCA molecule—Historical remarks and new results*. Journal of Electron Spectroscopy and Related Phenomena, 2012. **185**(8): p. 191-197.
 102. Hill, J.M., D.G. Royce, C.S. Fadley, L.F. Wagner, and F.J. Grunthaner, *Properties of oxidized silicon as determined by angular-dependent X-ray photoelectron spectroscopy*. Chemical Physics Letters, 1976. **44**(2): p. 225-231.
 103. Fadley, C.S., R.J. Baird, W. Siekhaus, T. Novakov, and S.Å.L. Bergström, *Surface analysis and angular distributions in x-ray photoelectron spectroscopy*. Journal of Electron Spectroscopy and Related Phenomena, 1974. **4**(2): p. 93-137.
 104. Jablonski, A. and J. Zemek, *Overlayer thickness determination by XPS using the multiline approach*. 2009. **41**(3): p. 193-204.
 105. Larsson, A., G. D'Acunto, M. Vorobyova, G. Abbondanza, U. Lienert, Z. Hegedüs, A. Preobrajenski, L.R. Merte, J. Eidhagen, A. Delblanc, et al., *Thickness and composition of native oxides and near-surface regions of Ni superalloys*. Journal of Alloys and Compounds, 2022. **895**: p. 162657.
 106. Alexander, M.R., G.E. Thompson, X. Zhou, G. Beamson, and N. Fairley, *Quantification of oxide film thickness at the surface of aluminium using XPS*. 2002. **34**(1): p. 485-489.
 107. Gardin, E., S. Zanna, A. Seyeux, A. Allion-Maurer, and P. Marcus, *Comparative study of the surface oxide films on lean duplex and corresponding single phase stainless steels by XPS and ToF-SIMS*. Corrosion Science, 2018. **143**: p. 403-413.
 108. Larsson, A., K. Simonov, J. Eidhagen, A. Grespi, X. Yue, H. Tang, A. Delblanc, M. Scardamaglia, A. Shavorskiy, J. Pan, et al., *In situ quantitative analysis of electrochemical oxide film development on metal surfaces using ambient pressure X-ray photoelectron spectroscopy: Industrial alloys*. Applied Surface Science, 2023. **611**: p. 155714.
 109. Siegbahn, H. and K. Siegbahn, *ESCA applied to liquids*. Journal of Electron Spectroscopy and Related Phenomena, 1973. **2**(3): p. 319-325.

110. Blomberg, S., U. Hejral, M. Shipilin, S. Albertin, H. Karlsson, C. Hulteberg, P. Lömker, C. Goodwin, D. Degerman, J. Gustafson, et al., *Bridging the Pressure Gap in CO Oxidation*. ACS Catalysis, 2021. **11**(15): p. 9128-9135.
111. Amann, P., D. Degerman, M.-T. Lee, J.D. Alexander, M. Shipilin, H.-Y. Wang, F. Cavalca, M. Weston, J. Gladh, M. Blom, et al., *A high-pressure x-ray photoelectron spectroscopy instrument for studies of industrially relevant catalytic reactions at pressures of several bars*. Review of Scientific Instruments, 2019. **90**(10).
112. Degerman, D., P. Amann, C.M. Goodwin, P. Lömker, H.-Y. Wang, M. Soldemo, M. Shipilin, C. Schlueter, and A. Nilsson, *Operando X-ray Photoelectron Spectroscopy for High-Pressure Catalysis Research Using the POLARIS Endstation*. Synchrotron Radiation News, 2022. **35**(3): p. 11-18.
113. Schnadt, J., J. Knudsen, and N. Johansson, *Present and new frontiers in materials research by ambient pressure x-ray photoelectron spectroscopy*. Journal of Physics: Condensed Matter, 2020. **32**(41): p. 413003.
114. Ogletree, D.F., H. Bluhm, G. Lebedev, C.S. Fadley, Z. Hussain, and M. Salmeron, *A differentially pumped electrostatic lens system for photoemission studies in the millibar range*. Review of Scientific Instruments, 2002. **73**(11): p. 3872-3877.
115. Starr, D.E., Z. Liu, M. Hävecker, A. Knop-Gericke, and H. Bluhm, *Investigation of solid/vapor interfaces using ambient pressure X-ray photoelectron spectroscopy*. Chemical Society Reviews, 2013. **42**(13): p. 5833-5857.
116. Salmeron, M. and R. Schlögl, *Ambient pressure photoelectron spectroscopy: A new tool for surface science and nanotechnology*. Surface Science Reports, 2008. **63**(4): p. 169-199.
117. Karslıoğlu, O., S. Nemšák, I. Zegkinoglou, A. Shavorskiy, M. Hartl, F. Salmassi, E.M. Gullikson, M.L. Ng, C. Rameshan, B. Rude, et al., *Aqueous solution/metal interfaces investigated in operando by photoelectron spectroscopy*. Faraday Discussions, 2015. **180**(0): p. 35-53.
118. Axnanda, S., E.J. Crumlin, B. Mao, S. Rani, R. Chang, P.G. Karlsson, M.O.M. Edwards, M. Lundqvist, R. Moberg, P. Ross, et al., *Using "Tender" X-ray Ambient Pressure X-Ray Photoelectron Spectroscopy as A Direct Probe of Solid-Liquid Interface*. Scientific Reports, 2015. **5**(1): p. 9788.
119. Favaro, M., B. Jeong, P.N. Ross, J. Yano, Z. Hussain, Z. Liu, and E.J. Crumlin, *Unravelling the electrochemical double layer by direct probing of the solid/liquid interface*. Nature Communications, 2016. **7**(1): p. 12695.
120. Favaro, M., J. Yang, S. Nappini, E. Magnano, F.M. Toma, E.J. Crumlin, J. Yano, and I.D. Sharp, *Understanding the Oxygen Evolution Reaction Mechanism on CoOx using Operando Ambient-Pressure X-ray Photoelectron Spectroscopy*. Journal of the American Chemical Society, 2017. **139**(26): p. 8960-8970.
121. Lichterman, M.F., S. Hu, M.H. Richter, E.J. Crumlin, S. Axnanda, M. Favaro, W. Drisdell, Z. Hussain, T. Mayer, B.S. Brunschwig, et al., *Direct observation of the energetics at a semiconductor/liquid junction by operando X-ray photoelectron spectroscopy*. Energy & Environmental Science, 2015. **8**(8): p. 2409-2416.
122. Lichterman, M.F., M.H. Richter, B.S. Brunschwig, N.S. Lewis, and H.-J. Lewerenz, *Operando X-ray photoelectron spectroscopic investigations of the electrochemical*

- double layer at Ir/KOH(aq) interfaces*. Journal of Electron Spectroscopy and Related Phenomena, 2017. **221**: p. 99-105.
123. Han, Y., S. Axnanda, E.J. Crumlin, R. Chang, B. Mao, Z. Hussain, P.N. Ross, Y. Li, and Z. Liu, *Observing the Electrochemical Oxidation of Co Metal at the Solid/Liquid Interface Using Ambient Pressure X-ray Photoelectron Spectroscopy*. The Journal of Physical Chemistry B, 2018. **122**(2): p. 666-671.
 124. Maibach, J., I. Källquist, M. Andersson, S. Urpelainen, K. Edström, H. Rensmo, H. Siegbahn, and M. Hahlin, *Probing a battery electrolyte drop with ambient pressure photoelectron spectroscopy*. Nature Communications, 2019. **10**(1): p. 3080.
 125. Ali-Löytty, H., M.W. Louie, M.R. Singh, L. Li, H.G. Sanchez Casalongue, H. Ogasawara, E.J. Crumlin, Z. Liu, A.T. Bell, A. Nilsson, et al., *Ambient-Pressure XPS Study of a Ni-Fe Electrocatalyst for the Oxygen Evolution Reaction*. The Journal of Physical Chemistry C, 2016. **120**(4): p. 2247-2253.
 126. Yue, X., A. Larsson, H. Tang, A. Grespi, M. Scardamaglia, A. Shavorskiy, A. Krishnan, E. Lundgren, and J. Pan, *Synchrotron-based near ambient-pressure X-ray photoelectron spectroscopy and electrochemical studies of passivation behavior of N- and V-containing martensitic stainless steel*. Corrosion Science, 2023. **214**: p. 111018.
 127. Novotny, Z., D. Aegerter, N. Comini, B. Tobler, L. Artiglia, U. Maier, T. Moehl, E. Fabbri, T. Huthwelker, T.J. Schmidt, et al., *Probing the solid-liquid interface with tender x rays: A new ambient-pressure x-ray photoelectron spectroscopy endstation at the Swiss Light Source*. Review of Scientific Instruments, 2020. **91**(2).
 128. Liu, C., Q. Dong, Y. Han, Y. Zang, H. Zhang, X. Xie, Y. Yu, and Z. Liu, *Understanding fundamentals of electrochemical reactions with tender X-rays: A new lab-based operando X-ray photoelectron spectroscopy method for probing liquid/solid and gas/solid interfaces across a variety of electrochemical systems*. Chinese Journal of Catalysis, 2022. **43**(11): p. 2858-2870.
 129. Griesser, C., D. Winkler, T. Moser, L. Haug, M. Thaler, E. Portenkirchner, B. Klötzer, S. Diaz-Coello, E. Pastor, and J. KunzeLiebhäuser, *Lab-based electrochemical X-ray photoelectron spectroscopy for in-situ probing of redox processes at the electrified solid/liquid interface*. n/a(n/a): p. e2300007.
 130. Booth, S.G., A.M. Tripathi, I. Strashnov, R.A.W. Dryfe, and A.S. Walton, *The offset droplet: a new methodology for studying the solid/water interface using x-ray photoelectron spectroscopy*. Journal of Physics: Condensed Matter, 2017. **29**(45): p. 454001.
 131. Knop-Gericke, A., V. Pfeifer, J.-J. Velasco-Velez, T. Jones, R. Arrigo, M. Hävecker, and R. Schlögl, *In situ X-ray photoelectron spectroscopy of electrochemically active solid-gas and solid-liquid interfaces*. Journal of Electron Spectroscopy and Related Phenomena, 2017. **221**: p. 10-17.
 132. Velasco-Vélez, J.-J., L.J. Falling, D. Bernsmeier, M.J. Sear, P.C.J. Clark, T.-S. Chan, E. Stotz, M. Hävecker, R. Kraehnert, A. Knop-Gericke, et al., *A comparative study of electrochemical cells for in situ x-ray spectroscopies in the soft and tender x-ray range*. Journal of Physics D: Applied Physics, 2021. **54**(12): p. 124003.

133. Als-Nielsen, J.M., *Des Kinematical scattering II: crystalline order*, in *Elements of Modern X-ray Physics*. 2011. p. 147-205.
134. Welzel, U., J. Ligot, P. Lamparter, A.C. Vermeulen, and E.J. Mittemeijer, *Stress analysis of polycrystalline thin films and surface regions by X-ray diffraction*. *Journal of Applied Crystallography*, 2005. **38**: p. 1-29.
135. Chason, E., T.J.C.R.i.S.S. Mayer, and M. Sciences, *Thin film and surface characterization by specular X-ray reflectivity*. 1997. **22**(1): p. 1-67.
136. Björck, M. and G.J.J.o.A.C. Andersson, *GenX: an extensible X-ray reflectivity refinement program utilizing differential evolution*. 2007. **40**(6): p. 1174-1178.
137. Glavic, A. and M.J.J.o.a.c. Björck, *GenX 3: the latest generation of an established tool*. 2022. **55**(4).
138. Bras, W., D.A.A. Myles, and R. Felici, *When x-rays alter the course of your experiments**. *Journal of Physics: Condensed Matter*, 2021. **33**(42): p. 423002.
139. Thompson, A.C. and D. Vaughan, *X-ray data booklet*. Vol. 8. 2001: Lawrence Berkeley National Laboratory, University of California Berkeley, CA.
140. Inokuti, M., *Inelastic Collisions of Fast Charged Particles with Atoms and Molecules---The Bethe Theory Revisited*. *Reviews of Modern Physics*, 1971. **43**(3): p. 297-347.
141. Glaeser, R., M. Facciotti, P. Walian, S. Rouhani, J. Holton, A. MacDowell, R. Celestre, D. Cambie, and H. Padmore, *Characterization of Conditions Required for X-Ray Diffraction Experiments with Protein Microcrystals*. *Biophysical Journal*, 2000. **78**(6): p. 3178-3185.
142. Christensen, C.K., M.A. Karlsen, A.Ø. Drejer, B.P. Andersen, C.L. Jakobsen, M. Johansen, D.R. Sørensen, I. Kantor, M.R.V. Jørgensen, and D.B.J.J.o.S.R. Ravnsbæk, *Beam damage in operando X-ray diffraction studies of Li-ion batteries*. 2023. **30**(3).
143. Loh, Z.H., G. Doumy, C. Arnold, L. Kjellsson, S.H. Southworth, A. Al Haddad, Y. Kumagai, M.F. Tu, P.J. Ho, A.M. March, et al., *Observation of the fastest chemical processes in the radiolysis of water*. *Science*, 2020. **367**(6474): p. 179-182.
144. Schwarz, H.A., *Free radicals generated by radiolysis of aqueous solutions*. 1981, ACS Publications.
145. Farooq, Z., D.A. Chestakov, B. Yan, G.C. Groenenboom, W.J. van der Zande, and D.H. Parker, *Photodissociation of singlet oxygen in the UV region*. *Physical Chemistry Chemical Physics*, 2014. **16**(7): p. 3305-3316.
146. Li, X., H. Zhang, Y. Ran, M. Ye, F. Yang, Y. Han, and Z. Liu, *Beam-Induced Effects on Platinum Oxidation during Ambient-Pressure X-ray Photoelectron Spectroscopy*. *The Journal of Physical Chemistry Letters*, 2022. **13**(24): p. 5677-5682.
147. Gervais, C., M. Thoury, S. Réguer, P. Gueriau, and J. Mass, *Radiation damages during synchrotron X-ray micro-analyses of Prussian blue and zinc white historic paintings: detection, mitigation and integration*. *Applied Physics A*, 2015. **121**(3): p. 949-955.
148. Zabilska, A., A.H. Clark, D. Ferri, M. Nachtegaal, O. Kröcher, and O.V. Safonova, *Beware of beam damage under reaction conditions: X-ray induced photochemical*

- reduction of supported VOx catalysts during in situ XAS experiments.* Physical Chemistry Chemical Physics, 2022. **24**(36): p. 21916-21926.
149. Polvino, S.M., C.E. Murray, Ö. Kalenci, I.C. Noyan, B. Lai, and Z. Cai, *Synchrotron microbeam x-ray radiation damage in semiconductor layers.* Applied Physics Letters, 2008. **92**(22): p. 224105.
 150. Akazawa, H., *FORMATION OF SILICON NANOCRYSTALS AND INTERFACE ISLANDS IN SYNCHROTRON-RADIATION-IRRADIATED SiO₂ FILMS ON Si(100).* International Journal of Modern Physics B, 2001. **15**(28n30): p. 3749-3752.
 151. Weber, T., V. Vonk, M.J.S. Abb, J. Evertsson, A. Stierle, E. Lundgren, and H. Over, *In Situ Synchrotron-Based Studies of IrO₂(110)–TiO₂(110) under Harsh Acidic Water Splitting Conditions: Anodic Stability and Radiation Damages.* The Journal of Physical Chemistry C, 2022. **126**(48): p. 20243-20250.
 152. Massover, W.H.J.J.o.S.R., *Radiation damage to protein specimens from electron beam imaging and diffraction: a mini-review of anti-damage approaches, with special reference to synchrotron X-ray crystallography.* 2007. **14**(1): p. 116-127.
 153. de La Mora, E., N. Coquelle, C.S. Bury, M. Rosenthal, J.M. Holton, I. Carmichael, E.F. Garman, M. Burghammer, J.-P. Colletier, and M.J.P.o.t.N.A.o.S. Weik, *Radiation damage and dose limits in serial synchrotron crystallography at cryo-and room temperatures.* 2020. **117**(8): p. 4142-4151.
 154. Jousseume, T., J.-F. Colin, M. Chandesris, S. Lyonard, and S. Tardif, *How Beam Damage Can Skew Synchrotron Operando Studies of Batteries.* ACS Energy Letters, 2023: p. 3323-3329.
 155. Onderwaater, W.G., A. Taranovskyy, G.M. Bremmer, G.C. van Baarle, J.W.M. Frenken, and I.M.N. Groot, *From dull to shiny: A novel setup for reflectance difference analysis under catalytic conditions.* Review of Scientific Instruments, 2017. **88**(2): p. 023704.
 156. Onderwaater, W.G., A. Taranovskyy, G.C. van Baarle, J.W.M. Frenken, and I.M.N. Groot, *In Situ Optical Reflectance Difference Observations of CO Oxidation over Pd(100).* The Journal of Physical Chemistry C, 2017. **121**(21): p. 11407-11415.
 157. Zhou, J., S. Blomberg, J. Gustafson, E. Lundgren, and J. Zetterberg, *Simultaneous Imaging of Gas Phase over and Surface Reflectance of a Pd(100) Single Crystal during CO Oxidation.* The Journal of Physical Chemistry C, 2017. **121**(42): p. 23511-23519.
 158. Pfaff, S., J. Zhou, U. Hejral, J. Gustafson, M. Shipilin, S. Albertin, S. Blomberg, O. Gutowski, A. Dippel, E. Lundgren, et al., *Combining high-energy X-ray diffraction with Surface Optical Reflectance and Planar Laser Induced Fluorescence for operando catalyst surface characterization.* Review of Scientific Instruments, 2019. **90**(3): p. 033703.
 159. Albertin, S., J. Gustafson, J. Zhou, S. Pfaff, M. Shipilin, S. Blomberg, L.R. Merte, O. Gutowski, A.C. Dippel, J. Zetterberg, et al., *Surface optical reflectance combined with x-ray techniques during gas-surface interactions.* Journal of Physics D: Applied Physics, 2020. **53**(22): p. 224001.

160. Rämisch, L., S.M. Gericke, S. Pfaff, E. Lundgren, and J. Zetterberg, *Infrared surface spectroscopy and surface optical reflectance for operando catalyst surface characterization*. Applied Surface Science, 2022. **578**: p. 152048.
161. Pfaff, S., L. Rämisch, S.M. Gericke, A. Larsson, E. Lundgren, and J. Zetterberg, *Visualizing the Gas Diffusion Induced Ignition of a Catalytic Reaction*. ACS Catalysis, 2022. **12**(11): p. 6589-6595.
162. Shkirskiy, V. and F. Kanoufi, *Reflective microscopy for mechanistic insights in corrosion research*. Current Opinion in Electrochemistry, 2023. **39**: p. 101259.
163. Li, R., A. Makogon, T. Galochkina, J.-F. Lemineur, F. Kanoufi, and V. Shkirskiy, *Unsupervised Analysis of Optical Imaging Data for the Discovery of Reactivity Patterns in Metal Alloy*. Small Methods, 2023. **n/a**(n/a): p. 2300214.
164. Godeffroy, L., A. Makogon, S. Gam Derouich, F. Kanoufi, and V. Shkirskiy, *Imaging and Quantifying the Chemical Communication between Single Particles in Metal Alloys*. Analytical Chemistry, 2023. **95**(26): p. 9999-10007.
165. Homborg, A.M., M. Olgıati, P.J. Denissen, and S.J. Garcia, *An integral non-intrusive electrochemical and in-situ optical technique for the study of the effectiveness of corrosion inhibition*. Electrochimica Acta, 2022. **403**: p. 139619.
166. Larsson, A., M. Vorobyova, S. Pfaff, G. Abbondanza, J. Pan, J. Zetterberg, and E. Lundgren, *Operando Surface Optical Reflectance Microscopy Study of Corrosion Film Growth on a Ni–Cr–Mo Alloy During Anodic Polarization*. The Journal of Physical Chemistry C, 2023.
167. Diebold, U., S.-C. Li, and M. Schmid, *Oxide Surface Science*. Annual Review of Physical Chemistry, 2010. **61**(1): p. 129-148.
168. Woodruff, D.P., *Modern techniques of surface science*. 2016: Cambridge university press.
169. Kolb, D.M., *An atomistic view of electrochemistry*. Surface Science, 2002. **500**(1): p. 722-740.
170. Kortlever, R., J. Shen, K.J.P. Schouten, F. Calle-Vallejo, and M.T.M. Koper, *Catalysts and Reaction Pathways for the Electrochemical Reduction of Carbon Dioxide*. The Journal of Physical Chemistry Letters, 2015. **6**(20): p. 4073-4082.
171. Birdja, Y.Y., E. Pérez-Gallent, M.C. Figueiredo, A.J. Göttle, F. Calle-Vallejo, and M.T.M. Koper, *Advances and challenges in understanding the electrocatalytic conversion of carbon dioxide to fuels*. Nature Energy, 2019. **4**(9): p. 732-745.
172. Dincer, I., *Green methods for hydrogen production*. International Journal of Hydrogen Energy, 2012. **37**(2): p. 1954-1971.
173. Wang, Y., D.F. Ruiz Diaz, K.S. Chen, Z. Wang, and X.C. Adroher, *Materials, technological status, and fundamentals of PEM fuel cells – A review*. Materials Today, 2020. **32**: p. 178-203.
174. Hwang, J.-Y., S.-T. Myung, and Y.-K. Sun, *Sodium-ion batteries: present and future*. Chemical Society Reviews, 2017. **46**(12): p. 3529-3614.
175. Xie, J. and Y.-C. Lu, *A retrospective on lithium-ion batteries*. Nature Communications, 2020. **11**(1): p. 2499.